

DEUTSCHES ELEKTRONEN-SYNCHROTRON
in der HELMHOLTZ-GEMEINSCHAFT



DESY-THESIS-2006-014

July 2006

**Search for the Pentaquark States
in Lepton-Nucleon Scattering
at HERMES**

by

L. Rubáček

ISSN 1435-8085

NOTKESTRASSE 85 - 22607 HAMBURG

Search for the Pentaquark States in Lepton-Nucleon Scattering at HERMES

Inaugural - Dissertation
zur Erlangung des Doktorgrades der Naturwissenschaften
der Justus Liebig Universität Giessen
Fachbereich 07 (Mathematik und Informatik, Physik, Geographie)

vorgelegt von

Lukáš Rubáček

aus Náchod

II. Physikalisches Institut
der Justus Liebig Universität Giessen
Februar 2006

Dekan: Prof. Dr. V. Metag

I. Berichterstatter: Prof. Dr. M. Düren

II. Berichterstatter: Prof. Dr. A. Müller

Contents

Zusammenfassung	1
1 Introduction	4
2 Search for Pentaquark	6
2.1 Why Search for the Pentaquark?	6
2.2 Quark Models	7
2.2.1 Pentaquark Models	10
2.2.2 Diakonov, Petrov & Polyakov Predictions	11
2.3 Experimental Results	13
2.3.1 Evidence for the Θ^+	13
2.3.2 Non-Evidence for the Θ^+	16
2.3.3 The Search for Other Candidates	18
2.4 Current Status	19
3 The HERMES Experiment	20
3.1 The HERA Accelerator	20
3.2 The HERMES Target	21
3.3 Tracking Detectors	23
3.4 Particle Identification	25
3.5 Beam Monitoring	29
3.6 Trigger and Data Acquisition	29
4 Analysis of HERMES Data	32
4.1 HERMES Data Selection	33
4.2 The Θ^- State	40
4.3 Four Track Events Analysis	42
4.4 Monte Carlo	45
4.5 Width and Angular Distribution of the Θ^+	46
4.6 Karliner - Lipkin Scheme	49
4.6.1 $\Lambda(1520)$ and $\bar{\Lambda}(1520)$	49
4.6.2 Application of K.-L. Scheme	52
4.7 Kinematic Reflection	55
4.7.1 N1710	57

4.7.2	$\Xi^0(1690)$	61
4.8	Summary of the Pentaquark Analysis	64
5	The Recoil Project	66
5.1	Generalized Parton Distributions	66
5.2	The Detector	68
5.3	SFT Frontend Electronics	73
5.3.1	Signal Handling in the PFM	76
5.3.2	Testing and Setup of the PFMs for Readout of PMT Signals	78
5.4	GSI Test Beam	83
5.4.1	Experimental Setup	84
5.4.2	Digitization and DAQ	85
5.4.3	Results of the Testbeam	87
6	Conclusion	92
	List of Figures	94
	List of Tables	98
	Bibliography	99
	Acknowledgments	106

Zusammenfassung

Alle bekannte Hadronen können als System von zwei oder drei Quarks beschrieben werden. Modelle der Hadronenphysik erlauben zwar Zustände, deren Quantenzahlen man nur mit mehr als drei Quarks erklären kann. Solche Teilchen wurden aber in der Vergangenheit nicht entdeckt. Diakonov, Petrov und Polyakov, die ein Quark-Soliton Modell benutzten, sagten Pentaquark als schmale Resonanz mit einer Masse von 1530MeV , einer Breite 15MeV und dem Zerfallskanal pK_S voraus. Der vorausgesagte Zustand wurde erstmals im Jahr 2002 durch das LEPs Experiment beobachtet. Mehrere Experimente haben diese Beobachtung bestätigt inklusive des HERMES Experiments. Die Suche nach dem vorausgesagten Teilchen in den HERMES Daten stellen einen Schwerpunkt dieser Arbeit dar.

Da eine gute Teilchenidentifikation für die Analyse erforderlich ist, wurden nur Daten, die in den Jahren 1998, 1999 und 2000 mit dem HERMES Ring Image Cherenkov gemessen wurden, ausgewählt. Aus dem Datensatz werden die Ereignisse ausgewählt, die mindestens drei Hadronenspuren enthalten, davon zwei gegensätzlich geladene Pionen und ein Proton. Die Auswahlkriterien der Pionen werden so optimiert, dass der Untergrund im K_S^0 Massenspektrum möglichst gering ist. Allerdings dürfen diese Kriterien keine künstliche Struktur im $p\pi^+\pi^-$ Massenspektrum erzeugen. Deswegen werden Ereignisse, die möglicherweise aus einem $\Lambda(1116)$ -Zerfall stammen, verworfen. Im resultierendem Spektrum wird ein Peak der Masse $1528 \pm 2.6(stat) \pm 2.1(syst) \text{MeV}$ und eine Breite $\Gamma = 19 \text{MeV}$ beobachtet. Die Signifikanz des beobachteten Peak entspricht ungefähr 4σ , abhängig davon, welche Funktion zur Beschreibung des Untergrund benutzt wird.

Es wurden drei verschiedene Verfahren benutzt, um den Untergrund besser zu verstehen. Erstens wurde ein Polynom drittes Grades angepasst, zweitens, es wurden die Impulse des K_S^0 und des Protons aus verschiedenen Ereignisse gemischt. Als letzte Meth-

ode wurden PYTHIA6 Simulationen durchgeführt und mit gemessenen Daten verglichen. Die Ergebnisse aus den PYTHIA6 Simulationen und der gemischten Ereignisse stimmen überein. Damit der Fit des Untergrunds gut angepasst werden kann, wurden in PYTHIA6 die fehlenden Σ Resonanzen addiert.

Weiterhin wird in der Analyse die Kinematik der Zerfallsprodukte untersucht um etwas über den Produktionsmechanismus zu lernen. werden. Die bisher vorhandene niedrige Statistik lässt allerdings keine eindeutige Schlussfolgerung aus den Ergebnissen zu.

Da mehrere Experimente, die ebenfalls nach Θ^+ Zuständen gesucht haben, diese trotz guter Statistik nicht beobachteten, stellt sich die Frage, ob der Θ^+ Zustand wirklich existiert. Der Standpunkt, dass das Θ^+ nicht existiert, wird durch die geringe Statistik der Experimente, die es beobachten, unterstützt. Als Quelle des Peaks wurden kinematische Reflektionen diskutiert. Zustände, die in $K_S\Lambda$ zerfallen, können durch die beschränkte Akzeptanz bei HERMES als pK_S nachgewiesen worden sein. In dieser Arbeit wird die Möglichkeit einen Peak durch nicht vollständig nachgewiesene Endzustände zu erzeugen simuliert. Es wurde gezeigt, dass der Zerfall bekannter Zustände keinen in Masse, Breite und Intensität gleichen Peak produzieren kann.

Der zweite Schwerpunkt dieser Arbeit liegt im Beitrag zum Bau des Recoil Detector, der rückgestreute Protonen in HERMES nachweisen soll. Diese sind besonders wichtig bei der Untersuchung der Tief-Virtuellen Compton-Streuung (DVCS), wobei im Endzustand ein Proton von Δ -Resonanzen unterschieden werden soll. Der gesamte Recoil Detector ist aus drei verschiedenen Detektoren aufgebaut, wobei in Giessen ein Detektor aus szintillierenden Fasern gebaut wurde.

Die Arbeit befasst sich mit dem Aufbau der Ausleseelektronik für den Detektor aus szintillierenden Fasern. Um Lichtsignale nachzuweisen, werden 64-Kanal Multi-Anoden Hamamatsu Photomultiplier benutzt. Die Ausleseelektronik wurde aus dem RICH Detektor des HADES Experiments übernommen. Jeder Photomultiplier wird mit Frontend-Modulen (FM) mit 64 Verstärkerkanälen und einer A/D-Wandlungseinheit mit Speicher für 120 Ereignisse verbunden. Als ladungsempfindlich Verstärker wird der GASSIPLEX-Chip benutzt. Die Auslese des FM sowie eine weitere Datenspeicherung erfolgt über einem Readout-Controller (RC) mit VME-Busanschluss.

Damit eine Auslese des Photomultipliers mit der HADES-Elektronik möglich ist, wurde der Einbau eines kapazitiven Kopplungskreises für des Analogsignal notwendig. Außerdem wurde die Schaltung des Multiplexers auf dem FM umgebaut. Die Elektronik wurde

in verschiedenen Anordnungen untersucht. Die Tests umfassen dabei von einem Pulser generierte elektrische Signale am GASSIPLEX-Analogeingang bishin zu Testexperimenten mit einem gemischten Proton- und Pionstrahl. Die letztgenannte Test wurde an der GSI in Darmstadt durchgeführt. Die erzielte Ergebnisse zeigen dabei gute Teilchenidentifikationsfähigkeiten des Faserndetektors, die auch für die weitere Untersuchung des Pentaquarks bei HERMES wichtig sind.

Nach einer kurzen Einleitung, wird im zweiten Kapitel eine Übersicht über theoretische Modelle die das Pentaquark beschreiben, gegeben und die experimentellen Ergebnisse über das Pentaquark zusammengefasst. Das dritte Kapitel beschreibt den Aufbau des HERMES Spektrometer am DESY in Hamburg. Das vierte Kapitel befasst sich mit der Analyse des Pentaquark aus den HERMES-Daten. Im fünften Kapitel werden Aufbau und Test des Ausleseelektronik für das Recoil Detector Projekt beschrieben. Im sechsten Kapitel wird eine Zusammenfassung gegeben.

Chapter 1

Introduction

One of the unexplained phenomena in Hadronic Physics is an existence of states which can be interpreted only as a combination of more than three valence quarks. Such states have been discussed since the earliest quark models but have never been observed experimentally. The developments in the past few years in the field of Hadronic Models postulate a new prediction of a possible exotic strange pentaquark with a narrow width which was afterwards confirmed by observations in several experiments. Since none of these experiments were optimized for such a search, the results exhibit a low significance of the observed particle. Later on, the situation was muddied further when several experiments reported non-evidence of a such pentaquark state.

Since there exist several different theoretical models supporting both, existence and non-existence of the strange exotic pentaquark, there is the challenge for experimental physics to prove which of those models are correct. Although the HERMES experiment was designed for the measurement of the proton spin structure, the data recorded during several years of running was used in order to contribute to the effort of searching for the strange exotic pentaquark.

This thesis describes the search for the exotic pentaquark Θ^+ at the HERMES experiment. The first section is a short introduction to the theoretical predictions of the pentaquark and the current status of experimental results. The second section describes the HERMES experiment at DESY. The third section describes the analysis of the data obtained by HERMES. The study of the pK_S system published by the HERMES collaboration in [18] has been reanalyzed. Further analyses and Monte Carlo studies are focused on topics related to the measurement of the angular distribution of the decaying products of the

pentaquark candidates. Kinematic studies of the $\Lambda(1520)$, which is related to the Θ^+ due to its similar mass and similar decay channel, are performed. The fourth topic is that of simulations which are focused to study potential fake sources of the pentaquark peak - known as “kinematical reflections”.

The last section presents the author’s contribution to the Recoil Detector project at HERMES. The Recoil Project is aimed to extend the HERMES acceptance to measure slow particles under wide angles. The study of the proton structure by means of Deeply Virtual Compton Scattering is the main task for the Recoil Detector. The author’s work has been focused on the building of the read-out electronics for the Scintillating Fiber Tracker. The final design of the analog electronics is presented and the results of a test experiment at GSI. Apart from the study of the internal structure of proton, the Recoil Detector can also play a significant role in the search for the exotic Θ^+ pentaquark.

Chapter 2

Search for Pentaquark

2.1 Why Search for the Pentaquark?

The nature of material substances in the universe has fascinated people since time immemorial. One of the most popular ideas of the ancient world was that of the Universe as composed of four infinitely dividable elements - Earth, Fire, Water and Air. In the fifth century BC, Demokritos opposed it and suggested that everything was built from elements which can not be divided any further. He named them “a-thomos”, which means “indivisible”.

First candidates for Demokritos' atoms were found more than two thousand years after his death, when Dalton assigned to each chemical element one kind of atom. Mendeleyev classified elements according their properties into the Periodic Table. The fact that this table has an internal structure was a first hint that Dalton's atoms are not “a-thomos” in the sense of Demokritos' idea. At the turn of the 20th century, subcomponents of the atoms were found. In 1897, Thomson [1] discovered electrons in cathode-rays and in 1911 Rutherford [2] found that the majority of the atomic mass is concentrated in a positively charged nucleus which is five orders of magnitude smaller than the entire atom.

Later in the century, even nuclei were split into their own subcomponents - protons and neutrons. These two types of particle, in addition to the electron, were viewed as the fundamental particles. Electron scattering experiments discovered a non point-like behavior of protons and neutrons. With the development of particle physics in the 1950s, hundreds of new particles were discovered. This was the genesis of hadron spectroscopy, which developed methods to observe the smallest constituents of matter, the quarks. All known hadrons can

be considered as a combination of two or three quarks, but there is no theory which excludes the existence of particles composed by four, five or even more quarks.

The earliest quark models discussed the possibility of such tetra- or penta-quark states, however no such state has been observed experimentally. In their 1995 work [25], Diakonov, Petrov and Polyakov predicted a narrow exotic pentaquark state. These predictions galvanized experimental efforts and the first observation of this predicted pentaquark was reported by LEPs collaboration [31]. Several experiments confirmed this result, among them the HERMES experiment at DESY. However, the initial enthusiasm over the existence of the pentaquark has since been dampened by several experiments which found no evidence of such a resonance. Current opinion is divided over the existence of the pentaquark - one fraction supporting the existence of the resonance, the other denying it.

2.2 Quark Models

Initial models of the hadronic spectra described the hadrons using the following quantum numbers: Charge Q , Baryon Number B , Z -Component of the Isospin T , and Hypercharge Y . Gell-Mann [3, 4] and Ne'emann [5] classified mesons and baryons in a scheme which they called "The Eightfold Way". Mesons are described by singlet and octet presentations of an $SU(3)$ Lie group and baryons by singlet, octet and decuplet presentations of such a group. In this scheme baryons and mesons can be considered as a composition of constituents called quarks and anti-quarks. The mesons are built from $q\bar{q}$ pairs whereas baryons are combinations of three quarks qqq . In the earliest quark models all hadrons were built from combinations of only three types of quark known as 'flavours': Up ' u ', Down ' d ' and Strange ' s '. The multiplets of the mesons and baryons consisting of these three lightest quarks are shown in Fig. 2.1. Through the discovery of new particles like the J/Ψ and Υ , the quark 'family' was given two new flavours Charm ' c ' and Beauty ' b '. The most recently observed quark has flavor Top ' t '. Current knowledge of quarks and their quantum numbers are summarized in Table 2.1. These quantum numbers are conserved in strong and electromagnetic processes. Weak interaction may change the flavor of the quarks.

The quark-idea as obtained from the hadron spectroscopy became of more importance after the discoveries in the scattering experiments of high energy electrons on protons in the 1970s [6]. These measurements showed results that were similar to those of Rutherford's experiment with nuclei. The measured energy and angular distributions

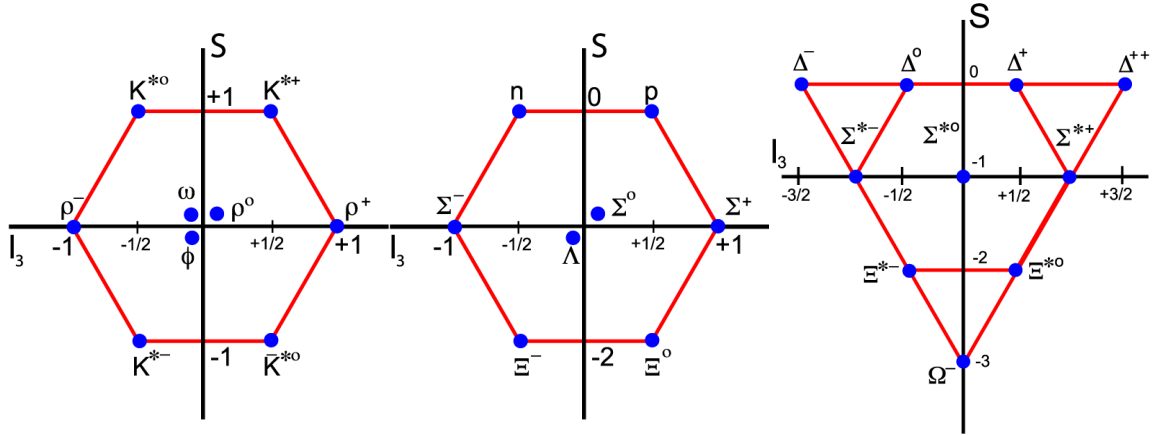


Figure 2.1: The multiplets of the hadrons in the plane given by strangeness and z -components of the isospin. The left diagram shows the SU(3) octet of the mesons with and a Φ which belongs to the SU(3) singlet. The plot in middle shows the SU(3) baryon octet and the rightmost the baryon decuplet.

Quark	d	u	s	c	b	t
Q - electric charge	-1/3	2/3	-1/3	2/3	-1/3	2/3
t_z - isospin	-1/2	1/2	0	0	0	0
s - strangeness	0	0	-1	0	0	0
c - charm	0	0	0	1	0	0
b - beauty	0	0	0	0	1	0
t - topness	0	0	0	0	0	1

Table 2.1: Additive quantum numbers of the quarks.

violated the expectation for scattering on a diffusely distributed charge inside the proton. The “scaling” properties of the measured distributions suggested that there are localized scattering centers within a proton that are point like objects without any substructure. This charged-scattering centers were named “partons”. The partons behave like a spin- $\frac{1}{2}$ object with $2/3$ or $1/3$ of the elementary charge. They could be identified with the quarks that were found in hadron spectroscopy.

With the increased precision of Deep Inelastic Scattering (DIS), a violation of the observed scaling behavior was noticed. Theoretical fixes accounting for the scaling violations involving interactions between the quarks predicted the existence of a new type of parton. This electrically neutral, spin-1 parton (named a “gluon”) plays the role of the gauge boson in the field theory of the strong interactions. However, the scaling violation was only an indirect hint about existence of gluons. The gluon was more directly observed in 1979 in e^+e^- colliding experiments at the PETRA accelerator at DESY [7]. The observed coplanar, three-hadronic jet events were explained as being generated by quark-antiquark pairs accompanied by a hard non-collinear gluon.

Baryons are fermions, thus their total wave function has to be antisymmetric. This fact caused problems in the quark model for states like Ω^- , Δ^{++} and Δ^- , where quantum numbers lead to the following quark content:

$$|\Omega^-\rangle = |\uparrow s\rangle|\uparrow s\rangle|\uparrow s\rangle, \quad (2.1)$$

$$|\Delta^{++}\rangle = |\uparrow u\rangle|\uparrow u\rangle|\uparrow u\rangle, \quad (2.2)$$

$$|\Delta^-\rangle = |\uparrow d\rangle|\uparrow d\rangle|\uparrow d\rangle. \quad (2.3)$$

In order to obey Fermi statistics, the quarks must differ at least in one quantum number. The problem was solved by the introduction of a new quantum number named “color”. Color is the charge of the strong interaction and has three degrees of freedom. Each valence quark inside the baryon has a different color, whilst the entire baryon behaves like a color neutral object. The colors of quarks are conventionally denoted as red, green and blue. The anti-quarks are considered to carry the corresponding anti-colors.

The models which explain baryons in terms of three quarks are today considered as a simplified view of the internal hadron structure. They are successful in describing collective properties of hadrons like mass or magnetic moment. However, these models are no longer sufficient to explain results of experiments which are investigating the internal structure of hadrons with higher energy probes. In the 1960's, the gauge theory of strong

interaction evolved and today is known as Quantum Chromodynamics (QCD). The most important step in developing this theory was done by D.J. Gross, H.D. Politzer and F. Wilczek [8, 9] who studied non-Abelian gauge theories and found that such theories are renormalizable and have an asymptotic free behavior. The asymptotic freedom results from the fact that gluons, which mediate the force between quarks, are carrying color and can interact with each other. The consequence of this feature of strong interaction is that the quarks in high-energy collisions behave like "free" particles, while at low energies they are strongly bound and confined in hadrons or mesons.

QCD allows the existence of any combination of quarks for which the total color is "white". The simplest way this might be achieved is by the combination of three quarks qqq in the case of baryons or by the combination quark-antiquark $q\bar{q}$ in the case of mesons. In addition, the combination of a color neutral $q\bar{q}$ pair with a color neutral qqq system is also possible. The wave function of a baryon can be expressed in terms of a Fock state expansion:

$$|B\rangle = |qqq\rangle(a_0 + a_1|q\bar{q}\rangle + a_2|q\bar{q}q\bar{q}\rangle + \dots + b_1|q\bar{q}g\rangle + \dots), \quad (2.4)$$

where higher order terms represent "sea quarks" which are created by QCD vacuum polarization. As QCD is flavor blind, naively one expects a flavor-symmetric sea. Recent measurements [11, 12] have shown that flavor symmetry in the quark sea is strongly broken.

For all known baryons the valence quark content is reducible to three quarks. For example, in combination of udd with $u\bar{u}$ the final state has quark content $u\bar{u}udd$. The \bar{u} can annihilate with u . Nevertheless, there are combinations, where the quark content can not be reduced to three and subsets of these exist, where the gluons contribute to the ground state quantum numbers - known as an "exotic states" (E.g. $uudd\bar{s}$). Due to the presence of the strange antiquark, there is no possibility of annihilation. An understanding of whether these exotic quark states exist and, if they do exist, what their properties are, is an important piece in the puzzle of understanding QCD in the non-perturbative regime.

2.2.1 Pentaquark Models

The MIT bag model has been developed to explain the non-existence of free quarks. The basic idea is to treat the confinement properties of nucleons in a phenomenological way. The world is divided into "internal" and "external" spaces, which are separated by a thin

surface. In the internal space quarks are massless and free, in contrast to the external space where their mass increases to infinity. On the separation surface, called confinement, the quarks experience the forces of strong interaction. In general, the model provides a satisfactory framework for treating hadrons as a system of confined quarks with residual QCD interaction that needs only be considered in lowest order. Where the details of the confinement mechanism is important however, the models shows some signs of being unsatisfactory.

For the bag model, the existence of multi-quark states has been discussed elsewhere [19, 20, 21]. The parameters of these models were fit to the masses of N , Δ , Ω and ω and resulted in a mass spectrum consistent with observances. Through symmetry conditions the constructed ground states $q^2\bar{q}^2$ and $q^4\bar{q}$ states are members of the flavour nonet. The model predicted that these states would be in a non-exotic ground state and may be mis-identified as normal $q\bar{q}$ or q^3 . Exotics are heavier - their mass has to be above decay threshold into $(q\bar{q})(q\bar{q})$ or $(q\bar{q})(q^3)$. For this reason, the width has to be very broad if, indeed, they are resonant at all. Observation of such states will be difficult.

The MIT bag model was the first which discussed the existence of pentaquark states. There were other models in which the discussion about possible pentaquark existence appeared. These models include, among others, the soliton model in the works of Kopeliovich [22], Chemtob [23] and Walliser [24].

2.2.2 Diakonov, Petrov & Polyakov Predictions

The most recent experimental search for the pentaquark was started by a prediction of Diakanov, Petrov and Polyakov [25]. They predicted a narrow pentaquark resonance with a mass of 1530 MeV and width Γ of about 15 MeV.

The prediction arose through consideration of the Quark Soliton Model, which is based on the Skyrme idea [26, 27], where nucleons can be interpreted as solitons of the pion field. The classification of the light baryons as the rotational states of the soliton is the strength of the model. Performing rotation in ordinary and in the $SU(3)$ space (and its quantization), the lowest baryons are classified as members of the octet (spin 1/2) and decuplet (spin 3/2).

The authors considered the next rotational excitation of solitons. The next excitation in the three-flavor case should be an anti-decuplet with spin 1/2. They identified

known nucleon resonance $N(1710)$ as a member of the anti-decuplet. The scheme of the anti-decuplet is shown in Fig. 2.2, where the naive interpretation of quark contents is in-

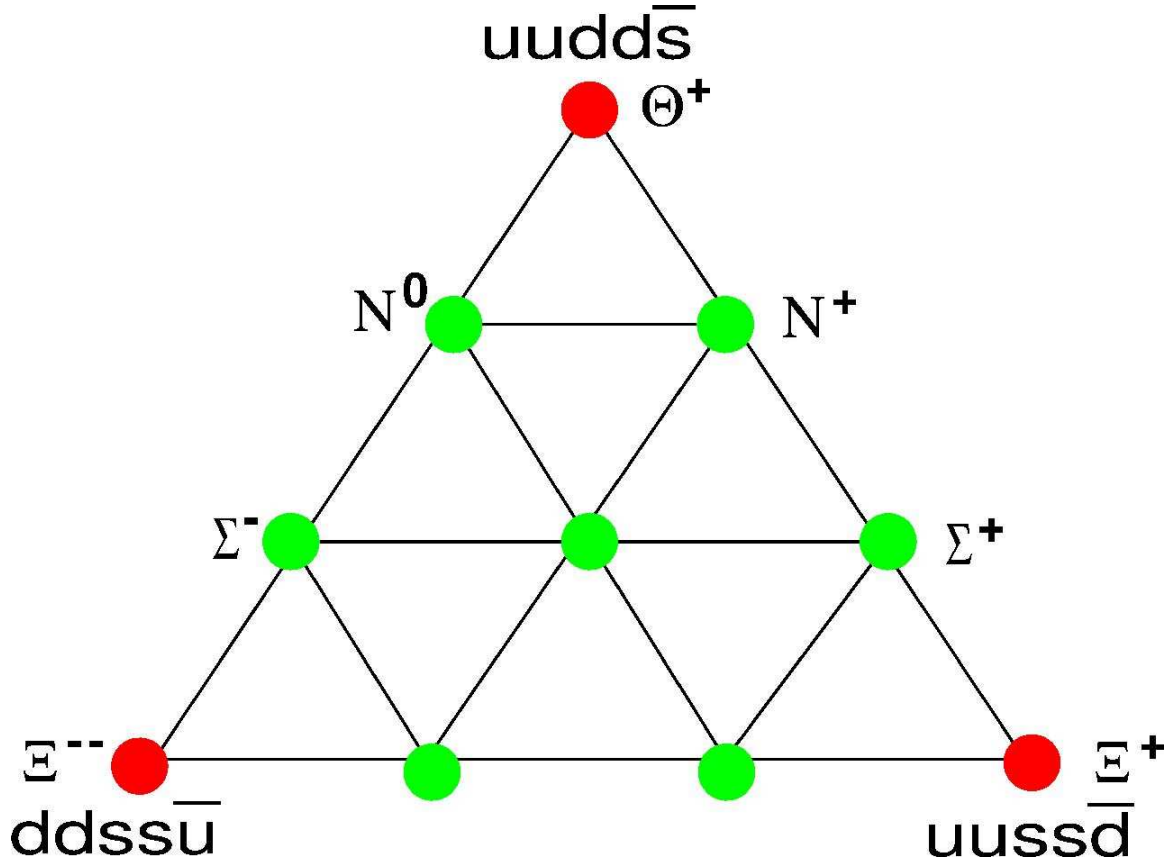


Figure 2.2: Anti-decuplet of baryons. The corners of this diagram are manifestly exotic.

indicated by coordinate system T_3, Y . The candidates for exotic pentaquarks are located in the corners of triangle. In the top corner is the Θ^+ with quark content $uudd\bar{s}$, in the left bottom there is hyperon Ξ^{--} with content $ddss\bar{u}$ and in right corner the hyperon Ξ^+ with $uuss\bar{d}$ quarks. The other members of anti-decuplet are not exotic.

Using $N(1710)$ as a foundation on which to build, the mass and width values of members laying on the anti-decuplet right side have been predicted. The exotic member denoted as Θ^+ has been predicted with a mass of 1520 MeV and a width of 15 MeV. The second non-exotic member has been predicted with a mass of 1890 MeV and a width about 70 MeV. This resonance can be identified as the observed $\Sigma(1880)P_{11}$ state. The second exotic member on this side line has a predicted mass of 2070 MeV and a width larger then

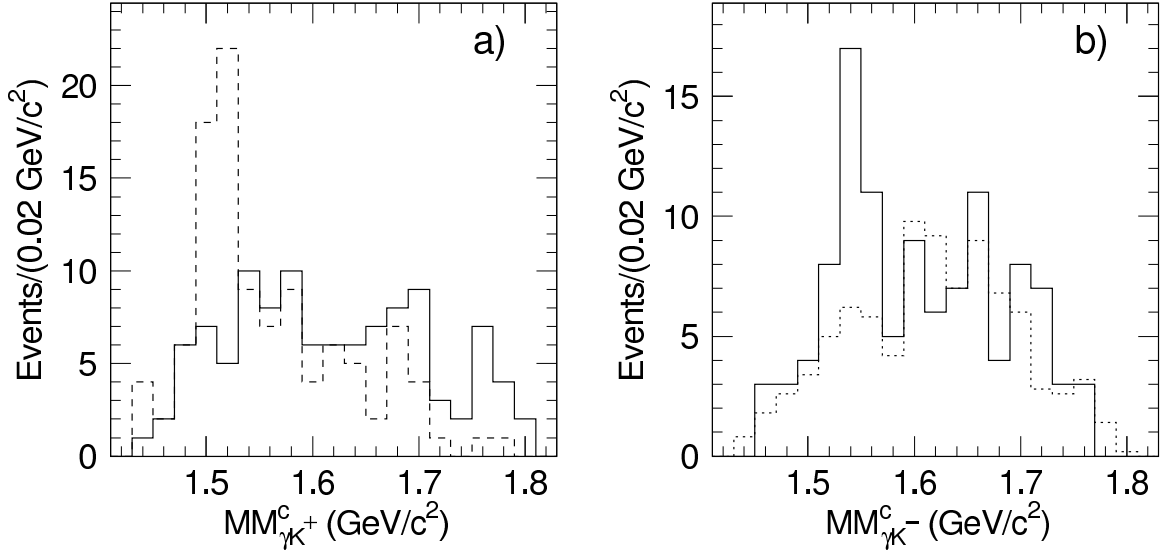


Figure 2.3: The first observation of the Θ^+ by the LEPS experiment [31]. Left panel a) shows the missing mass $MM_{\gamma K^+}^c$ spectrum for K^+K^- production for the signal sample (solid histogram) and for events which are accompanied with a proton hit. Right panel b) shows $MM_{\gamma K^-}^c$ for the signal sample (solid histogram) and for events accompanied with a proton hit (dotted histogram).

140 MeV. As a possible candidate, the observed $\Xi(2030)$ is proposed, however the quantum numbers of this state are not well established yet.

2.3 Experimental Results

2.3.1 Evidence for the Θ^+

In this subsection, an overview is given that describes the current status of the experimental search for pentaquarks. For review reports about experimental searches for pentaquarks see [28, 29, 30]. The first observation of the candidates came from the LEPS collaboration at the SPring-8 facility in Japan [31]. The reaction $\gamma n \rightarrow K^+K^-n$ on a ^{12}C target has been investigated with a γ energy between 1.5 and 2.4 GeV/c². An observed sharp resonance in the reconstructed channel K^+n exhibits a mass of 1.54 ± 0.01 GeV/c² and a width smaller than 25 MeV/c². The significance of the peak has been estimated at 4.6σ . The decay channel requires a strangeness quantum number $S = +1$. The resonance has been interpreted as the 5-quark state with configuration $|uudd\bar{s}\rangle$. The spectra of the

observed resonance is shown in Fig. 2.3. The recent preliminary analyses of the LEPS data confirmed the existence of the state. The peak contains 90 entries in comparison to the 19 published in the first report.

The first observation of an exotic narrow resonance at the LEPS experiment incited an intensive search among other experiments. The candidates for the Θ^+ have been observed in different reactions channels. The results are summarized in the Table 2.2 and plotted in Fig. 2.4.

The second experiment which reported [32] positive evidence of the Θ^+ state was DIANA at ITEP. The reaction $K^+Xe \rightarrow K^0pXe'$ was analyzed. The K^0 is decaying into $\pi^+\pi^-$ pair and the tracks of these, and of the p , were detected in an Xe bubble chamber. The invariant mass of the K^0p system was reconstructed. The observed narrow peak has a mass of $1.539 \text{ GeV}/c^2$ and a width $9 \text{ MeV}/c^2$.

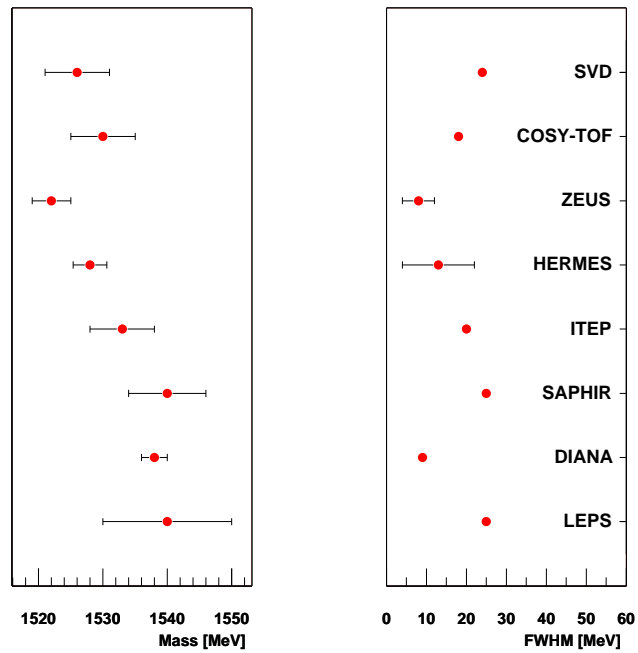
The reaction $\gamma p \rightarrow nK_S^0K^+$ was measured at the SAPHIR experiment at ELSA [33]. The liquid hydrogen target was bombarded with photons with energies between 0.87 GeV and 2.63 GeV . The K_S^0 was identified by the decay channel $K_S^0 \rightarrow \pi^+\pi^-$ whereas neutron by a kinematical fit and momentum conservation laws, while the SAPHIR detector could only detect charged particles. A peak with a mass of $1540 \text{ MeV}/c^2$ and a width lower than $25 \text{ MeV}/c^2$ was found in the reconstructed invariant mass spectrum of the nK^+ system.

Five different neutrino experiments have been analyzed by the ITEP group [34]. The $\nu A \rightarrow K^0pX$ reaction has been measured by means of bubble chambers, where A represents either hydrogen H , deuterium D , or neon Ne . The resulting peak shows 20 counts above background (12 counts) at a mass of 1533 MeV . This gives a realistic statistical significance of 3.5σ .

The ZEUS experiment at DESY measured the reaction $e^+p \rightarrow e^+K^0pX$ at a center-of-mass energy of about 300 GeV . The observation of a peak near to a value of 1522 MeV has been reported [35]. The peak is seen for events with 4-momentum transfer $Q^2 > 20 \text{ GeV}^2$ with statistical significance of 5σ . In the case of a sample where 4-momenta transfer $Q^2 > 1 \text{ GeV}^2$, no peak is visible.

Good evidence for the Θ^+ baryon has been reported by the COSY-TOF experiment [36]. Using the exclusive hadronic reaction $pp \rightarrow K^0p\Sigma^+$ from two different runs with slightly different energies, the measurement of Σ^+ in the final state can act as a tool for tagging strangeness. The result is a very clean final state showing a Θ^+ peak at mass

Reaction	Mass [MeV]	FWHM [MeV]	σ 's	Group	Ref.
$\gamma C \rightarrow K^+ K^- X$	1540 ± 10	< 25	4.6	LEPS	[31]
$K^+ Xe \rightarrow K^0 p X$	1539 ± 2	< 9	4.4	DIANA	[32]
$\gamma d \rightarrow K^+ K^0 (n)$	1540 ± 6	< 25	4.8	SAPHIR	[33]
$\nu A \rightarrow K^0 p X$	1533 ± 5	< 20	6.7	ITEP	[34]
$e^+ d \rightarrow K^0 p X$	1528 ± 2.6	13 ± 9	5	HERMES	[18]
$e^+ p \rightarrow e^+ K^0 p X$	1522 ± 3	8 ± 4	5	ZEUS	[35]
$pp \rightarrow K^0 p \Sigma^+$	1530 ± 5	< 18	4-6	COSY-TOF	[36]
$pA \rightarrow K^0 p X$	1526 ± 5	< 24	5.6	SVD	[37]

Table 2.2: Published experiments with evidence for Θ^+ resonance.Figure 2.4: Compilation of the world data observed Θ^+ . Left panel shows the mass values and the right plot shows the FWHM.

of about 1.53 GeV, with a statistical significance of between 4 and 5 σ .

The last reported observation of the Θ^+ baryon comes from the SVD collaboration at IHEP. In the most recent report [38], reanalyzed data [37] for the reaction $pA \rightarrow K^0 pX$ using protons of 70 GeV is presented. The observed peak in the pK system exhibits a mass of about 1.523 MeV. This result shows the highest significance amongst all the reported observations of the Θ^+ baryon.

2.3.2 Non-Evidence for the Θ^+

Low statistics are one of the common features of an experiment returning a positive signal for Θ^+ . Evidence for the “observed” peak is very close to that for a statistical fluctuation. Proof for the existence of Θ^+ rests on an experiment with higher statistical significance. Experiments with higher rates of particle productions would, one would hope, may throw more light on the situation. However, most such experiments them reported negative results. An overview of published non-observation of the Θ^+ baryon is shown in Table 2.3.

Non-observance has been reported by the e^+e^- collider experiments BaBar[39] , Belle[40] and ALEPH [41] which performed search by reconstruction of the pK_S^0 systems in the final states. The BES collaboration investigated the $e^+e^- \rightarrow J/\Psi \rightarrow \bar{\Theta}\Theta$ reaction [42]. The level of statistics obtained in the lepton colliding experiments is an order of magnitude higher than in the experiments with positive test results. The simplest explanation would be that the low statistics experiments are wrong in this case. The situation is more complicated if we assume that they are, in fact, correct. One solution is offered in a BaBar report [39]. They found that hadron production rates decrease smoothly as the mass increases. For baryons, this fall is steeper than for mesons. This baryon rate suppression may be naively explained in the following way. In e^+e^- collisions a pair $q\bar{q}$ is produced initially which is then hadronized. In order to produce a baryon, two other pairs of quarks have to be produced from the vacuum, rather than the single pair needed for meson production. The question of whether the suppression factor increases in the production of particles containing more quarks is a valid one. Unfortunately there is no theory which can give clear guidance. The experiments BaBar, Belle and LEP give us limits for the production, but they cannot rule out the existence of the Θ^+ .

There are other high energy hadron beam experiments from other groups, other

Reaction	Limit	Group	Ref.
$e^+e^- \rightarrow \Upsilon(4S) \rightarrow pK^0 X$	$< 1.0 \times 10^{-4} \mathfrak{B}\mathfrak{r}$	BaBar	[39]
$e^+e^- \rightarrow B^0 \bar{B}^0 \rightarrow p\bar{p}K^0 X$	$< 2.3 \times 10^{-7} \mathfrak{B}\mathfrak{r}$	Belle	[40]
$e^+e^- \rightarrow Z \rightarrow pK^0 X$	$< 6.2 \times 10^{-4} \mathfrak{B}\mathfrak{r}$	LEP	[41]
$e^+e^- \rightarrow J/\Psi \rightarrow \bar{\Theta}\theta$	$< 1.1 \times 10^{-5} \mathfrak{B}\mathfrak{r}$	BES	[42]
$pA \rightarrow K^0 pX$	$< 0.02 \times \Lambda^*$	HERA-B	[43]
$pCu \rightarrow K^0 pX$	$< 0.3\% K^0 p$	HyperCP	[44]
$p\bar{p} \rightarrow K^0 pX$	$< 0.03 \times \Lambda^*$	CDF	[45]
$pC \rightarrow K^0 \Theta^+ X$	$< 0.1 \times \Lambda^*$	SPHINX	[46]
$\pi + Si \rightarrow K^0 pX$	$< 0.02 \times \Lambda^*$	Belle	[47]
$e + Be \rightarrow pK^0 + X$	not given	BaBar	[48]
$d + Au \rightarrow K^- \bar{n} X$	not given	PHENIX	[49]
$\gamma p \rightarrow \bar{K}^0 K^+ n$	$< 0.002 \times \Lambda^*$	CLAS	[50]
$\gamma d \rightarrow K^+ K^- pn$	not given	CLAS	[51]
$\Sigma^- A \rightarrow K^0 pX$	$\mathfrak{B}\mathfrak{r} \cdot \sigma_0 < 1.8 \mu\text{b}$	WA89	[52]

Table 2.3: Published experiments with non observation of the Θ^+ resonance.

than the e^+e^- experiments, that claim non-observation of the Θ^+ : HERA-B with a 920 GeV proton beam on a carbon target [43]. The HyperCP experiment at Fermilab is designed to measure CP violation in cascade (Ξ) and anti-cascade decays. They sought for Θ^+ in reactions of protons and π^+ with tungsten collimators [44]. The incidence momenta of protons or pions is in the range 100-250 GeV/c. The CDF experiments studying $p\bar{p}$ collisions at an energy of 2 TeV published null results as well [45].

Contradictory to the SVD, the SPHINX collaboration reports no evidence of the Θ^+ resonance decaying into pK^0 system [46]. The experiment is using the same 70 GeV proton beam on a nuclear target.

Parallel to the analyses of the e^+e^- reaction, Belle and BaBar analyzed reactions coming from the interaction of the beam with surrounding material. Belle used secondary scattering of mesons in their silicon vertex detector [47], while BaBar analyzed interactions of positrons with the beam pipe [48]. Both experiments reported null results.

The last non-observation of Θ^+ was reported by the PHENIX collaboration [49] through analysis of the reaction $d + Au \rightarrow K^- \bar{n} X$ at $\sqrt{s_{NN}} = 200$ GeV.

The CLAS collaboration at the Thomas Jefferson National Accelerator Facility in the first report observed a narrow baryon peak in the exclusive reaction $\gamma d \rightarrow K^+ K^- pn$ [53]. The neutron in the final state was reconstructed by missing mass techniques since the incident photon energy was known from the tagging system. The resulting invariant mass spectrum of the $K^+ n$ system showed a sharp peak at the mass 1.542 GeV/ c^2 with a FWHM value of 21 MeV/ c^2 . Significance of the peak was estimated at 5.2σ . Further evidence for the Θ^+ was reported in [54] in the $\gamma p \rightarrow \pi^+ K^+ K^- (n)$ channel. In the last year, CLAS has performed a dedicated run aimed to search for Θ^+ . The reported results [50] show non-observation of a resonance in the range between 1.525 to 1.555 MeV for the $\gamma p \rightarrow \pi^+ K^+ K^- (n)$ reconstructed channel. The preliminary results [51] show the same for $\gamma d \rightarrow K^+ K^- pn$ channel.

2.3.3 The Search for Other Candidates

The predicted Θ^+ baryon resonance is assumed to be an iso-singlet. However the search has been performed for iso-vector state with charge $Q = +2$ as well. No experimental observation of Θ^{++} has been reported except by the STAR collaboration at RHIC [55]. The channel pK^+ was investigated in a dAu collision sample. The observed peak of a mass about 1530 MeV exhibits significance of 5σ . Assuming that Θ^{++} is real, the Θ^+ must also be seen. In their published results, the STAR collaboration shows a small peak with low significance in the pK_S invariant mass spectrum, shifted by about 10 MeV/ c^2 to higher mass.

As mentioned above, the anti-decuplet corners in Fig. 2.2 represent the exotic states. The search for the Ξ_5 has been performed by several experiments [45, 57, 58, 59, 60, 61, 62] without positive results. Up to now, there is only one reported candidate for Ξ^{--} by NA49 [63], which makes the existence of a Ξ^{--} with a reported mass of 1862 MeV doubtful.

Only pentaquark candidates with strange quark content have been discussed so far. Pentaquarks built from other flavors are possible as well, however the search for candidates with charm quark content has been performed in the last years by several experiments. Only H1 reported a signal corresponding to a $\Theta_c^0(3100)$ [64]. ZEUS and FOCUS claim incompatibility of their results with H1 findings.

2.4 Current Status

There were several theoretical works which searched for an explanation of the observed peak. In a quark-model approach Jaffe and Wilczek [65] explored the possibility of di-quark attraction strong enough to form a new stable hadronic state. Two highly correlated ud -pairs are coupled to an anti-quark, with the lowest states having $J^P = \frac{1}{2}^+$. An octet of di-quark pentaquarks was predicted to accompany the antidecuplet, and it was suggested that charm and bottom analogs to the Θ^+ might also be stable against strong decay.

Different example of an explanation comes from since a majority of experiments claiming observation of the Θ^+ were using a nuclear target. Gal and Friedman [66] studied the possibility of formation of Θ^+ by means of the K^+ - nucleus phenomenology.

No contribution of the lattice community brought any enlightenment on current situation. Results of 10 groups are compiled in [67]. The studies show that the most complicated problem for the lattice calculation is to distinguish a simple KN continuum scattering state from a Θ^+ pentaquark. About half of the results reported a pentaquark structure, while the others did not. The next discrepancies to be considered will be regarded to estimation of the spin and parity.

It is difficult to find a correct explanation for the contradictory results of the searches for Θ^+ . In view of the non-observations in high energy hadronic experiments with high statistics one may simply conclude that Θ^+ doesn't exist. On the other hand, this conclusion assumes that several low energy experiments are all wrong about a peak at about 1530 MeV which would be a surprising coincidence. The solution to this conundrum could be found in an examination of the possible production methods for a Θ^+ . A step in this direction was taken by Titov et al. [68]. Using well-known high energy phenomenology like energy dependence of the Regge trajectories and the scaling behavior of the hadronic amplitudes they found that the Θ^+ production cross section, when compared to conventional three quark hyperon, is (at high energy processes) strongly suppressed.

Although there is lot of effort to find theoretical explanations of the situation, the crucial question either this strange pentaquark exists or not can only be answered by experiments.

Chapter 3

The HERMES Experiment

3.1 The HERA Accelerator

The HERA accelerator at DESY, Hamburg, provides two beams - one of 920 GeV protons and one of 27.5 GeV electrons or positrons. In addition to HERMES, these are used for two collider experiments ZEUS and H1. The HERMES experiment is located in the East experimental hall, diametrically opposite to the HERA-B hall. It is one of two fixed target experiments. Collider experiments ZEUS and H1 are investigating nucleon structure functions by means of unpolarized deep inelastic scattering over a wide kinematic region. The goal of HERA-B experiment was to study CP-violation in B -meson production in proton-proton collisions.

HERMES (HERa MEasurement of Spin) [69] is designed for precise measurement of nucleon spin structure. This is accomplished by means of analyzing semi-inclusive spin asymmetries in polarized Deep-Inelastic lepton-nucleon Scattering (pDIS). Beam currents of up to 50 mA at the beginning of a fill have been achieved. Due to residual gas interactions, the beam current decays nearly exponentially. The average lifetime, which can be derived from the decay constant, is between 12 and 14 hours. Usually the beam is dumped earlier by inserting high density gas in the HERMES target cell in order to obtain high number of statistics for unpolarized DIS (important for the study of nuclear effects).

The electron beam is distributed within 220 bunches along the HERA storage ring's 6.3 km circumference. The polarization of the beam is achieved by the Sokolov-Ternov effect, which is caused by a small asymmetry in the synchrotron radiation. The theoretical limit for polarization is 92.4%. The real polarization reaches about 55% approximately 40

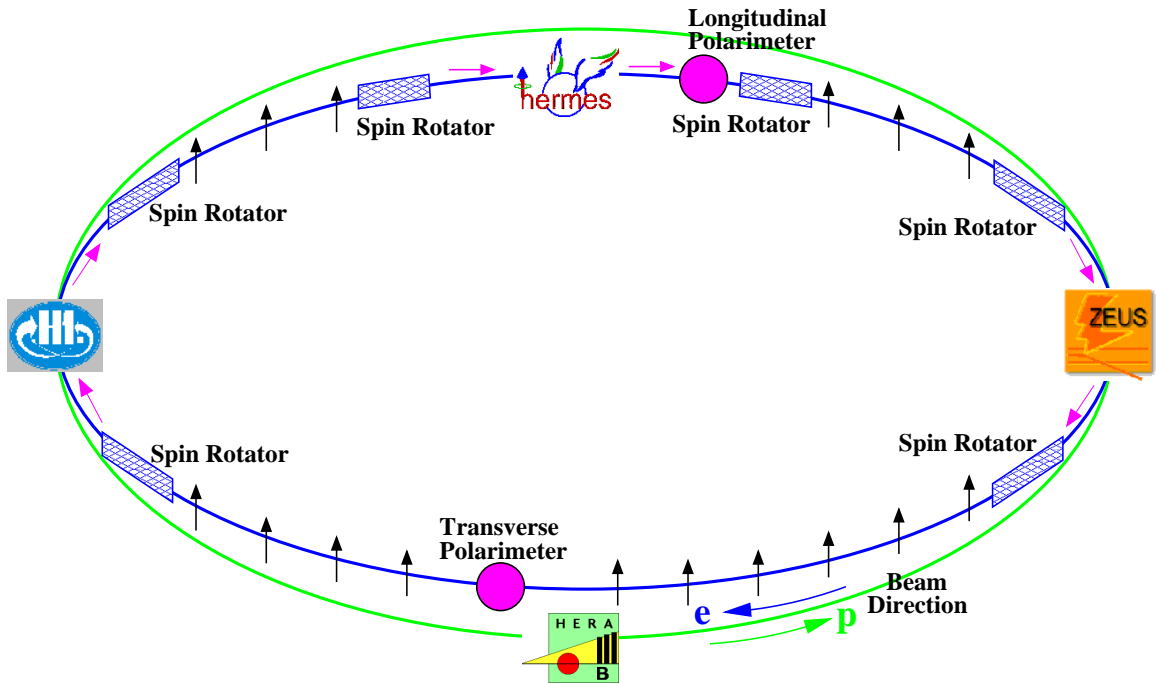


Figure 3.1: Location of HERMES at the HERA storage ring. The other experiments H1, HERA-B and ZEUS, the Spin rotators and polarimeters are superimposed. The setup of run 2001-2007 is shown. Prior to 2001 there were no rotators at H1 and ZEUS.

minutes after the fill start.

Spin rotators have been installed upstream and downstream from the HERMES experiment (see Fig. 3.1), since for the measurement of the beam spin asymmetries, longitudinal polarization is required in contrast to polarization in the storage ring which is in the transverse direction. The spin rotators at H1 and ZEUS were installed in addition during the shutdown of 2001. The polarization of the beam is measured by two laser backscattering polarimeters. The transverse polarimeter is located in the West Hall and longitudinal polarimeter is inside the spin rotator at the East Hall.

3.2 The HERMES Target

HERMES was intended to run alongside ZEUS and H1 without causing significant disruption to the beam lifetime, requiring a fill to remain for at least 10 hours. This immediately excluded any possibility of using solid material for the target in HERMES. In

fact, the target density is limited to 10^{15} atoms/cm². Thus a gaseous target cell intended to sit inline to the storage ring was designed for use in the experiment.

The HERMES experiment uses both polarized and unpolarized targets. The polarized target consists of Hydrogen, Deuterium or ³He, whilst the unpolarized gases are one of H₂, D₂, ³He, ⁴He, N₂, Ne, Kr, and Xe. A polarized ³He target was used in 1995 but during 1996 - 1997 a longitudinally polarized hydrogen target was used and in 1998 - 2000 longitudinally polarized deuterium. In 2001, a transversally polarized target was installed during a HERA upgrade.

The polarized hydrogen(deuterium) beam is produced by means of an atomic beam source (ABS) [70]. This device consists of dissociator, powerful differential pumping system, beam forming system, sextuple magnet system and adiabatic high-frequency transitions.

Molecular hydrogen/deuterium gas is dissociated by a radio frequency of 13.56 MHz in a pyrex-type tube. The degree of produced dissociation is up to 80 %. Atomic gas flows through a conical nozzle with an opening of diameter 2 mm, which is cooled to 100 K. Five sextupole permanent magnets split this beam into hyperfine states. The particular polarization state of interest is selected by combination of strong field transition (SFT), medium field transition (MFT) and weak field transition (WFT). The polarized atomic beam is injected into target cell with a pressure of about 10^{-7} mbar. The target cell is an elliptical tube with open ends which holds the gas at the lepton beam position. At the end of the target cell two powerful turbo-pumps are installed in order to protect ultra high vacuum in the accelerator ring.

For polarized gas, there are two instruments installed for monitoring a Breit-Rabi Polarimeter (BRP) and Target Gas Analyzer (TGA). The former measures the polarization of the gas and the latter gives an estimate of the degree of dissociation. For unpolarized gas, neither measurement makes sense, so the gas is filled directly into the target cell.

The HERMES detector [69] is constructed as a spectrometer with a dipole magnet. The symmetry planes of the electron and proton beam pipes divide the detector into upper and lower halves. The complex system of detectors that make up the spectrometer allow the detection of properties for any registered particle (see Fig. 3.2). The largest component of the HERMES spectrometer is a large dipole magnet with an integrated field strength of 1.3 Tm. Acceptance of the spectrometer is given by the opening angle of the spectrometer magnets. This angle is ± 170 mrad in the horizontal direction and 140 mrad in the vertical. Protection of the electron and proton beams against strong magnetic field is accomplished

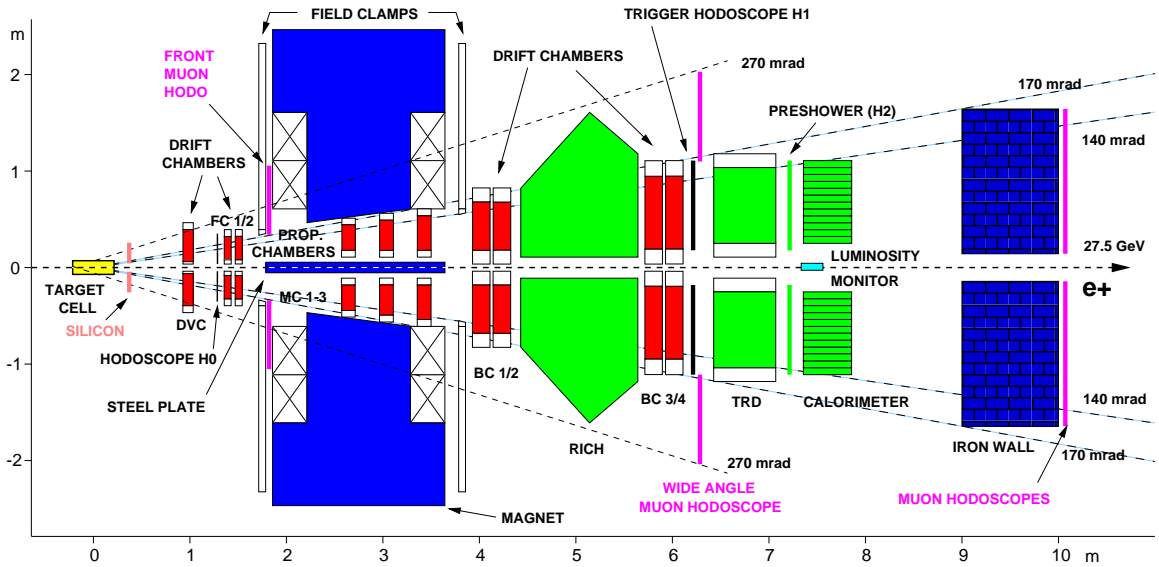


Figure 3.2: Side view of the current setup of the HERMES spectrometer

by a septum plate which limits acceptance for small vertical scattering angle to 40 mrad.

3.3 Tracking Detectors

The deflection of the charged particles by magnetic field is used for measurement of their momenta. This is accomplished by measuring the particles' track in the magnetic field region of the spectrometer. Tracking detectors measure a full complement of track information for any registered particle: the scattering angle (θ), the azimuthal angle (ϕ) and the vertex position. The tracking detector system is depicted in Fig. 3.2. In front of the magnet there is set of drift chambers. Two are called the Front Chambers (FC1/2) [71] and the third is called the Drift Vertex Chamber (DVC). They are used for determination of the initial trajectory in the front region. Four drift back chambers (BC1-4) [72] behind the magnet provide tracking after the deflection of the particle by means of the magnetic field. Three proportional chambers (MC1-3) [73] located within the opening of the magnet are used for the reconstruction of the tracks with low momenta that are deflected out of the spectrometer acceptance. Each space point determined by a tracking detector is defined by three co-ordinates: horizontal(x) and two at stereo angles $\pm 30^\circ$ (u, v). This is given by orientation of the wires in the chambers.

The drift chambers are constructed with the same principle but their size increases with distance from the target. Each chamber is assembled as a module with six layers. One layer consists of a plane of alternating anode/cathode wires between a pair of cathode foils. The cathodes are at negative voltage and the anodes are connected to ground. The wires are oriented vertically in the X plane and at stereo angles $\pm 30^\circ$ for planes U and V . One block is compound from pair of layers. Within the block, each layer is staggered with respect to their partner by half a cell size in order to help resolve left-right ambiguities.

The choice of gas mixture for the drift chambers was governed by the serious problems presented when needing to control a flammable gas in a tunnel environment. All drift chambers are operated with the same $Ar(90\%)/CO_2(5\%)/CF_4(5\%)$ gas mixture which is fast and non-flammable. Its drift velocity is about $70 \mu\text{m}/\text{ns}$ at the average field strength of $E = 800 \text{ V}/\text{cm}$. The readout of the drift chamber is accomplished by the Amplifier-Shaper-Discriminator card (ASD) connected to the Fastbus Multi-hit Time-to-Digital-Converter (TDC) with a time resolution of 0.5 ns .

For the multi-wire proportional chambers within the magnet opening, the same gas mixture as in the Drift Chamber is used, but with the mix ratio recalculated for optimization during MWPC operation: $Ar(65\%)/CO_2(30\%)/CF_4(5\%)$. The readout is based on the LeCroy PCOS IV system. An on-chamber cards provide amplification, discrimination and delay as well as latching to the event trigger. The MCs provide a spatial resolution of about $700 \mu\text{m}$.

In 2001, a silicon detector system named the “Lambda Wheel” (LW) was installed in the front of the spectrometer magnet with the intent of increasing the acceptance of HERMES to pions from Λ decays.

Tracking reconstruction uses a tree-search algorithm. The algorithm is based on the use of a pattern database that contains all possible particle tracks for a given detector system and resolution. The recorded hits from each detector are encoded in a bit pattern. A one dimensional bit array is created and these arrays are combined into two-dimensional pictures for all chambers with the same wire orientation. The detector pattern is compared to the pattern database and combinations that could not have been caused by straight tracks are filtered out. The iterative process starts with a “2-bit detector” that differentiates between a hit in the left or right side of the detector. In each step, the resolution of the bit pattern is doubled. After 11 iterations, the track is completely determined. The tree-search algorithm finds straight tracks separately in the front and back regions of the

spectrometer. The partial tracks are combined into tracks going through the magnetic field of the spectrometer. The Hermes Reconstruction Program (HRC) uses several methods for this. The momentum of the tracks is determined from a look-up table, generated only once during the initialization of the program, saving the computing time to calculate the momentum from the deflection in the magnet. The momentum resolution of the experiment for positrons is 0.7-1.25 %. The uncertainty in the scattering angle is about 0.6 mrad.

3.4 Particle Identification

Particle Identification (PID) is an important factor in the measurement of DIS. The HERMES experiment provides excellent hadron-lepton separation. This is accomplished by sub-system detectors which are the lead-glass Electromagnetic Calorimeter, the Preshower Detector, the Transition Radiation Detector (TRD) and the Ring Imaging Čerenkov Detector (RICH).

Different types of interaction take place as a particle passes through matter. Charged particles produce mainly ionization or bremsstrahlung. The amount of energy lost by these two processes depends on the momentum, mass and charge of the interacting particle and on the material through which the particle passes.

Electrons or positrons under the influence of the electromagnetic field of an atom radiate a high energy bremsstrahlung photon. Such photons interact with electromagnetic fields in the matter in which they were produced and, in turn, produce pairs of e^+e^- . It is possible to use this chain reaction to create electromagnetic showers in a material. This is typical behavior for a lepton, but heavier particles do not cause such showers as the process is inhibited due to their mass. Using such a material to create showers allows lepton-hadron separation inside the calorimeter and preshower detector.

The HERMES calorimeter [74] measures the energy of incident lepton or photons. It is built from 840 radiation resistant F101 lead-glass blocks which are arranged into two 42×10 arrays for top and bottom detector parts. Each block is of size $9 \times 9 \times 50\text{cm}^3$. The length of the calorimeter blocks corresponds to 18 radiation lengths. The hadron-lepton separation in the calorimeter is based on the fact that electrons deposit all their energy in the calorimeter. The ratio E/p is, for electrons, equal to one. Hadronic showers develop more slowly than electromagnetic ones, therefore the ratio E/p is less than one. Neutral photons are stopped in the calorimeter as well. Since photons do not produce ionization along their

track in the detector, they are identified as a hit in the calorimeter and a corresponding missing hit in the hodoscope system. The resolution of the HERMES calorimeter is

$$\frac{\sigma(E)}{E} [\%] = 1.5 + \frac{5.1}{\sqrt{E[\text{GeV}]}} \quad (3.1)$$

Similar processes to bremsstrahlung can occur if a particle passes the boundary between two media with different dielectric constants. In this case, an electromagnetic wave is emitted. The photons are usually emitted in the visible part of the spectrum but an X-ray may be emitted as well. To increase the probability of the emission of X-ray photons in the Transition Radiation Detector (TRD), a high number of boundaries are introduced. The ideal case would be a set of thin foils with a narrow uniform separation by vacuum. Such a construction is technically difficult. In the HERMES TRD it is replaced by packets of pseudo-randomly arranged polypropylene/polyethylene fibers with diameters of 17-20 μm . The fiber material is held in place with an aluminum frame and stitched together to maintain the proper density. The radiator blocks are 6.35 cm thick, 3.4 m wide and 0.8 m high. The detection of X-rays is accomplished by Multi-Wire Proportional Chambers (MWPC) with a gas mixture 90% Xe and 10% CH₄ behind the radiator. The HERMES TRD consists of six modules each consisting of a radiator block and a MWPC.

The selection of leptons from hadrons is done by combining the information from all PID detectors. The probability functions $P_i^j(p, x)$ (where the particle i with momentum p causes a response x in the detector j) are calculated. This is accomplished by comparing detector response to so-called “parent distributions”. The parent distributions are obtained from data and Monte-Carlo simulations. By combining the probability functions of the calorimeter and the preshower, a likelihood ($rPID3$) is obtained:

$$rPID3 = \log_{10} \frac{P_{Cal}^e P_{Pre}^e}{P_{Cal}^h P_{Pre}^h}. \quad (3.2)$$

The $rPID3$ is the logarithmic likelihood that a certain particle has been identified by the calorimeter and the preshower as a lepton, rather than a hadron. The same method is used for the calculation of the value $rPID5$ in the case of the TRD, where each module is treated as an independent detector:

$$rPID5 = \log_{10} \frac{\prod_{i=1}^6 P_{TRD_i}^e}{\prod_{i=1}^6 P_{TRD_i}^h}. \quad (3.3)$$

The sum of PID parameters, $rPID3 + rPID5$, is used for hadron selection. The efficiency of lepton-hadron separation is better than 98% with a contamination of less than 1%.

When travelling through a material with a speed higher than the speed of light in that material, charged particles emit photons in a process known as “Čerenkov Radiation”. The minimal momentum p for the Čerenkov Radiation is given by

$$p = \frac{m}{\sqrt{(n^2 - 1)}} \quad (3.4)$$

where m is the mass of the particle and n is the diffractive index of the medium. This is used in threshold Čerenkov counters. In addition the Čerenkov angle, θ_C , of the radiated photons (i.e. the angle with respect to the direction of the particle) is given by:

$$\cos \theta_C = \frac{1}{n\beta} \quad (3.5)$$

where n is the again diffractive index of the medium and $\beta = \frac{v}{c}$ (c is the speed of light in vacuum and v is speed of the particle in the medium). In the RICH detectors, the Čerenkov cone is focused on the matrix of photon detectors where a ring pattern is created. The diameter of the ring is proportional to the Čerenkov angle θ_C .

The charged hadrons in the HERMES experiment have momenta in the range 2-20 GeV/c. In order to achieve reasonable PID over the full range of momenta, a dual radiator RICH [75] was designed. The first radiator is a wall made from aerogel tiles. The wall is built from 425 tiles of size $11 \times 11 \times 1.0$ cm. The refractive index of the aerogel is 1.0303, thus the aerogel wall can cover PID within the lower part of the accepted momentum range. The second radiator is a C_4F_{10} gas with refractive index 1.00137. The gas fills the space of the RICH housing between the aerogel wall and the mirror. The mirror (radius of curvature of 220 cm) reflects and focuses Čerenkov light on to the PMT plane. The PMT plane contains 1934 Philips XP1911 type PMTs which are read out by the PCOS4.

The RICH particle identification is based on reconstruction of the Čerenkov angle and information about particle momentum. As mentioned above, the particle momentum is estimated by track reconstruction in BC and FC and deflection radius in the spectrometer magnet. The Čerenkov photons are detected by the RICH PMTs and all this information together can be used to reconstruct the Čerenkov cone.

Direct and Indirect Ray Tracing Methods (DRT and IRT) are used for reconstruction of the Čerenkov rings. For each hit in the PMTs matrix, the point of emission is estimated by means of the reconstructed track in the BC. Using information about the position of the mirror center, the emission point, the point of light detection and the direction of the particle, the Čerenkov angle is calculated. After reconstruction of the angle

by the tracing methods, likelihood algorithms are applied. They take into account both the Čerenkov angles and the number of fired PMTs. The likelihood is calculated for each hypotheses that light was emitted by π , K , or p . The diameter of the imagined rings for certain particles depends directly on the angle of the Čerenkov cone. Dependence of the Čerenkov angle θ_C on the hadron momentum for the HERMES RICH is shown in Fig. 3.3. The type of particle identified is that whose hypotheses is most probable. The quality pa-

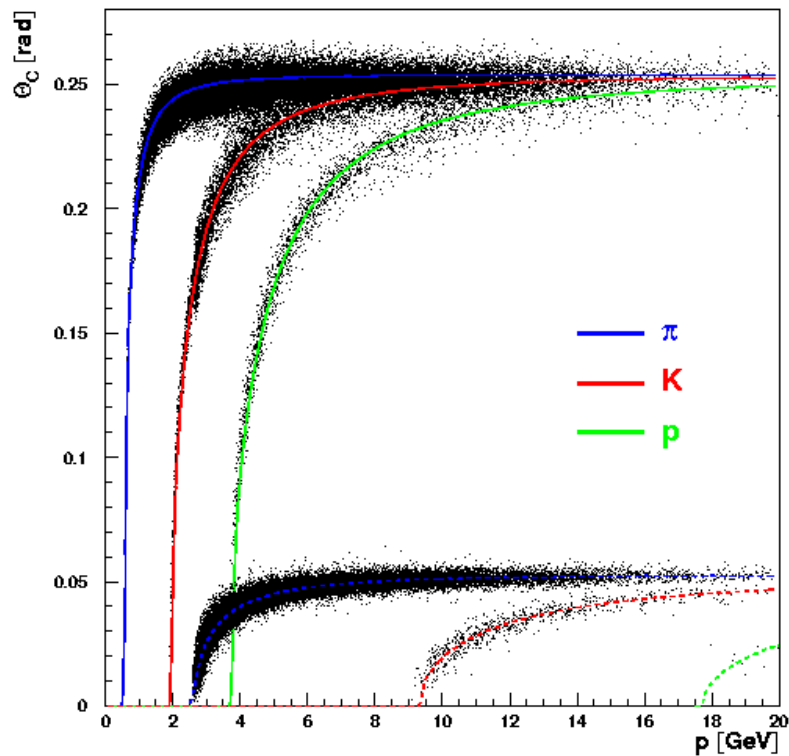


Figure 3.3: Čerenkov angles versus momentum for aerogel and C_4F_{10} gas. The upper curve shows angles of the Čerenkov light cone coming from the aerogel radiator. The lower curve corresponds to the C_4F_{10} gas.

parameter Qp is calculated as a difference of logarithms of the highest and the second highest likelihoods.

$$Qp = \log_{10} \frac{L_1}{L_2} \quad (3.6)$$

3.5 Beam Monitoring

Precise knowledge of the luminosity play an important role in DIS studies. The relative luminosity is required for estimation of cross-section asymmetries in DIS with different target or beam spin states. The absolute luminosity is necessary for the measurement of absolute structure functions or studies of unpolarized semi-inclusive hadron production. The luminosity measurement is based on the observation of elastic scattering of the beam positrons off the target gas electrons $e^+e^- \rightarrow e^+e^-$ (Bhabha scattering) and their annihilation into photon pairs $e^+e^- \rightarrow \gamma\gamma$. When an electron beam is used, electron-electron elastic scattering $e^-e^- \rightarrow e^-e^-$ (Möller scattering) is measured. Since the cross-sections of these processes are calculable using Quantum Electrodynamics (QED) techniques and the electron density in the target is the same as the nucleon density, the luminosity can be extracted from its measurement. By measuring event rates R , the luminosity L is given as:

$$L = \frac{R}{\int_{\Delta\Omega} \Omega \epsilon (d\sigma/d\Omega)} \quad (3.7)$$

where ϵ is detection efficiency and the integration is performed over an acceptance angle $\Delta\Omega$. The forward scattered electrons passing an opening in the septum plate are detected by a luminosity detector [76].

The rates are estimated in the following way. The septum plate opening determines the acceptance of the luminosity monitor. The luminosity monitor consists of a pair of electromagnetic calorimeters. Each of these is constructed as a matrix of 4x3 radiation hard $NaBi(WO_4)_2$ (NBW) Čerenkov crystals each of the size 22 mm². Crystals are coupled to photomultipliers and readout is performed by LeCroy ADCs.

Because the beam position has significant influence on the luminosity monitor acceptance, it is measured by a set of beam position monitors [77]. For physics analyses, the measured rates are corrected with respect to the beam position at the moment of the measurement [78].

3.6 Trigger and Data Acquisition

The aim of the HERMES experiment is to measure properties of protons by means of DIS. The trigger setup is optimized to select events with DIS electrons. The trigger signal is generated by several hit sub-detectors: Hodoscopes H0, H1 & H2, and the Calorimeter.

The Hodoscope H0 sits in front of the spectrometer magnet. Due to the small area of the acceptance, it consists of two blocks of plastic scintillator, one above the beam pipe, one below. Each block is read out by means of two photomultipliers from which time and amplitude information is recorded. A particle traveling at the speed of light passes the distance between H0 and H1 within approximately 18 ns. Thus time information allows the analyzer to distinguish between forward- and backward-travelling particles. This eliminates background caused by proton beam showers.

The hodoscopes H1 and H2 are mounted behind the HERMES magnet, just in front of the TRD (H1) and just behind (H2). The counters are composed of 84 vertical scintillator modules, split evenly between the upper and lower parts. Modules are built from fast scintillating material (BC-412 from Bicron Co.). Each module ($9.3 \times 91 \times 1$ cm) is read out by means of a photomultiplier tube coupled via light guides to the outside ends of the scintillator. A 3 mm overlap between the modules ensures full coverage of the acceptance. The average energy deposition is about 2 MeV for H1. The electrons deposit about 20 MeV in H2 due to an 11 mm thick Pb radiator in front of the scintillator.

The main DIS trigger is formed by the coincidence in all upper or lower parts of the hodoscopes and the calorimeter. The threshold for deposited energy in the calorimeter requires a minimum energy of 1.4 GeV, which may vary dependent on run condition. Information on the multiplicities of H1, H2, LUMI hits, back chamber, magnet chamber and muon hodoscope signals can also be read out in order to define additional types of trigger, if required.

The information that switches trigger types is produced by Programmable Lookup Units (PLU). The different trigger types are defined and loaded into PLUs. HERMES relies on those to distinguish between two types of trigger. “Physical” triggers are tied to the HERA-clock. The non-physical triggers are arbitrary in time. The main physical trigger 21 corresponds to a hit in all of the hodoscopes and a calorimeter hit above a certain threshold.

A dedicated trigger has been proposed for the pentaquark search. In the HERMES experiment, a channel pK_S^0 is analyzed where the K_S^0 is decays into two oppositely charged pions. For full reconstruction of such events, three hadron tracks have to be detected. The “pentaquark trigger” requires two tracks in the upper half of the detector and one in the bottom half, or vice versa. A single hadron track is defined by a one hit in H0, H1 and H2 and additionally a hit in the back chambers. The “pentaquark trigger” has been in use since 2004.

The HERMES data acquisition system is based on a Fast-Bus backbone. The Fast-Bus TDCs (Time-to-Digital Converter) and ADCs (Analog-to-Digital Converter) perform the readout. The drift chambers are read out by TDCs. The magnet chambers are read out by a PCOS IV system that is restricted to a single bit per channel.

The data acquisition stream is separated into runs. Each run consists of a dataset of events. During a fill of the positron machine, the data is written onto hard discs in the online machine. Parallel to the data stream, slow control data is stored on the disc. Between the fills, the data is transferred to a tape robot on the DESY main site and a backup is written to local DLT tapes.

Chapter 4

Analysis of HERMES Data

An experiment searching for a new particle has to fulfill several conditions. It has to have sufficient momentum resolution in order to reconstruct the mass and width. In addition to the momentum resolution, particle identification (PID) and vertex reconstruction capability are needed. Such features can help to reduce background originating from different reactions. Finally, a sufficient acceptance in the explored kinematic region and decay channel is necessary. The ability of a spectrometer to detect certain particles can be studied by means of Monte Carlo (MC) simulations. The cross check of quality of MC is usually performed by the analysis of well established particles.

In the search for Pentaquark Θ^+ , two basic schemes were applied among experiments. Inclusive reconstruction schemes reconstruct the particle mass by the sum of 4-momenta vectors of the decay products and their squares. Only decay products are taken into account. The background is reduced by selecting events which have good PID and the track of each product can be considered as originating from a vertex common to all of the decay products.

Experiments claiming an exclusive measurement must detect all products. The final state can be reconstructed in the same way as in the inclusive scheme, where the accompanied particle is used as a tag for a certain production channel or a missing mass technique is applied. This technique is useful for situations where one of the sought-for particle's decay product is neutral and thus a momentum measurement is difficult. The 4-momentum in the input channel is known as well as the 4-momenta of particles accompanying the investigated decay channel. Using the 4-momentum conservation law, an unknown 4-momentum can be computed and its scalar square root which represents the

invariant mass of the decay channel of interest can thus be established.

4.1 HERMES Data Selection

The analysis henceforth described was performed using the inclusive method defined in the previous section of this chapter. The predicted decay channel [25] of the Θ^+ into KN was investigated in HERMES data. Since clean PID is needed for all the decay products, the only data selected is that which has been measured with the RICH. This data was collected in the years 1998, 1999 and 2000 and has an integrated luminosity of $L = \int \mathcal{L} dt = 295.7 \text{ pb}^{-1}$. Only data on deuterium targets, both polarized and unpolarized, has been used for this analysis.

The first step was to select events which contain three or more hadron tracks in the fiducial volume of the spectrometer. The tracks must be long tracks, because only these allow PID by means of the RICH. The track is defined as a long track when track parts are reconstructed in both sets of tracking chambers, FC and BC. The hadrons have been selected according to PID values in the μ DSTs table:

$$g1Track.rPID3 + g1Track.rPID5 < 0 \quad (4.1)$$

As the next criteria, charge information and RICH particle type information have been used to find events. Two tracks have to be identified as oppositely charged pions and one track as a proton. This corresponds to type values obtained by RICH:

$$smRICH.iType = 3 (\pi^+, \pi^-) \quad (4.2)$$

$$smRICH.iType = 5 (p) \quad (4.3)$$

Since the reliability of the RICH PID differs for certain momenta regions and particle types, limits have been introduced for pion momenta.

$$1 \text{ GeV} < P_\pi < 15 \text{ GeV} \quad (4.4)$$

and for proton momenta

$$4 \text{ GeV} < P_p < 9 \text{ GeV} \quad (4.5)$$

The RICH PID quality parameter has been set to

$$smRICH.rQp > 0 \quad (4.6)$$

for pions and to

$$smRICH.rQp > 1.5 \quad (4.7)$$

for protons.

The next step in the analysis was to reconstruct K_S from the selected event sample. The four-momenta of two pion tracks was added and the invariant mass of both calculated. The invariant mass spectrum of the $\pi^+\pi^-$ is shown in Fig. 4.1. The resulting spectrum

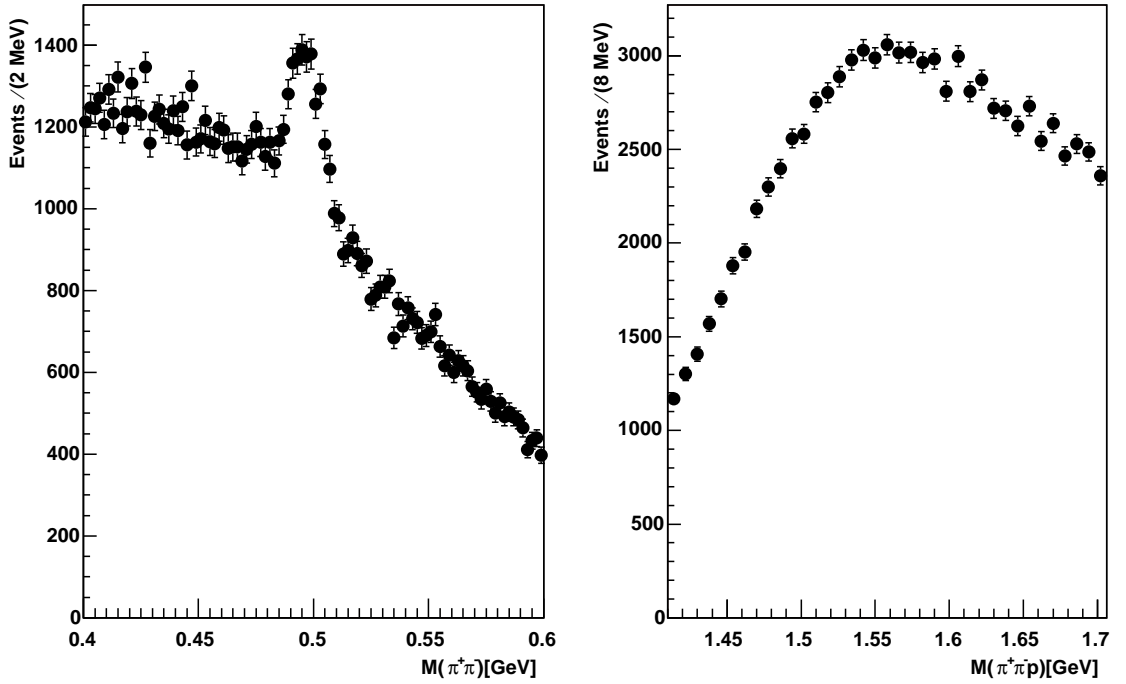


Figure 4.1: $\pi^+\pi^-$ invariant mass spectrum (left) and $\pi^+\pi^-p$ invariant mass spectrum (right). No cuts are applied on selected protons and pions. The $\pi^+\pi^-$ spectrum shows clear K_S peak while no structure is seen in the $\pi^+\pi^-p$ spectrum.

exhibits a clear K_S peak at 497 MeV, while the average value according to the PDG [79] is 497.272 ± 0.031 MeV. In order to improve the K_S signal-to-background ratio, additional cuts have been introduced. The cuts have been based on the event topology shown in Fig. 4.2. The position of the decay vertex B and the distance of the closest approach (DCA) of the pion tracks have been calculated. The tracks of particles which are produced by the decay of the same parent particle are supposed to come from the same vertex. This is, in the analysis, expressed for two pion tracks by the DCA cut:

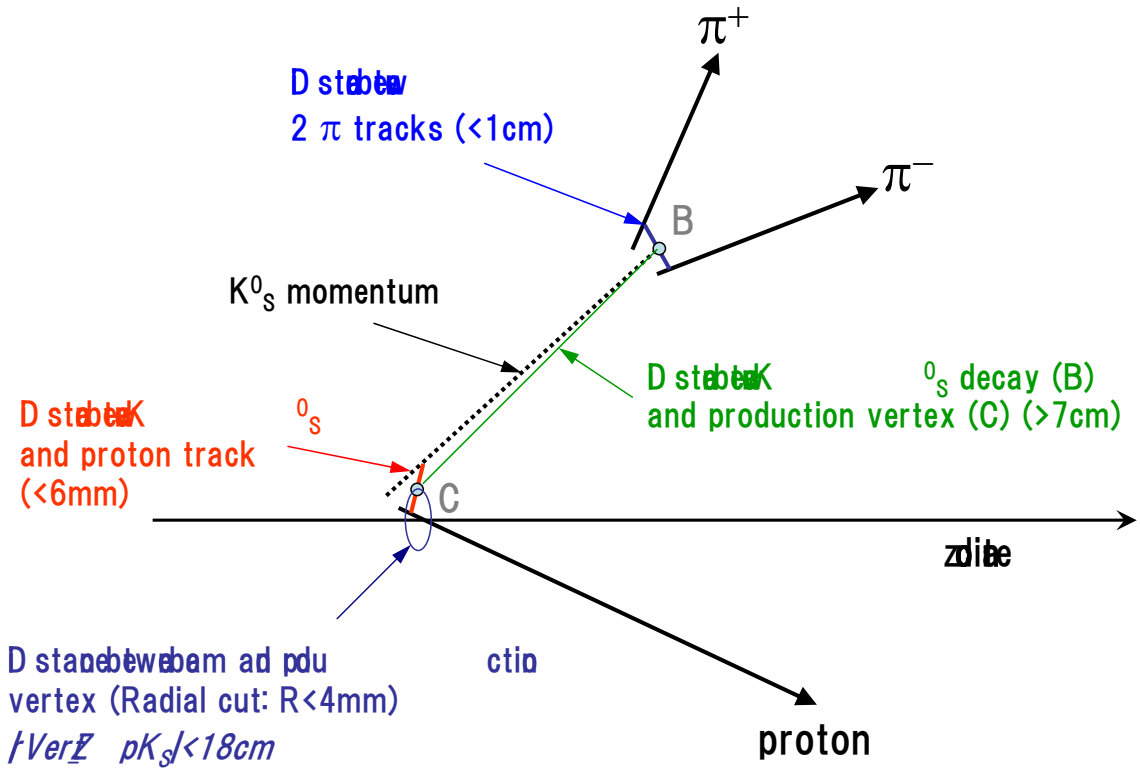


Figure 4.2: Topology of reconstructed three-track events

$$DCA_{\pi^+\pi^-} < 1 \text{ cm}. \quad (4.8)$$

The next topology cut utilizes knowledge of the mean life of the K_S (8.9 ns). For a K_S with a momentum of 1 GeV/c, the mean life corresponds to a flight distance of approximately 10 cm. In order to estimate decay length of potential K_S , its track and production vertex have been reconstructed. The direction of the K_S track is given by the sum of the two pions' three-momenta vectors. The K_S production vertex C has been reconstructed using the assumption that the K_S and the proton come from the same production vertex. The distance between two vertices gives a decay length of the K_S , which is required to be:

$$|B - C| > 7 \text{ cm} \quad (4.9)$$

Mass spectra of both the $\pi^+\pi^-$ and the $\pi^+\pi^-p$ systems are shown in Fig.4.3. The signal to background ratio of the K_S peak in $\pi^+\pi^-$ spectrum is improved whereas no significant structure is seen in the $\pi^+\pi^-p$ mass spectrum.

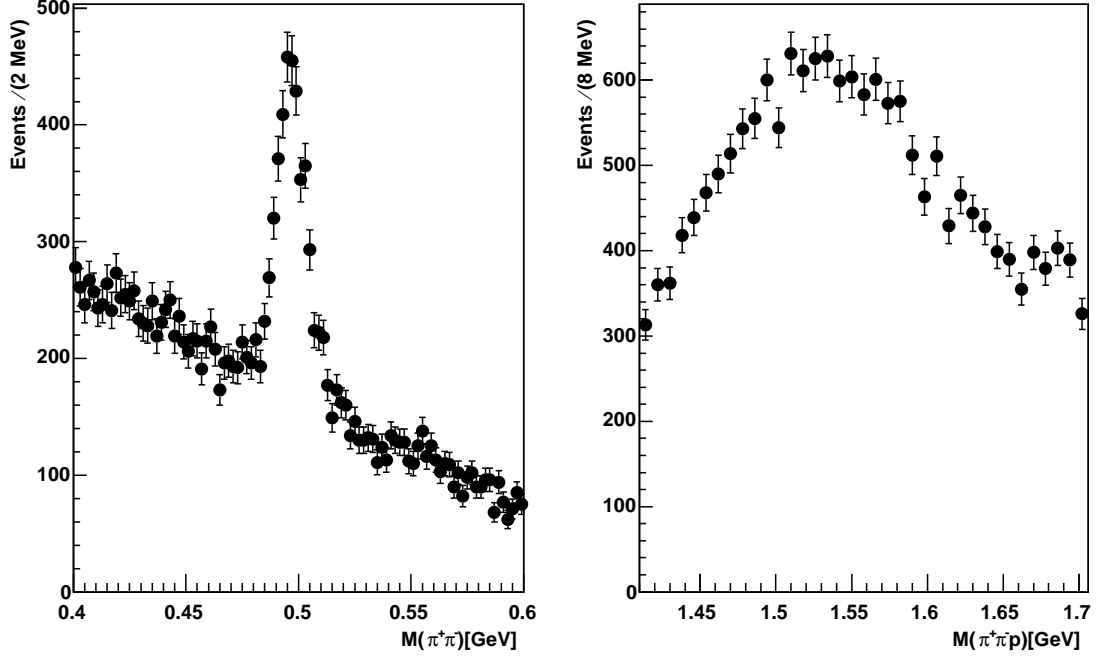


Figure 4.3: The $\pi^+\pi^-$ invariant mass spectrum left and the $\pi^+\pi^-p$ invariant mass spectrum right. The DCA and the decay length cuts are applied on selected pions in order to improve the K_S signal.

Up to now the shown $\pi^+\pi^-p$ invariant spectra has been constructed without constraints on the $\pi^+\pi^-$ mass. In order to satisfy the condition that the $\pi^+\pi^-$ coming from K_S decay, the events where the $\pi^+\pi^-$ invariant mass agree within 2σ of the mean value of the K_S peak have been selected.

$$|M_{\pi^+\pi^-} - 497| \text{ MeV} < 12 \text{ MeV}. \quad (4.10)$$

The region of selected K_S is depicted by the filled area in Fig. 4.4. Further, a causality cut has been applied for these plots - the position of the K_S decay vertex has to appear after the position of the K_S -proton production vertex with respect to the K_S momentum. Due to the HERMES acceptance limitations in the forward direction, this cut can be simply reduced to a cut on z -coordinates.

$$B_z - C_z > 0 \text{ cm}. \quad (4.11)$$

In Fig. 4.4 the $\pi^+\pi^-p$ spectrum is seen. More potential for the existence of a peak in the

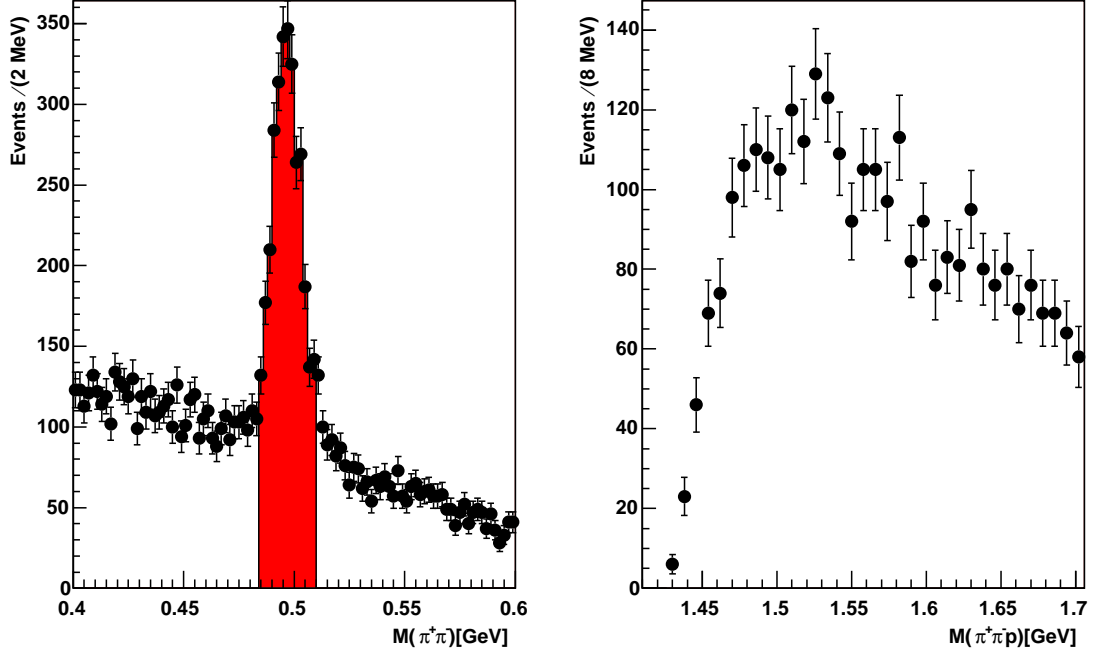


Figure 4.4: The $\pi^+\pi^-$ invariant mass spectrum left and the $\pi^+\pi^-p$ invariant mass spectrum right. The applied are extended by causality cut for position between $\pi^+\pi^-$ production and decay vertex. The $\pi^+\pi^-p$ spectrum is computed from events witch belong to the filled area of histogram in the left panel plot.

region of 1530 MeV can be seen.

The clarified K_S spectrum (i.e. the spectrum with the above mentioned cuts applied) can be seen in Fig. 4.5. The K_S peak has a mass of 496.7 MeV, which is in good agreement with the PDG [79] value 497.672 MeV. The width of 6.8 MeV is dominated by limitations in spectrometer resolution. Together with the K_S peak, a spectrum of the π^-p system is shown in Fig. 4.5. An enhancement in the region of 1116 MeV indicates that there is some small contamination caused by the $\Lambda(1116)$ hyperon. In order to suppress this contamination, events were rejected in which the invariant mass $M_{p\pi^-}$ fell within 2σ of the nominal Λ mass.

$$|M_{p\pi^-} - 1116| \text{ MeV} < 6 \text{ MeV} \quad (4.12)$$

The rejected events belonging to the histogram are indicated by the shaded region.

The last set of cuts is designed to select events with reasonable intersections of

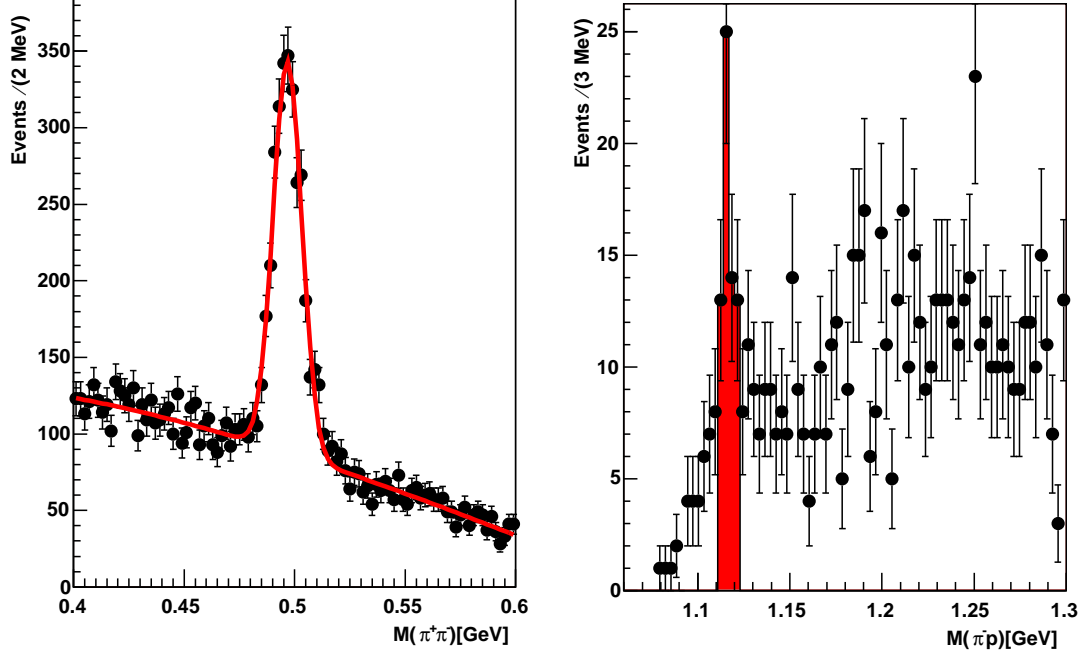


Figure 4.5: $\pi^+\pi^-$ invariant mass spectrum after applying the cuts is shown in the left panel. The spectrum is fitted with the sum of a polynomial of second order and a Gaussian. In the right panel, the π^-p invariant mass spectrum is shown.

proton and K_S tracks, which can be identified as possible Θ^+ production vertices.

Although a narrow width of Θ^+ is predicted in the case of strong decay, it can be assumed that the mean life is short enough that its decay vertex could be considered to be the same as the production vertex. The Θ^+ decay vertex is the same as the K_S production vertex. The distance between the K_S and the proton track at this point is required to be

$$DCA_{pK_S} < 0.6 \text{ mm}. \quad (4.13)$$

The Θ^+ is supposed to be produced in the beam interaction point, so cuts for the production vertex were introduced. The chosen cuts are:

$$|C_z| < 18 \text{ cm} \quad (4.14)$$

$$\sqrt{|C_x - \text{Beam}_x|^2 + |C_y - \text{Beam}_y|^2} < 4 \text{ mm}. \quad (4.15)$$

The final spectra of the pK_S system, published in [18], are displayed in Fig. 4.6. The fit curve in both plots is obtained using the unbinned fit package RooFit [80]. The

unbinned fitting method has been used in order to eliminate any influence of binning effects, which can be large in the case of statistically small samples. The fit curve in the left plot in Fig. 4.6 is composed from a third order polynomial and a Gaussian. The position of the Gauss peak is 1528 MeV with a width of 8 MeV.

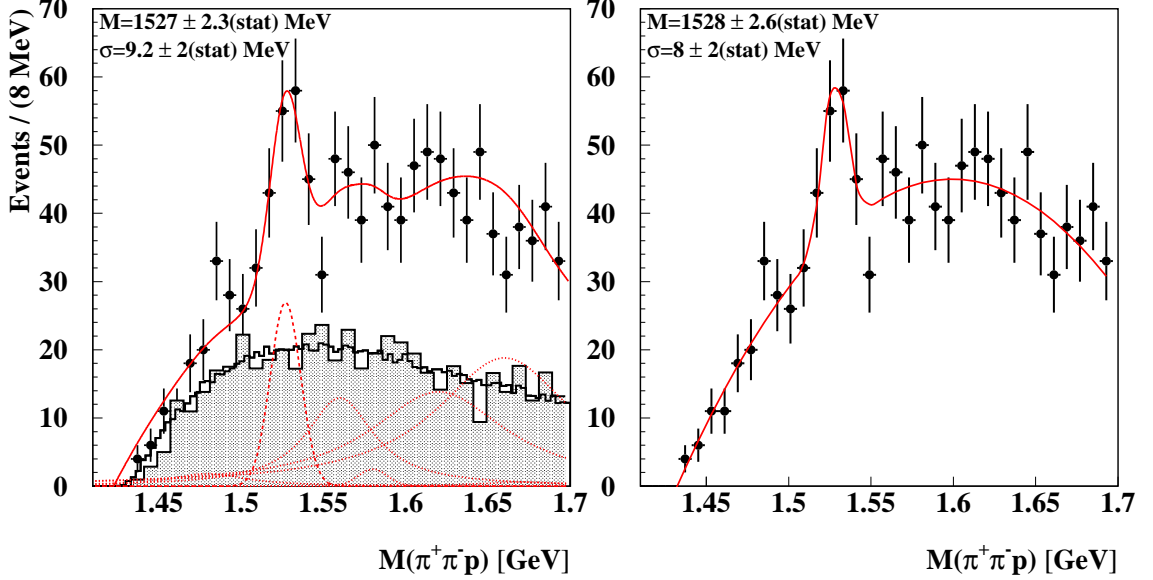


Figure 4.6: The final invariant mass spectrum of the pK_S obtained by the HERMES experiment. The right plot shows the spectrum fitted by third order polynomial plus Gaussian. In the left picture are six Σ^* resonances fitted additionally to the background. The gray shaded histogram represents a normalized PYTHIA6 simulation and the solid line histogram is the normalized result of a mixed event analysis.

In order to understand background, different methods have been applied to its calculation. The first method is based on a mixed event analysis. The K_S tracks are combined with the proton track from different events and the invariant mass spectrum is computed. The results of the mixed event analysis is shown in the left box of the Fig. 4.6 as the solid line histogram. As the second approach to calculate background a PYTHIA6 simulation [81] has been used tuned for HERMES kinematics [82]. The normalized result of this simulation is represented by the gray shaded histogram. The shape of the non-resonant background spectrum agrees very well with the shape obtained by means of the mixed event analysis, but there is a discrepancy between the simulated and measured backgrounds: there are more events in the measured background than in the simulated background. The missing events can be explained by the introduction of Σ^* resonances,

which can decay into pK_S and which are not included in the PYTHIA6 event generator. In order to confirm this possible explanation, the following fit procedure has been used. The fit function for the measured invariant mass of the pK_S system has been constructed as a sum of polynomial function, six convoluted functions of the Breit-Wigner function with Gaussian and one Gaussian function. The polynomial parameters have been obtained from a fit of the simulated background and have been fixed. The widths and positions of six Breit-Wigner functions have been fixed to the PDG [79] values of the Σ^* . The following six Σ^{*+} were included: $M = 1480$ MeV with $\Gamma = 55$ MeV, $M = 1560$ MeV with $\Gamma = 47$ MeV, $M = 1580$ MeV with $\Gamma = 13$ MeV, $M = 1620$ MeV with $\Gamma = 100$ MeV, $M = 1660$ MeV with $\Gamma = 100$ MeV and $M = 1670$ MeV with $\Gamma = 60$ MeV. The amplitudes of these have been used as free parameters of the fit. However, an extra, unknown resonance must be included in addition to the six Σ^* , in order to describe shape of the spectrum. The Gauss function fits the nominal role of a hitherto unknown resonance. As can be seen from the left box of Fig. 4.6, such a constructed function can very well describe the shape of the spectrum. The resonance represented by the Gaussian could be an indication of a new narrow state decaying into pK_S . The fit results to a mass of 1527 MeV with the FWHM 22 MeV for this new state.

The amount of statistics of observed events with a pK_S system in the final state is rather poor, although the data over three years has been used for analysis. Due to low statistics, the significance of the observed peak could be a subject of discussion. Two approaches have been used in order to estimate the significance. The first expression is the naïve estimator $N_s^{2\sigma}/\sqrt{N_s^{2\sigma}}$. The corresponding result is listed in Table 4.1. The second, more precise approach is using the ratio $N_s/\delta N_s$, where all correlated uncertainties from the fit are accounted for in δN_s .

4.2 The Θ^- State

The standard model shows that every particle has an antiparticle, for which each additive quantum number has the negative of the value it has for the “normal” matter particle. If we assume the condition that our measured peak is real and that Θ^+ pentaquark exists, then the charge conjugate anti-particle $\bar{\Theta}^-$ has to exist as well. An analysis was performed with the goal of finding such an antiparticle. The same data sample was analyzed as for Θ^+ . The set of cuts was practically the same except for the following changes: For

	Θ^+ mass [MeV]	FWHM [MeV]	$N_s^{2\sigma}$ in $\pm 2\sigma$	$N_b^{2\sigma}$ in $\pm 2\sigma$	naïve signif.	Total $N_s \pm \delta N_s$	sgnif.
Ia)	$1527.0 \pm 2.3 \pm 2.1$	$22 \pm 5 \pm 2$	74	145	6.1σ	78 ± 18	4.3σ
IIa)	$1527.0 \pm 2.5 \pm 2.1$	$24 \pm 5 \pm 2$	79	158	6.3σ	83 ± 20	4.2σ
Ib)	$1528.0 \pm 2.6 \pm 2.1$	$19 \pm 5 \pm 2$	56	144	4.7σ	59 ± 16	3.7σ
IIb)	$1527.8 \pm 3.0 \pm 2.1$	$20 \pm 5 \pm 2$	52	155	4.2σ	54 ± 16	3.4σ

Table 4.1: Mass and width values obtained by different fit procedures of the pK_s system and their systematic and statistical errors. Row Ia) is based on the fit using the simulated background model and Σ^* s. In the case of row Ib), background is fitted simply by a polynomial. Rows IIa) and IIb) are using same background models as Ia) and Ib) respectively, but different mass reconstruction expressions that are expected to result in better resolution. Number of signal and background events in 2σ area are in column marked as $N_s^{2\sigma}$ and $N_b^{2\sigma}$.

the hadron identified as a proton previously by means of the RICH, the charge had to be negative. Since the antiproton could not come from a Λ decay with π^- but can originate from the decay of the $\bar{\Lambda}$ to $\bar{p}\pi^+$, the cut in equation (4.12) was changed to

$$|M_{\bar{p}\pi^+} - 1116| \text{ MeV} < 6 \text{ MeV} \quad (4.16)$$

The resultant spectrum is shown in Fig. 4.7. The statistics obtained were about a factor of five smaller than in the case of the Θ^+ spectrum and therefore it is not possible to judge the existence or non existence of Θ^- state.

Non-observation of the peak in $\bar{p}K_s$ could be consistent with existence of Θ^+ . As will be shown later in the analysis of $\Lambda(1520)$ in section 4.6, the production of antibaryons is suppressed. The suppression is due to limited reaction phase space for antiparticle production. In order to obey baryon conservation law, a new baryon has to be produced together with its antibaryon, while baryonic states can be produced from the nucleon target by additional reaction channels. The suppression factor between baryon and antibaryon with similar masses like Θ^+ is about factor 14, assuming that the suppression factor is the same for $\Lambda(1520)$ and Θ^+ . Using the number of observed Θ^+ and this suppression factor, we obtain that the expected number of Θ^- is 4 or 5, depending on the method used for the fit of the pK_s mass spectrum.

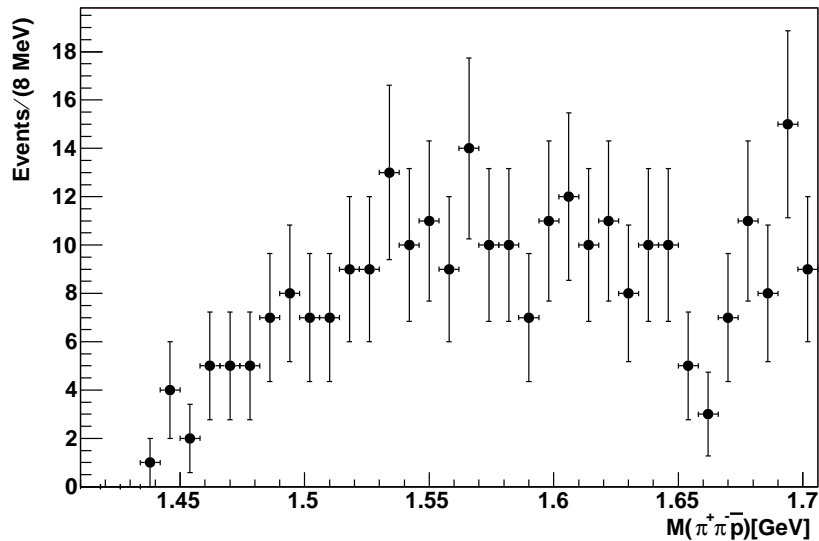


Figure 4.7: The invariant mass distribution of the $\bar{p}K_S$ system. The statistics are too small for any statement about existence of Θ^- state,.

4.3 Four Track Events Analysis

In the work [83], a possible production mechanism of the Θ^+ in the HERMES experiment has been discussed. With a deuterium target, the most likely reactions are considered to be

$$\gamma^* p \rightarrow \bar{K}^0 \Theta^+, \quad (4.17)$$

or

$$\gamma^* n \rightarrow K^- \Theta^+. \quad (4.18)$$

Unfortunately, there is no direct access to confirm these hypotheses because of the HERMES acceptance. Due to the small opening angle of the HERMES spectrometer, the detection of all four particles is unlikely. In the first analysis we required three tracks, which had to be oppositely charged pions and a proton. The number of statistics obtained was rather low. If we required an additional fourth track, the statistics would drop even more. A particle-type plot for the fourth track detected together with $K_S p$ events, after applying all analysis cuts, is shown in Fig. 4.8. It is clearly seen that we can not fully reconstruct all particles from the considered reaction channels due to the small number of K which are detected as a fourth track. On the other hand we can use the fourth track to reduce background. There are other channels where from K_S could originate. The main contribution to the K_S

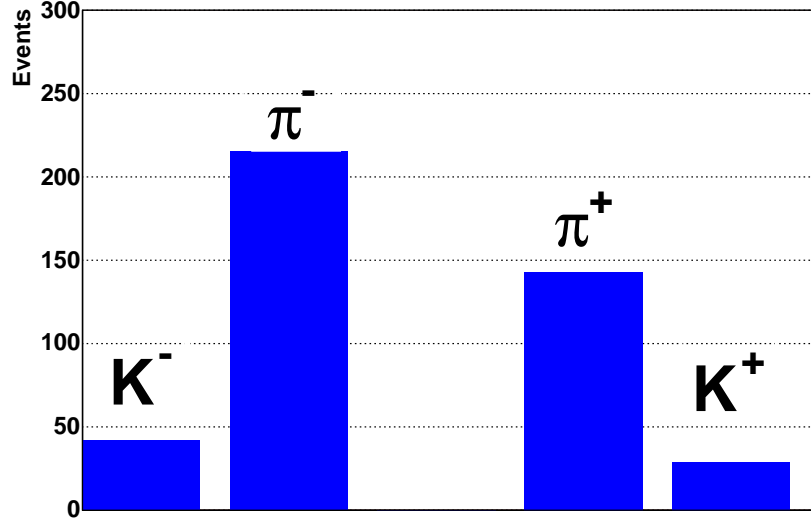


Figure 4.8: The distribution of particle type of the fourth track.

statistics could be from

$$\phi \rightarrow K_L K_S \quad (4.19)$$

and

$$K^{*\pm} \rightarrow \pi^\pm K_S \quad (4.20)$$

We could not reject events originating from ϕ because it would be necessary to reconstruct K_L but in a principle is possible reduction of background from K^* . The plot of invariant mass of the system of the K_S and π^\pm is shown in Fig. 4.9. The statistics are low but the region around 892 MeV (which is mass of the K^*) is covered. In the next step, the following cut was applied in order to construct a new invariant mass spectrum of the $K_S p$ system in which the fourth particle has to be detected, identified as a pion and in which the invariant mass of the $K_S \pi$ system can not be interpretable as K^* :

$$|M_{K_S \pi} - 0.892| > 0.075 \text{ GeV}. \quad (4.21)$$

Furthermore, the pion from the fourth track could be a decay product of a Λ . Therefore, the invariant mass of negatively charged pions and protons has been calculated and cuts (4.12) applied again. The resulting spectrum of the $K_S p$ system invariant mass shows a clear peak at a mass of 1530 MeV (see Fig. 4.10). The signal to background ratio is improved, but total statistics are significantly lower. The estimate of the significance of the peak is 3.5σ in the naïve approach and 2.99σ in the realistic.

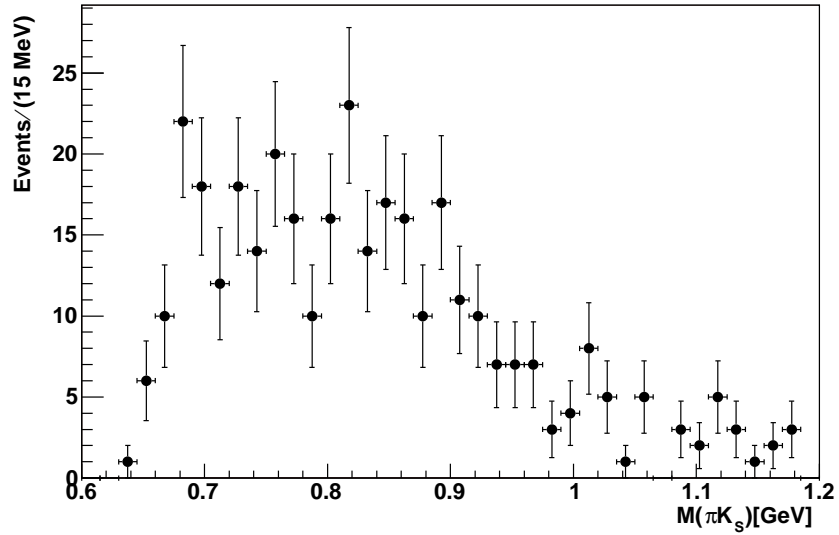


Figure 4.9: Invariant mass spectrum of the system $K_S\pi$. The spectrum is generated from events where three tracks of standard Θ^+ cuts are accompanied by fourth track which is identified as pion.

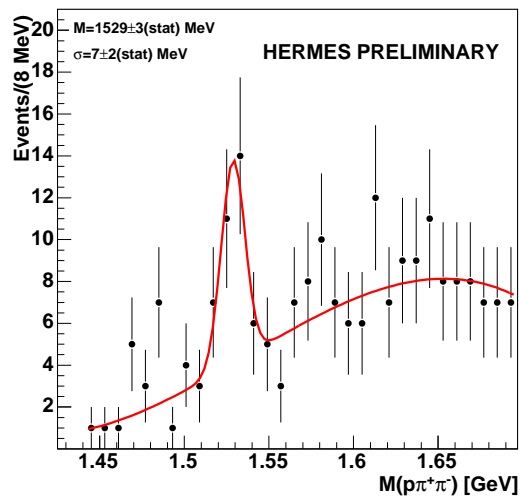


Figure 4.10: The invariant mass spectrum of $K_S p$ system. Two opposite charged pions and protons are accompanied with the fourth track identified as pion. The events, where pion have together with K_S invariant mass of K^* or with p mass of the Λ , are excluded.

4.4 Monte Carlo

Knowledge of the spectrometer acceptance is crucial to ensure that any measured mass and width is correct and that a peak is not produced artificially. In order to understand the acceptance for a three-track decaying particle, a simple Monte-Carlo generator has been developed. The generator is described in [84]. By means of this generator, a particle with certain mass and width can be produced and made to decay into 2 or 3-body system. The decay products can be specified to be any particle types known to GEANT [85]. The momentum distribution of the parent particle is represented as a part of a Gaussian distribution. The expected value of the Gaussian can be negative or larger than beam momentum in order to obtain monotonic distribution. The vertices of generated particles are distributed according to the usual gas profile. In the work [84], the mass of the parent particle has been chosen to be 1540 MeV and width $\Gamma = 2$ MeV, accordingly to the measured masses and widths in experiments which observed the Θ^+ . The particle decays into a K_S and proton system. The reconstruction of the simulated resonance uses the same sets of cuts as the analysis of the measured data. The reconstructed peak exhibits a width $\sigma = 7.2$ MeV, which shows that the width of the observed peak is generated mainly by the spectrometer resolution.

By means of the ratio of generated and reconstructed events, the spectrometer acceptance has been estimated. The combined acceptance and cut efficiency has been found to be $\epsilon = 0.14\%$. It has been found that this acceptance is fairly insensitive to the choice of parameters controlling the generated transverse momentum of the Θ^+ . Using this acceptance, a rough estimate about the production cross section of a pentaquark in the photo-production reaction can be provided according following formula.

$$\sigma_{\gamma N \rightarrow \Theta^+} = \frac{N_{\text{observed}}^{\Theta^+ \rightarrow pK_S}}{\Phi \cdot \mathfrak{B}\tau \cdot L \cdot \epsilon} \quad (4.22)$$

where the integrated luminosity L of the analyzed data sample corresponds to 295.7 pb^{-1} [86]. Using the assumption that the branching ratios of $\Theta^+ \rightarrow p\bar{K}^0$ and $\bar{K}^0 \rightarrow K_S^0$ both are $1/2$ gives that $\mathfrak{B}\tau = 1/4$. Applying the Weizsäcker-Williams approximation [87, 88], the virtual photon flux is $\Phi = 0.02$. There are $N_{\text{observed}}^{\Theta^+ \rightarrow pK_S} = 74$ events, which results in a cross section of $\sigma = 36 \text{ nb}$. The estimated cross section is a very rough number, because the Monte Carlo does not include trigger efficiency and the angular distribution of the decaying particle. Both these numbers are unknown, but important for a more exact cross section

estimation.

4.5 Width and Angular Distribution of the Θ^+

The knowledge about angular distribution of the Θ^+ decay can supply information about the possible spin of the particle. In [89], possible options for pentaquark decay have been discussed. A model-independent assumption predicts the isotropic angular distribution decay in the center-of-mass system of the pentaquark for spin $\frac{1}{2}$. This is valid since the production process is a strong interaction which conserves parity. The produced pentaquark could not have longitudinal polarization. The polarization in the beam direction must vanish as well. In the decay, the total angular momentum is conserved. Thus the decay has to be isotropic in the center-of-mass system of the pentaquark. These constraints are not necessarily valid for the background and for other possible pentaquark spin.

Predicted spins for the Θ^+ state differ between the models. If the measured decay of the Θ^+ differs from isotropic, spin $\frac{1}{2}$ can be excluded. In order to measure the angular distribution of the Θ^+ we have to know an acceptance for the particular angles in their center-of-mass system. These were estimated by means of the results of the Monte Carlo simulation, where an isotropic decay behavior of the Θ^+ was simulated.

The same generator as for the mass resolution study was used for studies of the decay distribution. Although the HERMES observed mass is 1528 MeV, the average observed mass across all experiments that reported observance is closer to 1530 MeV (see Tab. 2.2), the mass of the parent particle has been set to 1530 MeV. The observed width of the peak is a little larger than the simulated one, so the Γ of the parent particle has been taken to be 10 MeV. The parameters of the momenta distribution were: the momenta spread in transversal direction $\sigma_{P_{\perp}} = 0.4 \text{ GeV}$, the mean of the momenta in the z -direction $\langle P \rangle_z = -0.143 P_{beam}$ and the momenta spread in the z -direction $\sigma_{P_z} = 0.237 P_{beam}$. The invariant mass spectrum of reconstructed $K_S p$ system is shown in Fig. 4.11. The peak in this spectrum exhibits a larger width ($\sigma = 10.6 \text{ MeV}$). The width of the parent particle has been increased by factor of 5 - nevertheless the reconstructed width increased by about 50 %. This confirms hypothesis that the real width of the peak is small and the width of the observed one is mainly due to the spectrometer resolution. From each reconstructed event, a decay angle in the center-of-mass system has been calculated. The direction of the x -axis in the c.m.s. (center-of-mass) system has been given by means of the direction of

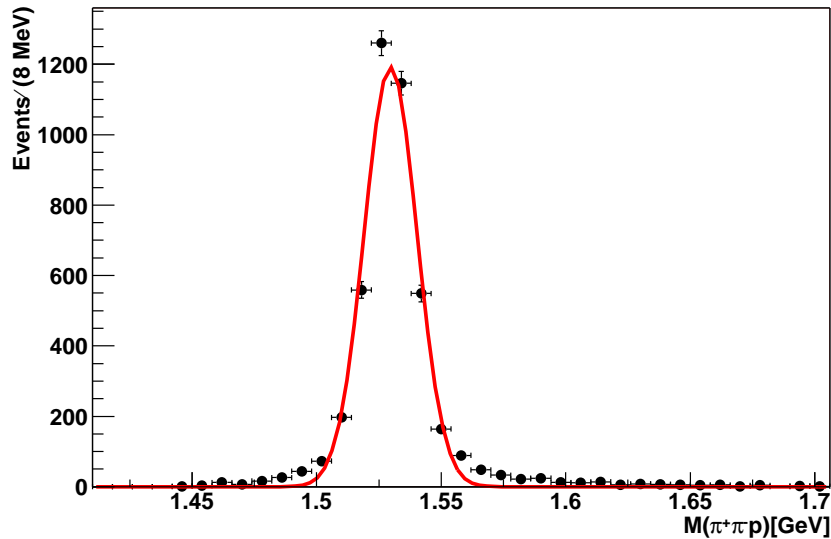


Figure 4.11: The invariant mass distribution of simulated Θ^+ .

the pK_S system momentum in the laboratory frame. The simulated angular distribution accepted by the spectrometer compared to the measured one is shown in Fig. 4.12. The measured distribution is shown in Fig. 4.13. In the plot the normalized distribution for events from a two σ interval around the observed peak is compared with the distribution of the background events. A slight difference is seen between the signal and the background angular distribution. The mean value of the background cosine angle is 0.40 (0.33 RMS), while the mean cosine of the signal is 0.44. The simulated distribution differs as well only slightly from the measurement of the background. The mean value of the simulated distribution is about 0.35 and the RMS is 0.325. Since the simulation starts from an isotropic angular distribution, one can conclude that both the background and the signal exhibit slight forward peaking. In the case of the signal, the forward peaking seems to be more significant than in the background case.

Such a result might lead to the conclusion that the spin of the Θ^+ is not $\frac{1}{2}$ according to Ref. [89]. On the other hand, it has to be stressed that the number of events which have been used for the construction of the angular distribution is 221. Further, the analysis [18] results show that the signal to background ratio is about 1:2. This means that the shape of the measured angular distribution is given mainly by the background, and the signal

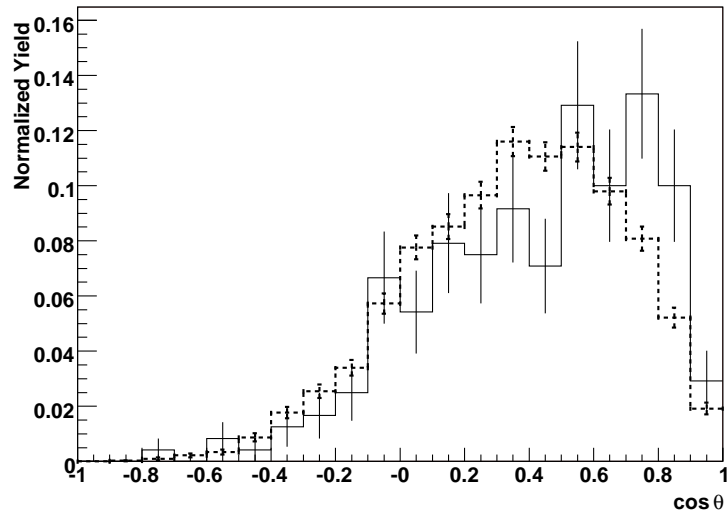


Figure 4.12: The comparison of the simulated and measured angular distribution of the Θ^+ . In the simulation, the parent particle decays isotropically in the center-of-mass system. Angular distribution of simulated Θ^+ accepted by the HERMES spectrometer is displayed by the dashed line. The angular distribution corresponding to the events whose mass agree within 2σ to the mean of the observed peak are depicted by solid line.

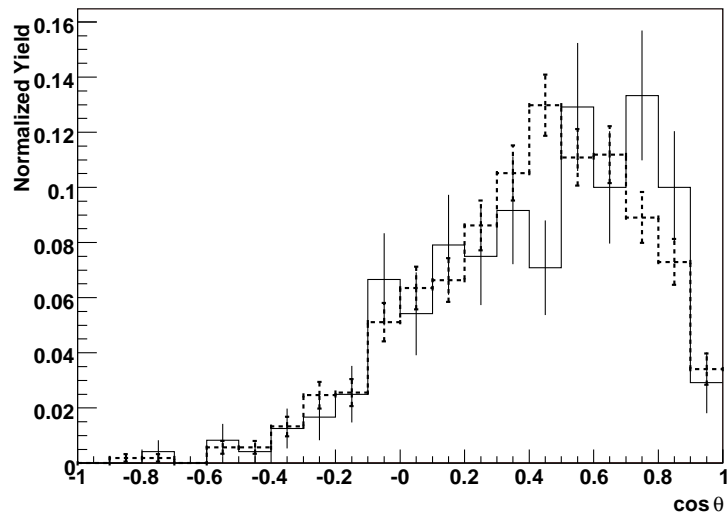


Figure 4.13: The measured angular distributions of the pK_S system. The solid line is given by the events whose mass corresponds to the mass of the observed peak. The dashed line corresponds to background events out of the two σ -range around a peak. .

part is suppressed. With low statistics and only the slight deviation between the measured and the simulated angular distributions, a statistical fluctuation can not be excluded as the explanation for the observed difference from the isotropic angular distribution.

4.6 Karliner - Lipkin Scheme

In the work [90] Karliner and Lipkin proposed a new test which can help to make a decision about the origin of an observed peak. The test is based on information obtained from squared momentum difference between the momenta of two experimentally-observed particles in the laboratory frame. The angular distribution of the relative momenta in the center-of-mass system exhibits a forward-backward symmetry in the production and decay of any resonance with a definite parity. Let P_K denote a 3-momentum of a Kaon and P_N the momentum of the nucleon. The squared momentum difference is defined as $\Delta P_{KN}^2 = |P_K|^2 - |P_N|^2$. The distribution of the counting rates observed at certain momenta has to be symmetric and obey the equation

$$N(\Delta P_{KN}^2 = \Delta \bar{P}_{KN}^2 + \delta P_{KN}^2) = N(\Delta P_{KN}^2 = \Delta \bar{P}_{KN}^2 - \delta P_{KN}^2) \quad (4.23)$$

where the mean value of the squared momentum difference is given by

$$\Delta \bar{P}_{KN}^2 = \langle |P_K|^2 - |P_N|^2 \rangle = \frac{M_K^2 - M_N^2}{M^2} \cdot |P|^2 \quad (4.24)$$

where M_K , M_N and M are Kaon, nucleon and resonance masses and P is the sum of the nucleon and Kaon momenta.

The momentum difference $|P_K|^2 - |P_N|^2$ distribution from measured data can help to identify of the origin of the observed peak. A peak created by the kinematic reflection will generally not have forward-backward symmetry nor satisfy equation (4.23). Furthermore the method can be used to improve the signal-to-background ratio by cutting out events which are mainly background. This can work in any case where there is a significant difference between the angular distribution of signal and background and this difference remains significant even for events within detector acceptance.

4.6.1 $\Lambda(1520)$ and $\bar{\Lambda}(1520)$

The proposed Karliner-Lipkin scheme is suitable mainly for experiments with 4π acceptance and is claimed to be generally valid for any resonance. In this section it is

described as a test which has been performed in order to estimate whether this method can be used even for the HERMES spectrometer whose acceptance is restricted in the forward direction. In order to avoid an artificially produced peak in a pK_S spectrum by means of a kinematical cut, the method has been applied on a well known resonance. The most feasible candidate for the test was found to be $\Lambda(1520)$. The $\Lambda(1520)$ has almost the same mass as observed for the Θ^+ and decays into the pK^- system, where the similar masses of the products produce similar kinematic constraints on the primary particles in the decay. The difference of the acceptance is given by detection of Kaons. While K_S is reconstructed from its secondary products $\pi^+\pi^-$, the K^- is detected directly.

Before starting the analysis of momenta square differences, the pK^- system was reconstructed. In order to obtain comparable results to the Θ^+ analysis, a similar set of cuts was used. The K^- and proton have been selected in the momentum range

$$3 \text{ GeV} < P < 15 \text{ GeV} \quad (4.25)$$

for K^- and

$$4 \text{ GeV} < P < 9 \text{ GeV}. \quad (4.26)$$

for proton momenta. The PID quality cuts were

$$smRICH.rQp > 0 \quad (4.27)$$

for Kaons and

$$smRICH.rQp > 1.5 \quad (4.28)$$

for protons. All tracks had to be long tracks and the set of fiducial cuts for any particular track remains the same as in the case of the Θ^+ reconstruction. The decay vertex of the pK^- was computed and the distance of closest approach (DCA) cut has been taken as:

$$DCA_{p+K^-} < 0.6 \text{ cm}. \quad (4.29)$$

It is supposed that the $\Lambda(1520)$ decays directly in the production point. The same cut on the position of the production vertex was used as was in the case of the Θ^+ :

$$|C_z| < 18 \text{ cm} \quad (4.30)$$

$$\sqrt{|C_x - Beam_x|^2 + |C_y - Beam_y|^2} < 4 \quad (4.31)$$

The resulting spectrum of the pK^- system up to mass 1.7 GeV is shown in Fig. 4.14. The distribution was fitted by means of the sum of a Breit-Wigner function and a third order polynomial. The unbinned fit method has been used. The fit results show a mass of 1524 MeV and $\Gamma = 27$ MeV. Considering the spectrometer resolution, both values are in

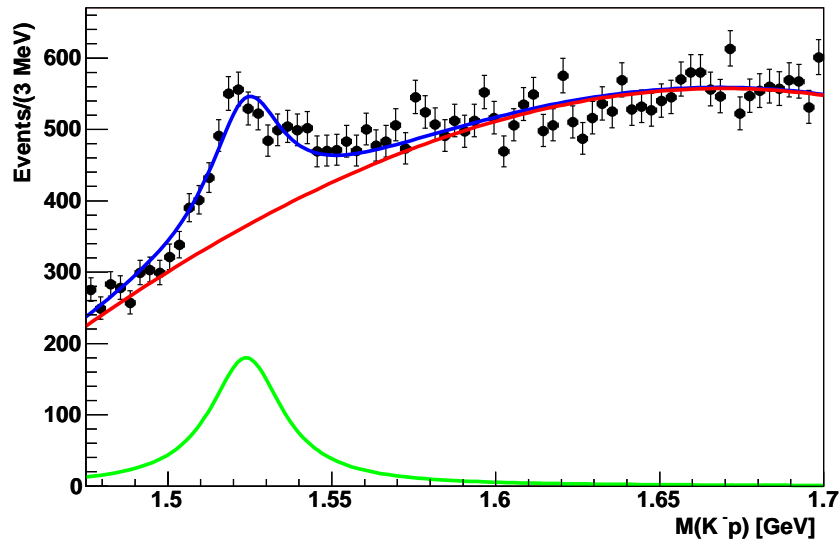


Figure 4.14: The invariant mass spectrum of the pK^- system. .

agreement with the PDG [79] values.

The same analysis has been performed for oppositely charged tracks, where the proton has been replaced by an antiproton and K^- by K^+ . In the $\bar{p}K^+$ mass spectrum, the peak of the conjugate $\bar{\Lambda}(1520)$ is expected. The spectrum was fitted by the same function as pK^- - this is shown in Fig. 4.15. Because there is no evidence for any peak structure around the mass of 1520 MeV, the position and the width parameters of Breit-Wigner function has been fixed to the values obtained from the fit of the pK^- spectrum. In this way, a lower limit for $\bar{\Lambda}(1520)$ production suppression factor with respect to $\Lambda(1520)$ production can be estimated. Considering the same acceptance of the spectrometer for both final states, the cross section ratio between production particle and antiparticle is $\frac{\sigma_{\Lambda(1520)}}{\sigma_{\bar{\Lambda}(1520)}} > 13.6$

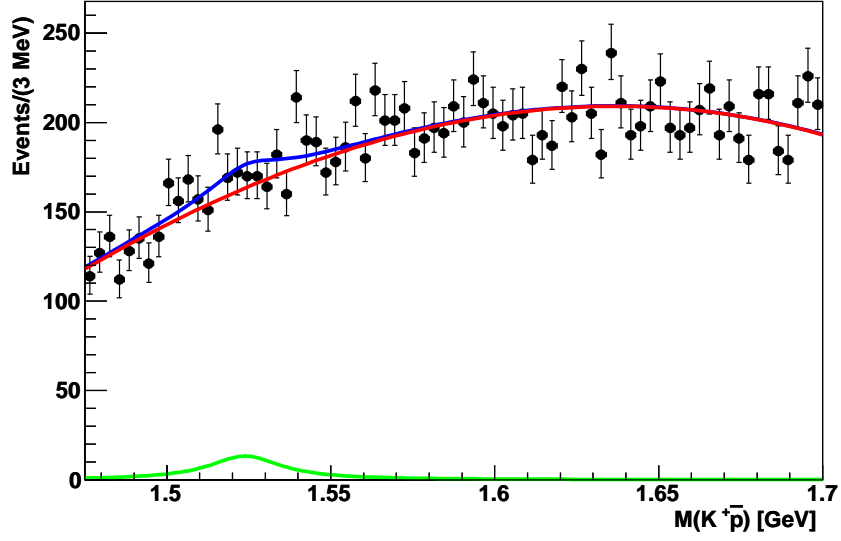


Figure 4.15: The invariant mass spectrum of the $\bar{p}K^+$ system.

4.6.2 Application of K.-L. Scheme

The reconstruction of the $\Lambda(1520)$ by means of the pK^- system has been shown in the previous subsection. Now the pK^- data can be used for a test of the K.-L. scheme. The squared momentum difference $|P_K|^2 - |P_N|^2$ has been computed separately for the events which belong within 2σ of the peak and the events which belong to the background. The distribution of both is shown in Fig. 4.16. The distribution of the signal exhibits different behavior from the background for higher values. A significant difference between signal and background events is required for this method to work. From the plots it can be seen that the shape of the distributions differ for positive values. This means that there is a difference between signal and background, which indicates that in the case of the $\Lambda(1520)$ this method can be, in principal, used for the improving signal to background ratio. About 15% of the background events have positive values of square momentum difference, whereas among signal events there are only 10% events with positive values.

This result shows that the suggested scheme can be applicable for $\Lambda(1520)$. The scheme should be performed by applying a cut on positive values of square momentum difference. In order to find the best value, a scan of possible cuts from $-60 \text{ GeV}^2/c^2$ to

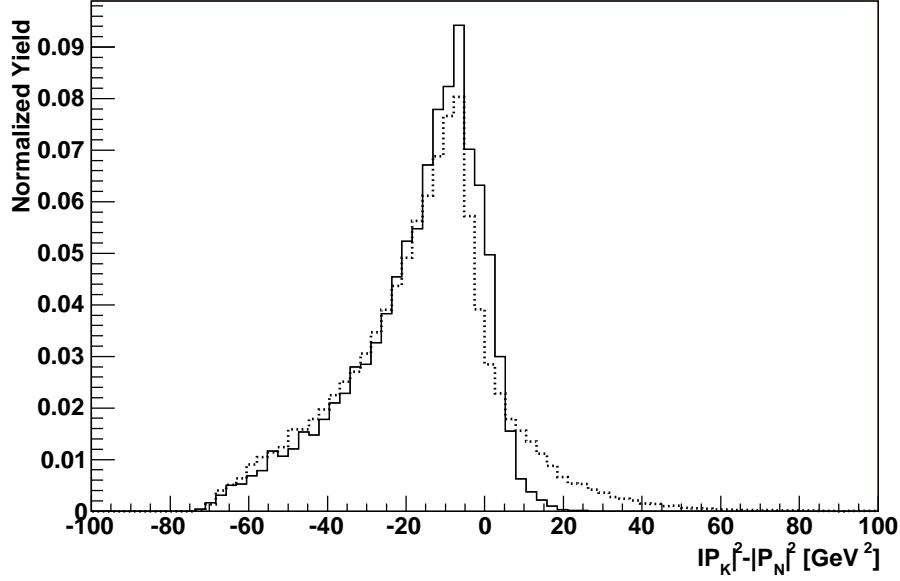


Figure 4.16: The squared momentum difference $|P_K|^2 - |P_N|^2$ plot. Solid line shows distribution of the signal events, whereas dotted line shows distribution of the background.

100 GeV^2/c^2 has been performed. Each reconstructed spectrum of pK^+ has been fitted by above mentioned function. Both, naïve ($N_s^{2\sigma}/\sqrt{N_s^{2\sigma}}$) and realistic ($N_s/\delta N_S$) significance has been computed for each cut. The peak significance dependence on the cut values is plotted in Fig. 4.17.

There an improvement of the significance for cut about value $|P_K|^2 - |P_N|^2 = 5 \text{ GeV}^2/c^2$ can be seen. Both significances increase - the naïve one by about 3σ , the realistic about 1σ . The increase of the significance is correlated with a slight increase in both peak mass and peak width. The drop of the significance in the negative square momentum difference region is due to a strong decrease in the number of events in the final spectrum.

After applying the cut $|P_K|^2 - |P_N|^2 < 5 \text{ GeV}^2/c^2$ on the data where the pK_S system is detected, the significance of the Θ^+ peak improved to 6.6σ for the naïve approach and to 4.5σ for the realistic. The spectrum, including the fit curves, is shown in Fig. 4.18.

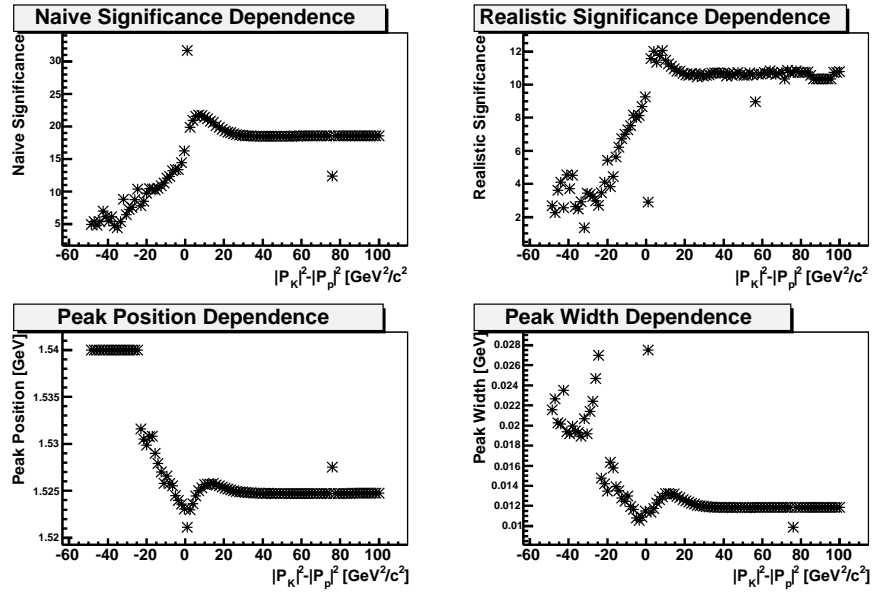


Figure 4.17: The scan of square momenta cut values for K.-L. scheme. The events below certain square momenta difference are selected and the final spectrum is fitted. In upper panels the dependence of naive and realistic significance is showed. The dependence of peak position and width on the cut value is shown in lower panels.

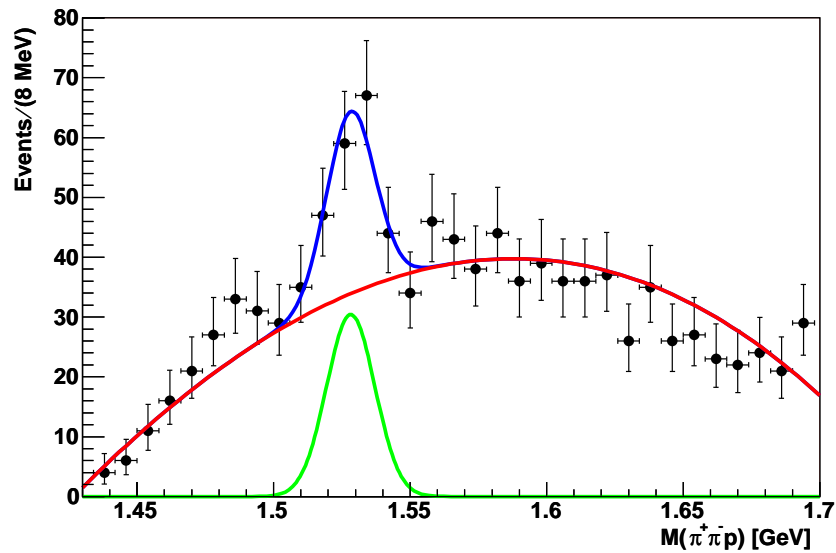


Figure 4.18: The pK_S system mass spectrum after applying cut $|P_K|^2 - |P_N|^2 < 5 \text{ GeV}^2/c^2$.

4.7 Kinematic Reflection

There are doubts about the origin of the resonance at 1530 MeV which has been observed in different experiments. One can consider the resonance to be a kinematic reflection of another state. In the articles [91, 92], the authors suggested that the Θ^+ found in experiments which measured the K^+n channel can be due to a kinematic reflection of $f_2(1275)$, $a_2(1320)$ or $\rho_3(1690)$ mesons. The CLAS collaboration in [93] reject this explanation. But they do not reject the postulation of kinematic reflections outright, only that these particular mesons could reflect in their spectrum due to the production mechanism of the mesons.

We can consider another type of kinematic reflection. The HERMES spectrometer covers only a small region of the phase space of decaying particles. We can ask what happens with the invariant mass spectra if we loose one particle of a decaying product. A special case of interest should be resonances decaying into Λ which decays afterwards into p and π^- . In the laboratory frame, in which Λ is boosted in the forward direction, the proton carries most of the momentum fraction and the angle between the Λ and the proton momenta is small. Let us consider the resonance which decays into $K_S\Lambda$. Could such a resonance produce a peak at the Θ^+ mass if we missed the pion from the Λ decay?

First, we must start to calculate the expected mass of such a resonance. Using the four-momenta conservation law we obtain

$$M_N^2 = M_\Theta^2 + M_\Lambda^2 - M_p^2 + 2P_{K_S}P_{\pi^-}, \quad (4.32)$$

where M_N is the mass of the resonance decaying into a $K_S\Lambda$ system and M_Θ is the invariant mass of the $K_S p$ system, where the proton is produced by the decay of the Λ . M_Λ and M_p are the masses of the Λ and proton respectively. The last term $P_{K_S}P_{\pi^-}$ represents the scalar product of the K_S and the π^- four-momentum. Let us expect the mass of $K_S p$ to be about 1530 MeV. To calculate the mass of the resonance, it is necessary to estimate the value of the $P_{K_S}P_{\pi^-}$. In a first approximation, we can put limits on this number. From the lower side, the product has to be greater then zero. The upper limit can be written as

$$2P_{K_S}P_{\pi^-} \leq M_\Theta^2 - M_{K_S}^2 - M_\pi^2, \quad (4.33)$$

where M_{K_S} and M_π are the masses of the K_S and the π . After substituting the numbers from previous equation, we obtain, that resonance, which could reflect into the Θ^+ peak, has an expected mass in the range from 1645 to 2190 MeV.

In [79], there are thirteen N resonances reported whose masses are within this suggested mass region and which have a decay channel of $K_S\Lambda$. Most of these resonances exhibit a large width in the range of a few hundred MeV. Generally, this fact would make reflection to a narrow peak difficult. On the other hand, the phase-space in the HERMES kinematics is strongly reduced by the geometrical acceptance of the spectrometer. Describing these limits in an analytical way is rather complicated when using Monte Carlo methods. Using the HERMES Monte Carlo software, we can simulate a particle with certain mass decaying into a certain channel and study the response of the spectrometer. In order to save computing resources, the study was limited to a particular resonance.

In order to select the best candidate, the results of the four track analysis were used as a guide. The events where the combination of the proton and π^- mass results in the Λ -mass to within three σ (± 18 MeV) and the combination of the proton and K_S is within 30 MeV of the 1528 MeV peak were selected. The invariant mass of the four hadron tracks ($\pi^- \pi^- \pi^+ p$) was also calculated. In the resulting spectrum (Fig. 4.19) all events falling in the range 1700-1750 MeV are shown. Although the statistics are small, the results

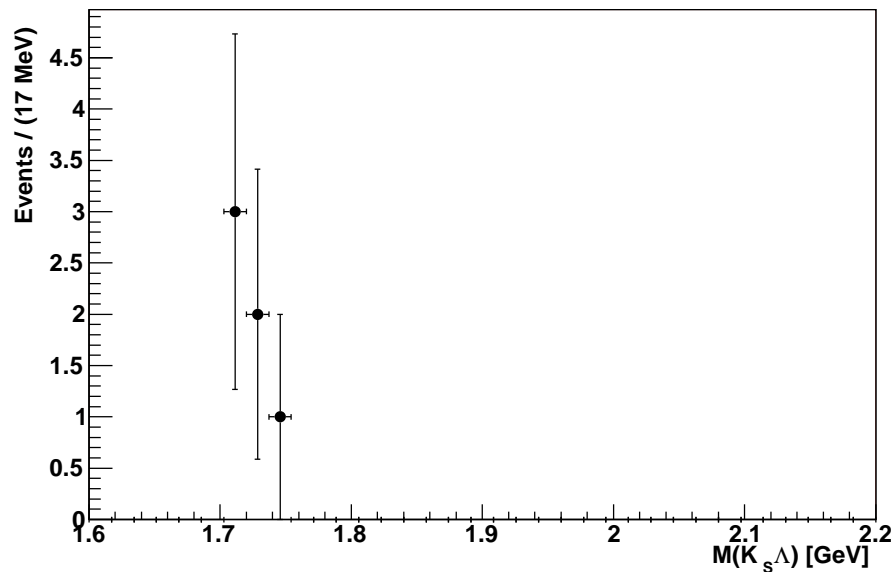


Figure 4.19: The invariant mass spectrum of the events where system pK_S exhibits mass of 1528 ± 30 MeV and systems $p\pi^-$ have mass of the Λ 1116 ± 18 MeV. The π^- is observed as the fourth track in the events.

constrain the possible reflecting resonances. Using the argument that in the case of the Λ decay, most of the energy is carried by the proton, it could be assumed that even in the cases where the π^- is not detected the difference in the invariant mass of the system ΛK_S and pK_S remain similar. Under these conditions, we can expect for such a resonance to have a mass within the range observed in the analysis of the four track events.

4.7.1 N1710

Of the three potential candidates the N resonance with a mass of 1710 MeV has been used for the simulation. The photoproduction cross section of these states under HERMES kinematic conditions is unknown, however - the decision has been taken mainly due to the branching ratio of the ΛK_S channel. Furthermore, the mass difference of 10 MeV among these three resonances is significantly smaller than their widths (which are of order 100 MeV).

The HERMES event generator was used for the simulation of the parent particle. A particle with mass of 1710 MeV and width 100 MeV was generated. The mass distribution is shown in Fig. 4.20 and momenta distributions in x , y and z directions are plotted in Fig. 4.21. Only the ΛK_S decay channel was to be investigated, so the parent particle was made to decay into Λ and K_S at the production vertex. The generated particles were used as input for HMC (The HERMES Monte Carlo) and HRC (HERMES ReConstruction) code in order to study the response of the detector. In the first step, 150000 $N(1710)$ particles were generated in a 4π stereo-angle. The simulated and reconstructed tracks have been further analyzed with the same set of cuts as the real data samples and the mass spectrum of pK_S has been reconstructed. The spectrum is shown in Fig. 4.22.

This spectrum shows a potential peak at the expected mass of the Θ . It is not clear whether this feature is due to small statistics or it is an effect of the limited acceptance of the spectrometer. The HERMES acceptance is restricted only to forward angles. As well as the phase space of $N(1710)$, decay products are limited to forward angles because the mass of $N(1710)$ is only just above the $K_S\Lambda$ threshold. In order to find the origin of the feature and its possible influence on the observed peak in the pK_S mass spectrum, the simulation was performed with three times higher statistics than in the previous simulation so as to have a comparable number of events as in the measured Θ^+ spectrum.

A fit was then performed for the reconstructed spectrum of the $N(1710)$ simu-

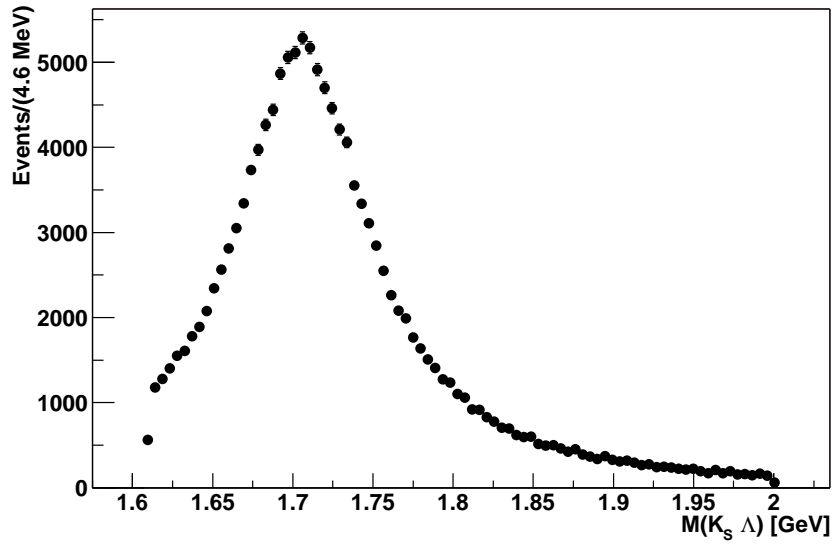


Figure 4.20: The generated mass of the $N(1710)$ resonances.

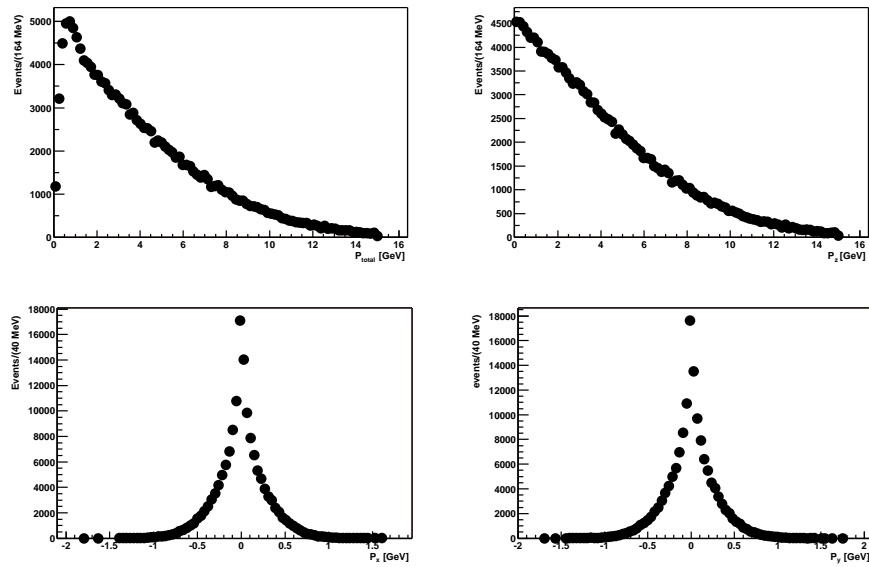


Figure 4.21: The simulated momenta of the $N(1710)$ resonances. The upper left histogram shows the total momentum of the parent particle. The upper right shows the momentum distribution in the direction of the z -axis, lower left in the x -axis and lower right in the y -axis

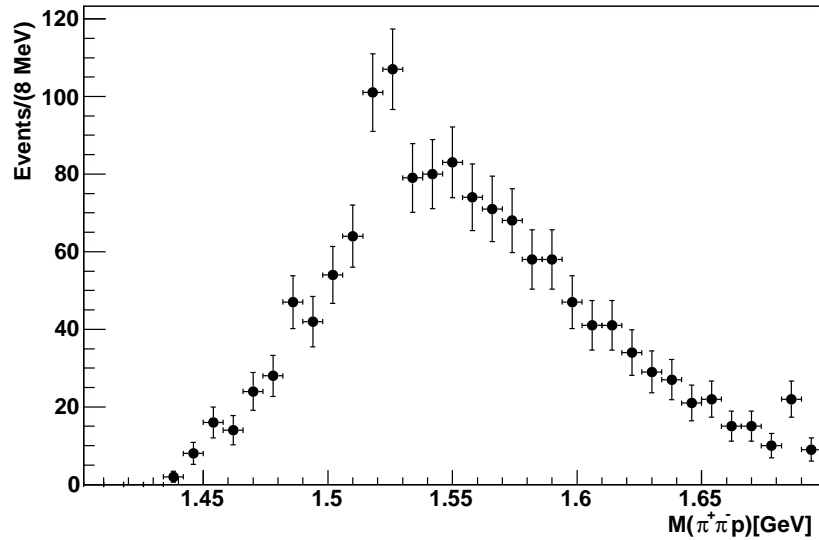


Figure 4.22: The reconstructed mass spectrum of pK_S system. The generated events are coming from decay of $N(1710)$ decaying into $K_S\Lambda$. The π^- from the Λ decay is not reconstructed.

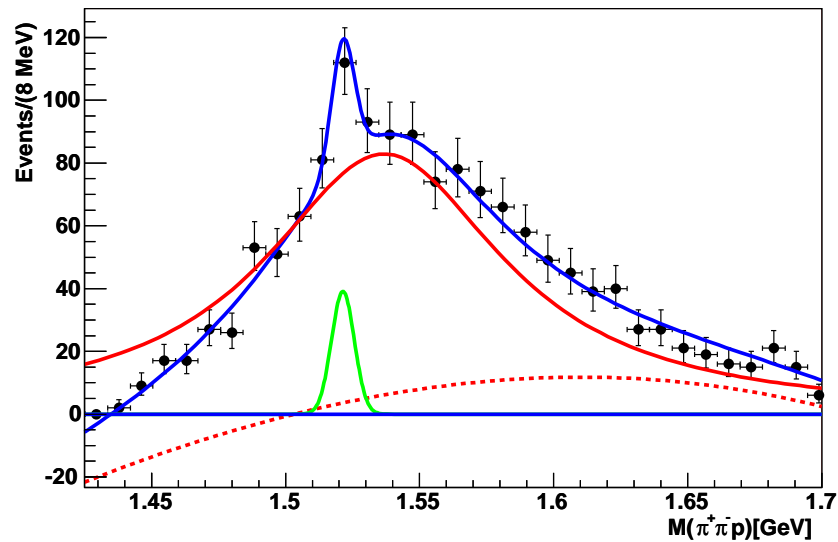


Figure 4.23: The fit of the reconstructed mass spectrum of the pK_S system. The fit function is composed as a sum of Breit-Wigner, Gauss and third order polynomial function

lation. A sum of Gaussian, Breit-Wigner and third order polynomials was found to best describe the shape of the spectrum and is shown in Fig. 4.23. The lower mass part of the spectrum has a similar shape to the measured mass distribution of the pK_S system. This distribution was used together with six Σ^* resonances and a third degree polynomial to fit the data. The result is seen in Fig. 4.24.

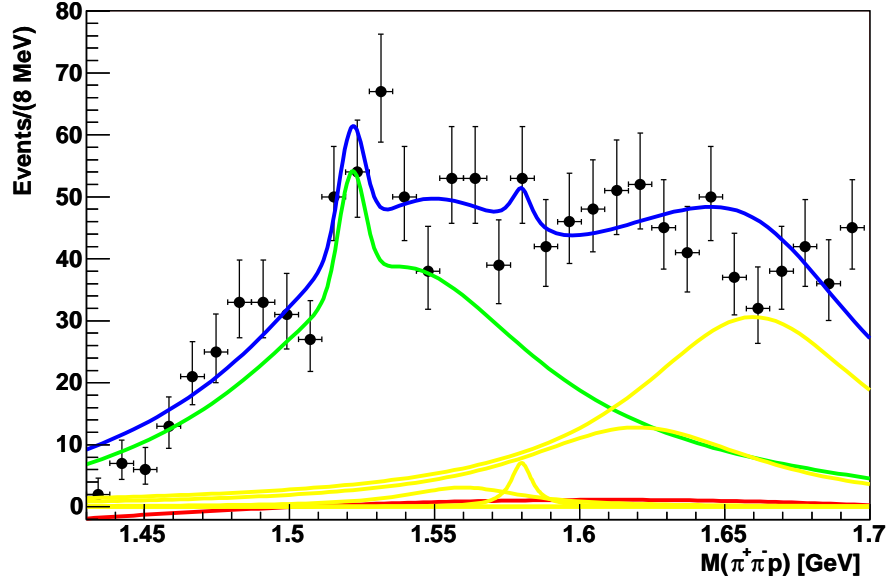


Figure 4.24: The fit of the pK_S mass spectrum. The fit function is the sum of a third degree polynomial, six Breit-Wigner function describing Σ^* resonances and a function obtained from $N(1710)$ kinematic reflection studies.

The description of the spectrum shape is not quite accurate. It has to be stressed that the polynomial function which describes the non-resonant background is close to zero and even partly negative. Such behavior is not consistent with the above-mentioned PYTHIA6 simulation results. The $N(1710)$ is not the only resonance which decays into the $K\Lambda$ system. There are several resonances with masses close to 1710 MeV. This makes the parent distribution smoother as well as the reflected pK_S . Taking into account these facts we can exclude a reflection of the $N(1710)$ as the source of the observed peak.

There are other implications which can be inferred from this analysis. By increasing statistics by a factor of five the “peak-like” feature in the pK_S spectrum disappears as can be seen in Fig. 4.25. The spectrum is smooth without any significant peak-like

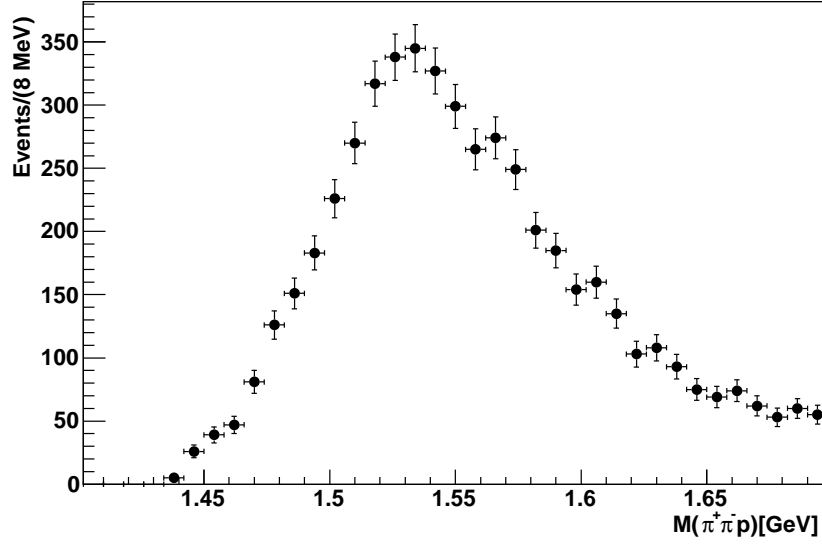


Figure 4.25: The pK_S system invariant mass spectrum obtained by higher statistic simulation of $N(1710)$.

feature. In the light of this study of $N(1710)$, it could be a considered conclusion that the observed resonance in the pK_S system may be explained away as a statistical fluctuation.

4.7.2 $\Xi^0(1690)$

There is another resonance which can decay into the $K\Lambda$ system. This is a member of the Ξ group and has a mass of 1690 MeV. The width of $\Xi(1690)$ is significantly lower than the width of the $N(1710)$ (discussed in previous section). The PDG [79] estimates an upper limit to the width of 30 MeV. In the most recent experimental result [94], the reported width is 10 MeV. The decay branching ratios of this resonance are unknown. The ΛK channel is one of the observed decay channels, the other decay modes are $\Xi\pi$ and $\Sigma\pi$. The resonance has been simulated with the same generator as $N(1710)$, as well as using the same parameters as were used for the momentum description of the parent particle. The analysis of the simulated data was performed with the same set of cuts as the analysis of the measured pK_S system. The detector response to the pK_S system is shown in Fig. 4.26. It resulted in a peak at 1512 MeV with a width of 18 MeV. The width of the resultant peak is two times bigger than the width of the observed Θ^+ and the mass is about 16 MeV lower.

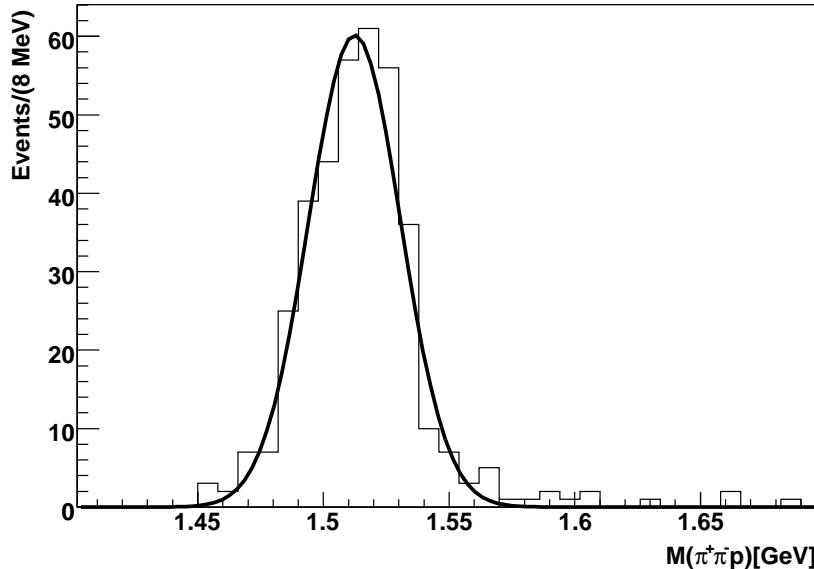


Figure 4.26: The pK_S system invariant mass spectrum obtained by simulation of $\Xi^{*0}(1690)$ decaying into $K_S^0\Lambda$. The peak has been fitted by means of Gaussian distribution.

The resulting mass and width values seems to contradict to the values of the measured Θ^+ . Nevertheless, there is no direct way to exclude this resonance as a possible source of the Θ^+ peak. Firstly, the Ξ might be narrower. There are experiments [95] referring to a width of below 8 MeV. The width reported by yet other experiments [96, 97] is given mainly by their experimental resolution. From both the simulation of the $N(1710)$ and $\Xi(1690)$ it can be seen that the width of the reflecting object depends on the width of the parent resonance. In the case that the real width of the Ξ is smaller than the simulated one, the width of the reflecting peak in the pK_S system could be comparable with the measured width of the Θ^+ .

The discrepancies between the simulated and the measured masses can be explained by uncertainties in the $\Xi(1690)$ data. The PDG [79] reports that 1σ deviation in the average mass reported by the experiments is about 10 MeV. If the mass of the parent particle is higher than the momentum carried by the decay products in c.m.s., it will be higher as well. The K_S is fully reconstructed by its decay product, while from the Λ only a proton is detected. In the case of Λ decay in the laboratory frame, most of the momentum

is carried by the proton. This kinematic constraint leads to the result that the invariant mass of the reconstructed pK_S system is correlated with the invariant mass of the parent ΛK_S system. Under the assumption that the real mass of the Ξ is about 1700 MeV or higher, the mass of the reflecting peak can become consistent with the width of measured Θ^+ .

A hyperon beam was scattered off a copper target in [94] and the ratio between $\Xi(1530)$ and $\Xi(1690)$ was been estimated.

$$\frac{\sigma \cdot \mathfrak{B}\mathfrak{r}(\Xi^0(1690) \rightarrow \Xi^- \pi^+)}{\sigma \cdot \mathfrak{B}\mathfrak{r}(\Xi^0(1530) \rightarrow \Xi^- \pi^+)} = 0.022 \quad (4.34)$$

From the experiment [96], where a Kaon beam was scattered off a proton target, the ratios between particular decay modes of $\Xi^0(1690)$ are known. For our purposes, the most interesting is the ratio between the $K_S \Lambda$ and the $\Xi^- \pi^+$ channel.

$$\frac{\sigma \cdot \mathfrak{B}\mathfrak{r}(\Xi^0(1690) \rightarrow K_S \Lambda)}{\sigma \cdot \mathfrak{B}\mathfrak{r}(\Xi^0(1690) \rightarrow \Xi^- \pi^+)} > 1.1 \quad (4.35)$$

The acceptance of HERMES for $\Xi^*(1530) \rightarrow \Xi \pi$ has been discussed in [98]. Using this acceptance, the photoproduction cross-section of $\Xi^*(1530)$ has been estimated as $\sigma_{\gamma N \rightarrow \Xi^*(1530)} = 8.6 \pm 2.3$ nb. This knowledge can be used to check whether the number of observed Θ^+ can be realistically explained by $\Xi(1690)$. Assuming that the cross-section ratio $\sigma_{\Xi^*(1530)}/\sigma_{\Xi^*(1690)}$ in the photoproduction process is the same as in the production by hyperon beam, and using formula (4.34) and the branching ratio of $\mathfrak{B}\mathfrak{r}(\Xi^*(1530) \rightarrow \Xi \pi) = \frac{2}{3}$, the product of $\Xi^*(1690)$ photoproduction cross-section and the branching ratio can be calculated. We obtain

$$\sigma \cdot \mathfrak{B}\mathfrak{r}(\Xi^*(1690) \rightarrow \Xi \pi) = 0.126 \text{ nb}. \quad (4.36)$$

Using equation (4.35), the lower limit for the cross-section of $\Xi^*(1690) \rightarrow K_S \Lambda$ has been estimated as $\mathfrak{B}\mathfrak{r} \cdot \sigma_{\Xi^*(1690) \rightarrow K_S \Lambda} > 0.14$ nb.

From the simulation we can estimate an detection efficiency ϵ for detection of the pK_S system if the particles are coming from the reaction $\Xi^{*0} \rightarrow K_S^0 \Lambda$. This has been estimated to be $\epsilon = 9.5 \cdot 10^{-5}$. The number of expected events $N_{observed\ pK_S}^{\Xi^{*0}(1690) \rightarrow K_S^0 \Lambda}$ can be calculated by means of the following equation:

$$N_{observed\ pK_S}^{\Xi^{*0}(1690) \rightarrow K_S^0 \Lambda} = \sigma_{\gamma N \rightarrow \Xi^{*0}(1690) \rightarrow K_S \Lambda} \cdot \Phi \cdot \mathfrak{B}\mathfrak{r} \cdot L \cdot \epsilon, \quad (4.37)$$

where the branching ratio cross-section product $\mathfrak{B}\mathfrak{r} \cdot \sigma_{\Xi^*(1690) \rightarrow K_S \Lambda}$ has been estimated in a previous part of this section, L is integrated luminosity ($L = 295.7 \text{ pb}^{-1}$,

Φ is photon flux factor equal to 0.02 GeV^{-3} and ϵ is the detection efficiency of the pK_S system originating from the $K_S^0\Lambda$ decay channel of $\Xi^{*0}(1690)$. The calculation results into $N_{\text{observed } pK_S}^{\Xi^{*0}(1690) \rightarrow K_S^0\Lambda} = 0.07$ events, which is a number three orders of magnitude lower than has been observed in the measured spectrum. With this result we can rule out the possibility that the Θ^+ peak is due to a reflection of $\Xi^*(1690)$.

4.8 Summary of the Pentaquark Analysis

All of the analyses performed in this chapter were aimed to collect all pertinent information which can be used to solve the problem of the existence of the Θ^+ . The analyses started by cross checking the results reported by the HERMES collaboration in [18], and next work was focused on studies of the pK_S system kinematics, which brought an indication of the possible non-isotropic behavior of the observed peak. This was achieved by analysis of the angular momentum distributions. Additional kinematical analysis was used to test the Karliner-Lipkin scheme [90] which was applied to the $\Lambda(1520)$ and its decay into the pK^- system. This test showed that the Karliner-Lipkin works under HERMES kinematic conditions. Application of this scheme to the pK_S system found that it could be a useful tool to suppress background for future study of the reaction mechanism. Nevertheless, due to low statistics, further measurement is necessary in order to be able to use both analyses to find a more detailed picture regarding the existence of the Θ^+ .

The creation of the peak structure in the pK_S mass spectrum was studied in the additional analyses by means of kinematic reflections which have been frequently discussed as possible sources of the observed narrow peak. This would be a natural solution to the discrepancies between experiments which observed the peak and those which reported negative results. The resonances decaying into the $K_S\Lambda$ system have been analyzed as possible sources of the peak in the pK_S mass spectrum. The results show that these candidates can be ruled out. The $N(1710)$ can not produce a narrow structure due to its own broad width. The $\Xi(1690)$ reflects into a narrow peak, but the mass of the reflected peak is too low. In addition, a stronger argument against this hypothesis comes from comparing known branching ratios of $\Xi(1530)$ and $\Xi(1690)$. From the measured yield of $\Xi(1530)$ and the spectrometer acceptance, the expected number of events is factor of a thousand times smaller than the observed one.

Although the HERMES pentaquark signal has a limited significance and tests

to produce this peak in artificial way were performed, the existence of the strange exotic pentaquark could neither be proven nor be ruled out. Further measurements will run with an improved trigger and the Recoil Detector in order to seek a more satisfactory solution. If the Θ^+ is confirmed, the production mechanism at HERMES can be studied in detail by means of angular momentum distribution or the Karliner-Lipkin scheme as shown in this work.

Chapter 5

The Recoil Project

In the previous chapter it was shown that only for one of a thousand pK_S from the mass window around 1530 are all three decay particles detected. In the forward direction, the restricted acceptance of the spectrometer is the limiting factor for the detection efficiency of particles decaying into a multi-hadronic final state. Whenever the parent particle exhibits a small boost, one or more particles have the chance to escape detection under a larger angle than the detector acceptance. Furthermore, the photoproduction cross-section generally decreases with an increasing momentum of the produced particle. By means of enhancing the spectrometer acceptance to larger angles the situation can be changed considerably. This will be achieved by installing a Recoil Detector in the target region of the HERMES spectrometer. The Recoil Detector is the subject of this chapter. The original motivation of this detector is not the pentaquark search, but the measurement of Generalized Parton Distribution.

5.1 Generalized Parton Distributions

The scattering amplitude of inclusive and semi-inclusive DIS can be described in terms of polarized and unpolarized parton distribution functions. The Generalized Parton Distributions (GPDs) [99, 100, 101, 102] are natural extensions of parton distribution functions and are suitable to describe the exclusive processes in the off-forward ($t \neq 0$) kinematic regime. For this reason GPDs are sometimes called off-forward distribution functions.

GPDs are expressed in terms of four distribution functions. Two unpolarized ($H^q(x, \xi, t)$ and $E^q(x, \xi, t)$) and two polarized ($\tilde{H}^q(x, \xi, t)$ and $\tilde{E}^q(x, \xi, t)$), where kinematics

are parameterized in terms of x, ξ, t , where x represents the momentum fraction carried by the struck quark. The ξ variable is called “skewness” and is given by the difference of the momenta of outgoing and incoming quarks from the nucleon. The t parameter is the Mandelstam kinematic variable. In the forward limit ($\xi = 0, t = 0$) the GPDs H and \tilde{H} become quark distribution functions.

$$H^q(x, 0, 0) = q(x), \quad \tilde{H}^q(x, 0, 0) = \Delta q(x), \quad (5.1)$$

where $q(x)$ and $\Delta q(x)$ represents spin-independent and spin-dependent quark densities. The functions E and \tilde{E} have no such straight-forward interpretation. The first moments of the GPDs are the flavor-dependent form factors:

$$\int_{-1}^{+1} dx H^q(x, \xi, t) = F_1^q(t), \quad \int_{-1}^{+1} dx E^q(x, \xi, t) = F_2^q(t) \quad (5.2)$$

$$\int_{-1}^{+1} dx \tilde{H}^q(x, \xi, t) = g_A^q(t), \quad \int_{-1}^{+1} dx \tilde{E}^q(x, \xi, t) = h_A^q(t), \quad (5.3)$$

where $F_1(t)$ and $F_2(t)$ are the Dirac and Pauli form factors and $g_A(t)$ and $h_A(t)$ are the axial-vector and pseudo-scalar form factors. In the forward limit, second moments of E and H are related to the total angular momentum carried by the quarks of the flavor a :

$$\lim_{t \rightarrow 0} \frac{1}{2} \int_{-1}^{+1} dx x [H^a(x, \xi, t) + E^a(x, \xi, t)] = J^a, \quad (5.4)$$

The sum over all flavors a gives a total quark orbital angular momentum by the relation:

$$J = \frac{1}{2} \Delta \Sigma + L_q \quad (5.5)$$

The contribution of the quarks' angular momentum L_q to the nucleon spin can also be decomposed. The $\Delta \Sigma / 2$ is the quark spin contribution available from inclusive and semi-inclusive polarized DIS.

In the HERMES experiment, these GPDs can be accessed through measuring Deeply Virtual Compton Scattering (DVCS) or Hard Exclusive Meson Production (HEMP):

$$\gamma^*(q) + T(p) \rightarrow \gamma(q') + T'(p'), \quad \gamma^*(q) + T(p) \rightarrow M(q') + T'(p') \quad (5.6)$$

where virtual photon γ^* with high energy and virtuality Q^2 scatters off the nucleon target T and produces a real photon γ or meson M and hadronic state T' . The DVCS process has the same final state as a Bethe-Heitler (BH) process, thus both processes interfere. In the HERMES kinematic regime BH dominates. The appropriate diagrams are shown

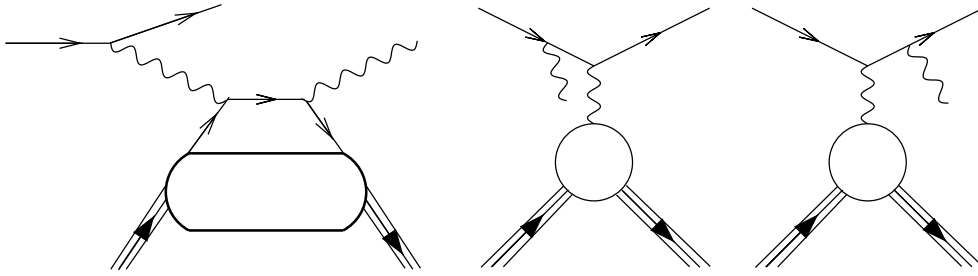


Figure 5.1: The Feynman diagram of the DVCS and competitive Bethe-Heitler process

in Fig. 5.1. Nevertheless, the interference between both processes can be used as a lever arm and particular GPDs can be extracted from measured asymmetries. The total angular momentum of the quarks is accessible by measurement of DVCS at low t . Therefore a clear estimate of the final state of the process is necessary. Analysis of DVCS from recent HERMES data is already done. Only the γ and lepton are detected - the proton from DVCS is not detected due to the limited acceptance of the spectrometer. In order to select exclusive events with only a proton, γ and lepton in the final state, a missing mass technique is used. The momenta of initial states are known. By applying conservation law, the invariant mass of the missing particle in the final state is computed. The resulting missing mass spectrum is shown in Fig. 5.2, where the measured data is compared with a Monte Carlo simulation. The data is depicted by black points and the simulation results are represented by colored histograms. The magenta peak around 1 GeV^2 corresponds to events with only one proton in the final state. The blue part of the histogram corresponds to fragmentation background. The resolution of the missing mass technique is not perfect, and from the simulation it is seen that separation of the proton from Δ -resonances in the final state is not possible.

5.2 The Detector

In order to improve the resolution in such a way that the GPDs are accessible at the HERMES experiment, the Recoil Detector [103, 104] was proposed. The main goal is measurement of DVCS in the forward kinematic region. The Recoil Detector has to be able to provide particle identification for pions and protons in order to guarantee exclusivity of

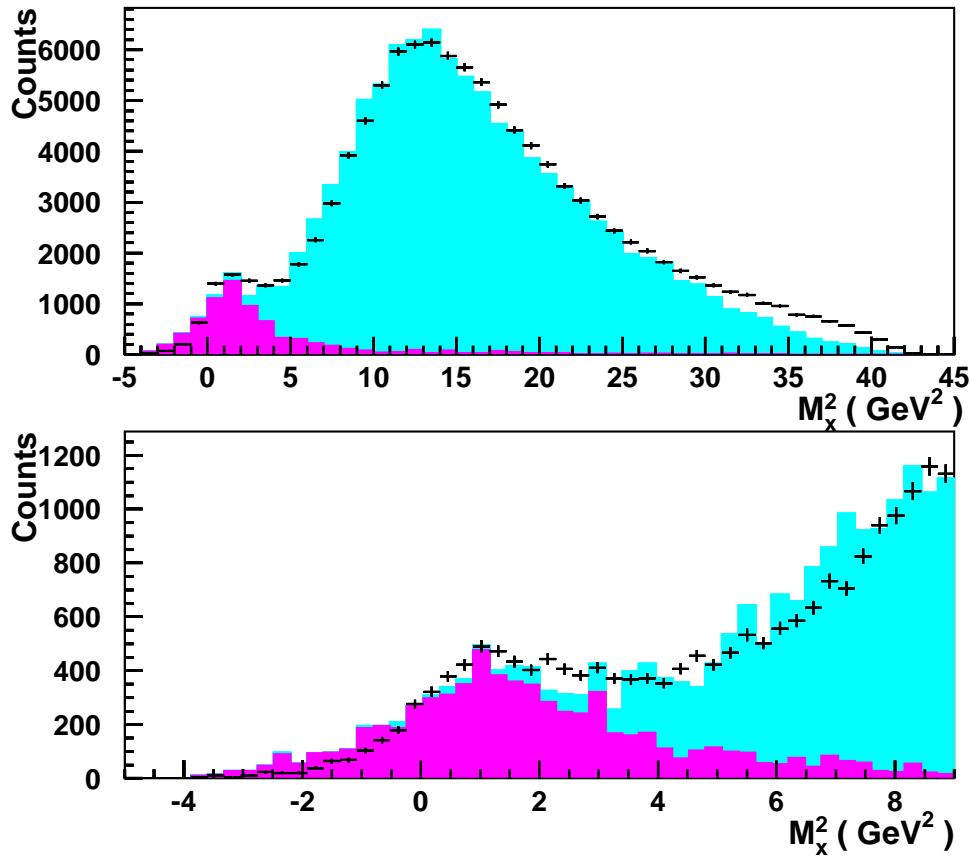


Figure 5.2: The missing mass spectrum of the DVCS process. The black points correspond to the measured data. The magenta area are MC DVCS events, the light blue area are events from fragmentation background

the events. This is to be achieved by a system of three different detectors (see Fig. 5.3). The silicon detector in the beam pipe vacuum, two barrels of scintillating fibre tracker (SFT) and a photon detector. All of the detectors are surrounded by a solenoidal superconducting magnet with a magnetic field of approximately 1 T in the bore.

The silicon detector would provide measurement of space points for track reconstruction. The momentum range of the protons detected by the silicon detector is 134 - 450 MeV/c. A measurement of the energy deposition ΔE in the silicon detector layers is a reasonable tool to achieve proton/pion separation. For low momenta protons (below 250 MeV/c) a large signal in the silicon detector is expected and no signal in SFT detector. Pions of the same momenta produce a small signal or no signal in the silicon detector and produce a signal in the SFT.

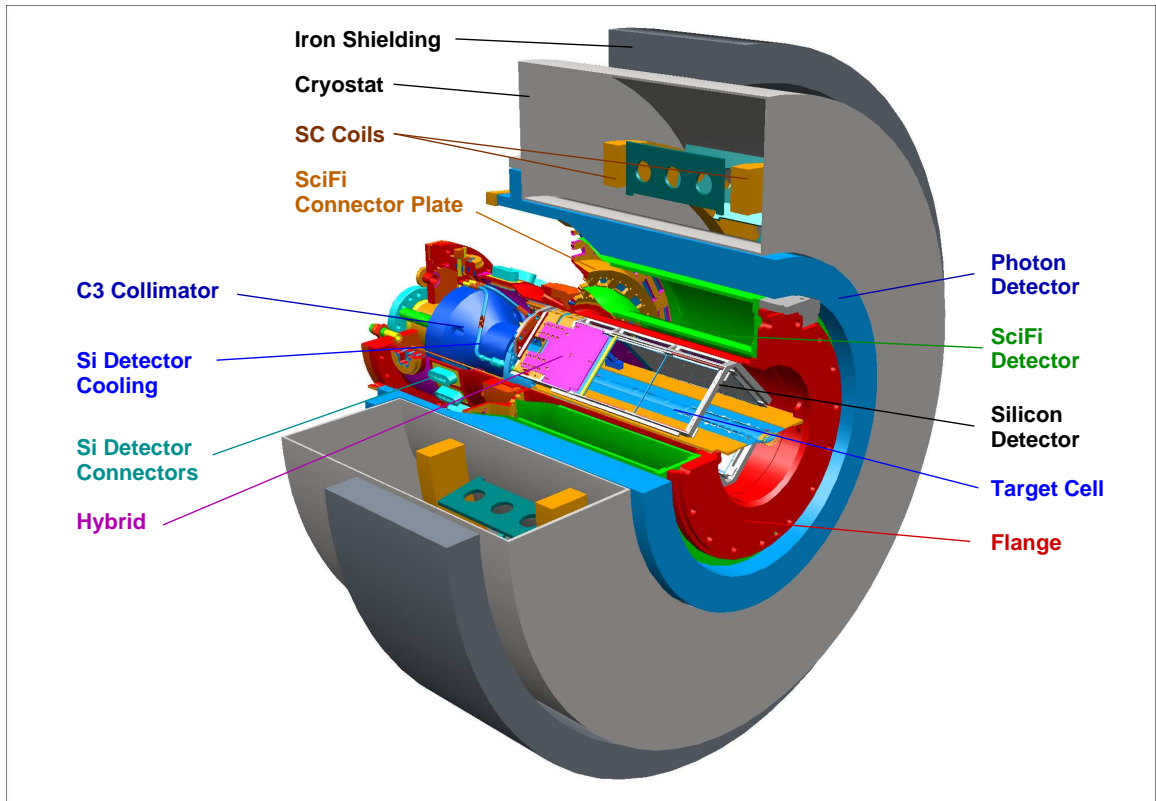


Figure 5.3: 3D View of the Recoil Detector

In the momentum interval of 250 to 450 MeV/c, the momentum dependent cut on the total energy deposition ΔE in the SFT detector should provide particle identification. For momenta above 650 MeV/c, pion rejection drops down. It is expected that additional information from the photon detector may improve PID reliability up to 800 MeV/c. Identification of π^0 decaying into γ is the goal of the photon detector. This is needed in order to suppress background from Δ -resonances.

The silicon detector consists of eight silicon modules arranged in a double-layered diamond formation around the HERMES target cell (see Fig. 5.3). Each module consists of two double-sided TIGRE wafers with a “hybrid” of readout electronics, one hybrid for each side of the wafer. The HELIX 3.0 chip was chosen for the readout of the silicon detector after its predecessor, the HELIX 2.0, was used in the readout of the Lambda-Wheel (LW) detector which was installed in HERMES in 2002.

The Scintillating Fibre Tracker (SFT) is designed to measure and identify protons

and charged pions in the momentum range of 250-1600 MeV/c. The charge of the particle and its momentum are identified by the bending radius of the particle track in the magnetic field. Particle identification is based on measurement of the deposited energy in the scintillating fibres.

Two concentric barrels were built from 1 mm Kuraray SCSF-78 M scintillating fibres. The inner one has a 220 mm diameter and the outer one has a 370 mm diameter. Each barrel is composed of two sub-layers of fibre. In the first one, closest to the beam, the fibres are parallel to the beam direction. The fibres in the second layer form a helix shape under a stereo angle of 10° with respect to the beam direction.

A side view of one layer is shown in Fig. 5.4. The barrels are built as a self-supporting structure to minimize the material traversed by the particle. Each barrel layer is assembled using pre-shaped modules consisting of 64 fibres arranged in two sub-layers. The downstream end of the fibres are machined for optical quality and aluminized. The reflecting face enhances the light yield by up to 30 %. The upstream parts of the fibres are glued into customized connectors which are fixed by screws to an aluminum connector ring.

The light from each scintillating fibre is guided by means of a bundle of sixty-four four-meter long lightguide fibres to Hamamatsu H7546B photomultipliers. This enables the setup of PMTs boxes in an area with a relatively low magnetic field. The fibres are connected to multianode PMTs by means of a customized connector. The fibres from the inner barrel are connected one per pixel, whereas for the outer barrel there are two fibres coupled to one pixel. Due to stray magnetic fields at the location of the PMTs in the experimental area, the PMT and lightguides connectors are surrounded by two U profiles of μ -metal plates and soft iron boxes.

The photon detector consists of three concentric barrels each built of a tungsten radiator and plastic scintillator strips. Along each strip a pair of wavelength shifting fibres are installed. These collect light from the scintillator and guide it to the connector ring. At the connector ring, a light-guide fibre is connected and the light is sent to a 64-channel Hamamatsu H7546B photomultiplier. The readout is provided by means of a CAEN QDC V792.

A solenoidal superconducting magnet surrounds all detectors and provides a near-homogeneous magnetic field parallel to the beam axis. The deflection of the charged particles in this magnetic field is used as a tool to estimate their momenta. By combining space points interactions of a particle in the silicon detector and SFT, track reconstruction

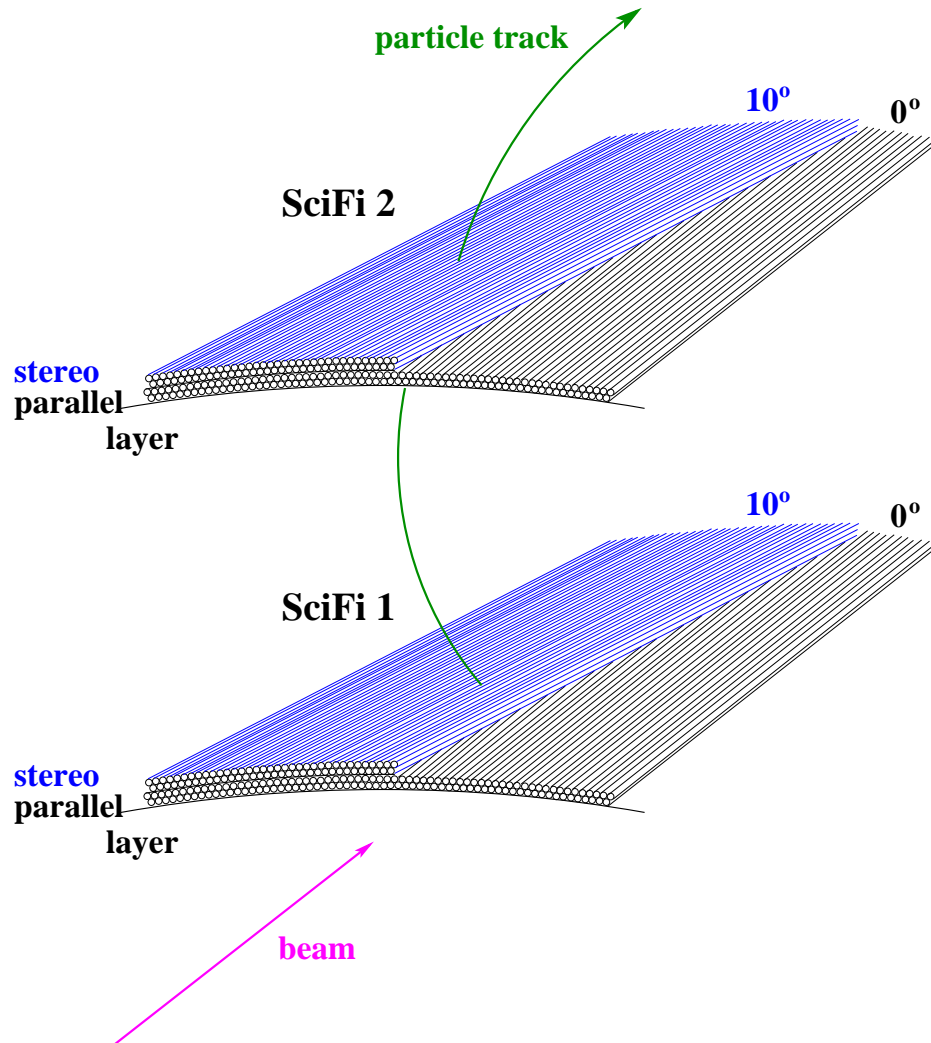


Figure 5.4: The schematic view of fibre layout in the Scintillating Fibre Tracker. The fibres of the inner sub-layers are orientated parallel to the beam axis. Fibres wrapped around the barrel in a helix-shaped in the outer sub-layers form a stereo angle of 10° with respect to the beam direction. Two sub-layers are built into each of the parallel and stereo layers of either barrel.

is possible. The curvature of the track gives information about the transverse momentum component.

5.3 SFT Frontend Electronics

The SFT contains, in accordance with proposal [104], 7000 scintillating fibres, which are connected to multi-anode photomultipliers.

Due to the number of channels which have to be read out in the case of SFT, the full assembly configuration uses 78 PMTs each containing sixty-four channels. This limits the choice of possible read-out electronics. Commercial readout systems available on the market are not suitable for the SFT due to cost considerations. The price of such a system exceeds 100 € per channel which was not feasible given the budget of the Recoil Detector project. An investigation of various possible readout systems was made to find a system which is able to handle photomultiplier signals and can provide information about the deposited energy. The constraint of measuring energy deposited in the scintillating fibres excludes using the same electronics as the RICH or MWPC (multi-wire proportional chamber). Already in the HERMES experiment there is a PCOS4 readout system for these detectors but it only provides logical information about channels with a response over a predefined threshold. This evidently cannot fulfill the deposited-energy requirement. It is this requirement that also makes the ASDL based readout used in HERA-B unsuitable for the SFT. Eventually the decision was taken to base the readout upon the HADES RICH detector. This decision was mainly due to two factors - the previous knowledge about such a readout available at Gießen and the low price point at 10€ per channel.

The HADES RICH readout system is built from a VME module which processes digital signals and preprocessing frontend modules (PFM) with an analog part and first level trigger logic function. The logic function is implemented by means of field programmable gate array (FPGA) technology. This gives a flexibility-allowing configuration of the logic for different tasks. The analog part of the read-out electronics is based on the GASSIPLEX [105, 106] chip, which is a 16-channel amplifier-shaper integrated circuit. The scheme of the GASSIPLEX is seen in Fig. 5.5. The GASSIPLEX chip is developed for readout of gaseous or silicon detectors and its main component is a charge sensitive amplifier (CSA). The CSA of the GASSIPLEX is followed by a deconvoluting filter for usage with gas detectors. The filter has two modes: "silicon" (Si) and "gaseous" (gas) mode. In Si mode the filter function

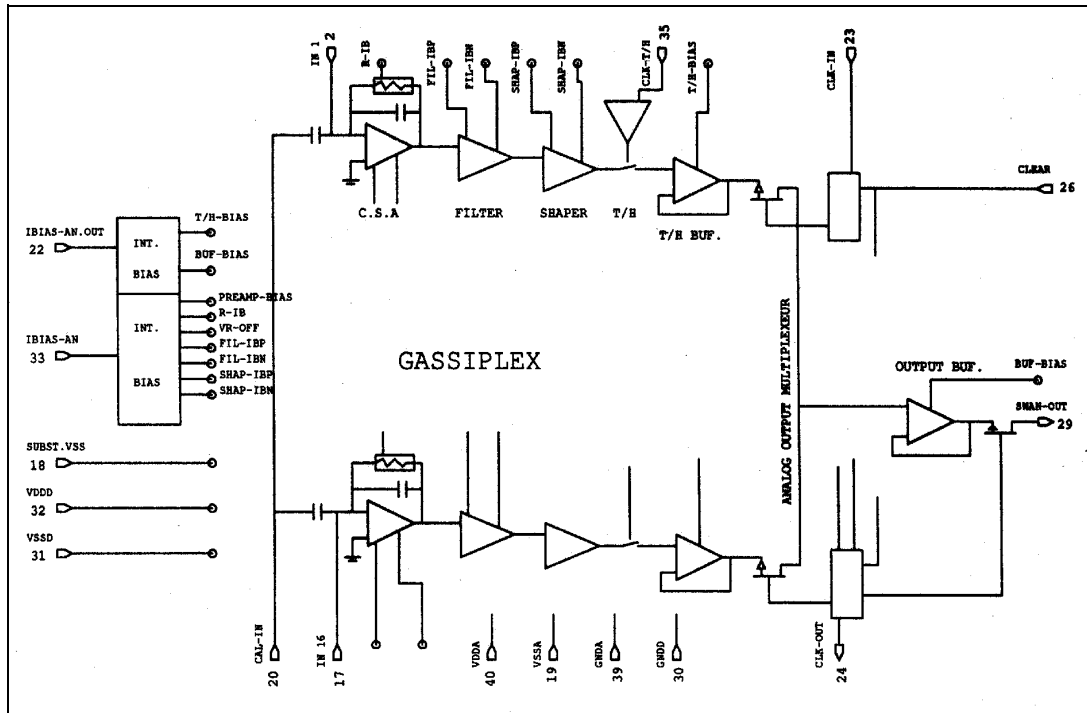


Figure 5.5: Scheme of internal structure of GASSIPLEX

is switched off whereas in gas mode the transfer function is the inverse of the detector signal in order to compensate for the long hyperbolic current tail. The dynamic range varies from -120 to 300 fC for Si mode (without filter), and from -75 to 150 fC for gas mode. The third stage of the chip is a shaper with peaking time of about 600 ns. The output signal of the shaper is transferred to the track&hold buffer, which is connected by means of a multiplexer to the output line.

On the PFM an older version of GASSIPLEX is used which differs slightly from the referred one [106]. The chip is built with $1.5\mu\text{m}$ technology and is not the $0.7\mu\text{m}$ final version. This mainly impacts on the sensitivity of the amplifier, which in the case of GASSIPLEX1.5 is 11.2 mV/fC . GASSIPLEX1.5 is powered by $\pm 3.3\text{ V}$ while the GASSIPLEX 0.7 uses a standard TTL voltage of 5 V .

The control interface of the GASSIPLEX consists of an analog output for the multiplexed signal and logic inputs for track&hold-, clock- and clear-operations. The analog input signals processes continuously and in parallel. After receiving a trigger signal, a

track&hold buffer is disconnected from the shaper output. By means of multiplexing, amplitudes from each track&hold buffer are transferred to the analog output. The multiplexing procedure is controlled by external clock signals. After the multiplexing is finished, a clear signal is sent to discharge the track&hold buffers. After discharging, the chip is ready for the next event.

Each PFM is assembled with four GASSIPLEX chips which enable readout of 64 analog input channels. The block scheme of the PFM is shown in Fig.5.6. Output channels

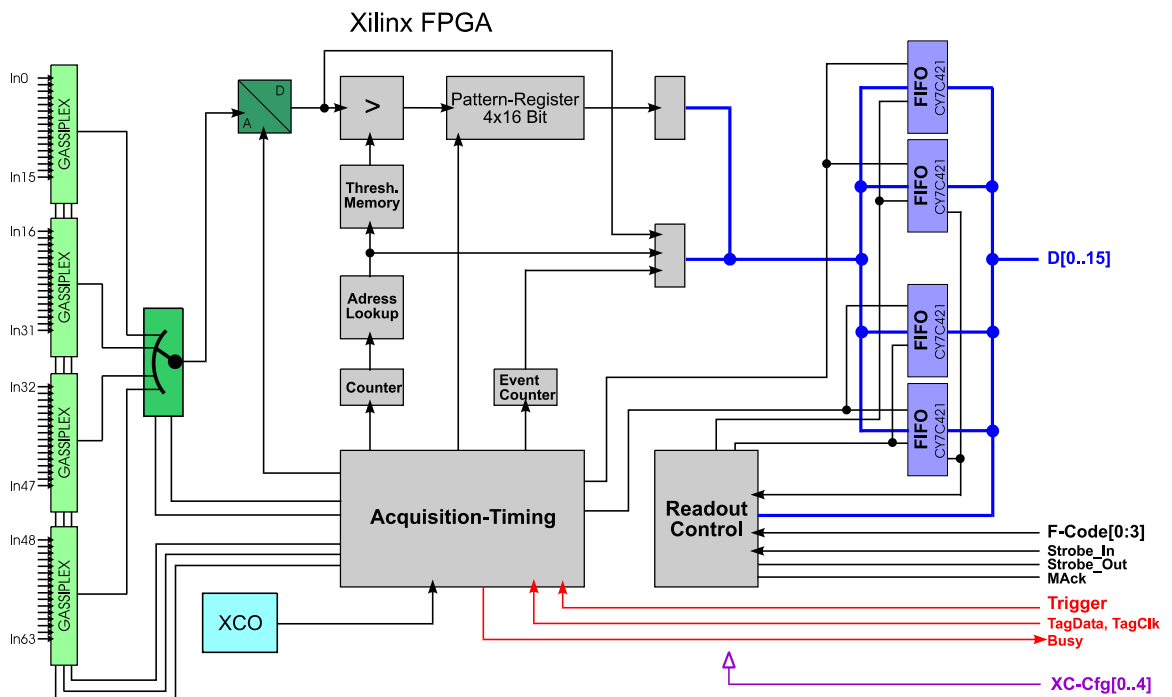


Figure 5.6: Block scheme of the PFM board

of the four GASSIPLEXes are multiplexed by means of the analog multiplexer EL4441 from Élantec. The analog multiplexer is a four input video-multiplexed amplifier with a common feedback input [107] and a switching time of 8 ns. Digitization of the analog signal is provided by a Burr-Brown ADS820 analog-to-digital converter (ADC) [108]. The ADC includes a 10-bit quantizer with internal track&hold, reference and power down features.

The FPGA devices are unlimitedly reprogrammable which offers the ability to a change the logic in a very flexible way. All logic functions of the PFM are implemented

by the FPGA XC4005E from Xilinx. The gray boxes in Fig. 5.6 correspond to functions programmed into the FPGA. The digital value of the measured signal is compared with the threshold value for the corresponding readout channel. Accepted events are 10 bits of information extended by six bits of channel address. The 16 bit long word is parallel-stored in two FIFO banks (capacity 1024 words [110]), called pattern and analog. The 16 bit transceiver SN74ACT16245 provides communication interface between the FPGA on PFM and the RC (Readout Controller) in the VME crate.

5.3.1 Signal Handling in the PFM

The trigger signal is directly transferred to the GASSIPLEX chip. It switches the GASSIPLEX into “hold” mode. The trigger activates a BUSY signal in the FPGA which disables that other trigger signals are not accepted. The system clock of 30 MHz on the PFM boards is provided by a programmable crystal oscillator MG-7010 [109] and is used as a base for particular control signals for the GASSIPLEX multiplexers and common analog multiplexers. Multiplexing (see Fig. 5.7) and digitized signals are transferred into the FPGA channel-by-channel where a threshold comparison is performed. Two different

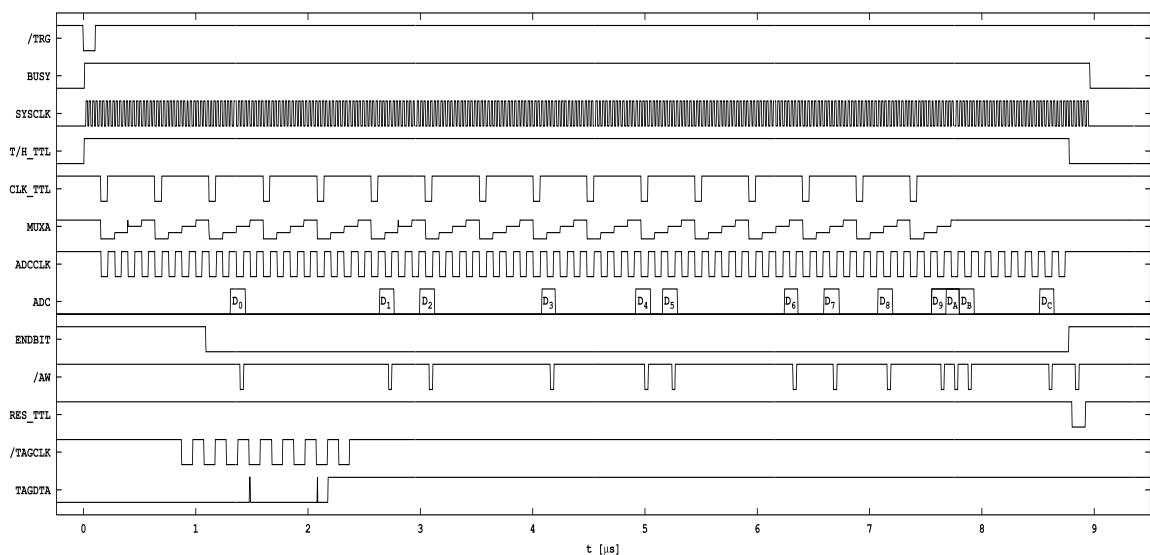


Figure 5.7: Timing of a complete sample cycle

readout cycles are used for data transfer from PFM FIFO memory to the RC. They are called pattern-(PRDOU_T) or analog-readout (ARDOU_T) according to which of two FIFOs bank is read-out. The timing of both cycles is, in principle, the same. This feature is used within the HADES readout cycle for processing data by first and second level trigger signals. Except during the transfer of data to the next processing cycle by the RC, the data of one particular event can be deleted. Only the ARDOU_T cycle was used during the test experiment of the SFT. In addition, the final read-out scheme of the SFT in the running of the Recoil project is designed to use only the ARDOU_T cycle to transfer data to the RC.

Up to eight PFMs can be plugged into one backplane board which provides a connection to one port of the readout controller. The readout of boards connected to one port is processed by means of a daisy-chaining operation. It is provided by the handshake lines StrobeIn(/STRBI), StrobeOut(/STRBO) and ModuleAcknowledge(/MACK). The design of the daisy-chain read-out of five boards is seen in Fig. 5.8. More precise descriptions of the PFMs' functions are in [111].

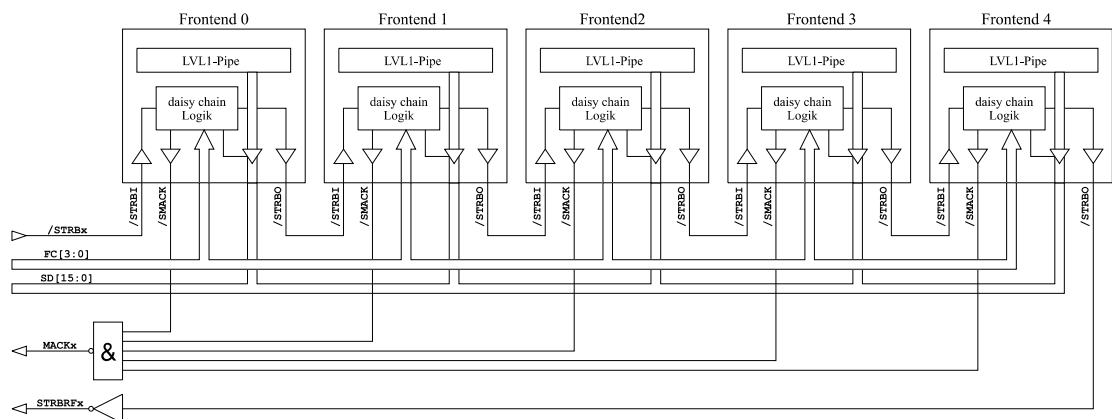


Figure 5.8: Daisy chained connection of five PFMs

The Readout Controller(RC) is a 6U VME board which provides an interface between the PFMs, the Detector Trigger Unit (DTU), the Central Trigger Unit(CTU) and the Imaging Processor Unit (IPU). A through description of the functionality of the RC is given in [112]. Communication, diagnostics and data transfer operations are provided by a standard VME bus. Communication between the DTU and the RC runs over a privately definable part of the VME bus. The DTU provides signal handling for data transfer from

the PFMs to the RC, from the RC to the VME-controller and from the RC to the IPU. Since only the TRG, the ARDOUT and the BUSY signals are needed for read-out of the SFT, the DTU is replaced with a simplified-state machine. The machine transmits a TRG signal directly to the RC. In coincidence with the TRG, it receives a BUSY signal from the RC. The BUSY signal is used as a simplified-state veto for double triggering of the RC. After $10\ \mu\text{s}$ (which are needed for the digitization of the signal) the machine releases the ARDOUT, which starts data transfer from the PFMs' FIFO to the second level buffer on the RC. At the end of the ARDOUT transfer, the BUSY signal is set to 0, then the PFMs are enabled to accept the next event.

5.3.2 Testing and Setup of the PFMs for Readout of PMT Signals

The HADES RICH readout electronics exhibit some features which limit direct use of these electronics for readout of the SFT. The first constraint is that the PMTs provide a short negative pulse of the order of a few nanoseconds while the PFMs are designed for positive signals with a length of the order of hundreds of nanoseconds. The second constraint was the different dynamic range of the PMTs and the GASSIPLEX chip. The gain of the 64-channel PMTs varies from 10^5 to 10^6 with supplied high voltage, which in the case of single photoelectron event corresponds to a charge of 16 - 160 fC, while the dynamic range of the GASSIPLEX chip for negative charge is up to -120 fC. The expected signals from low momenta protons are, according to simulations [113], about 70 photoelectrons (P.E.). By combining these signals with the gain of the PMT of 10^5 to 10^6 , the expected amount of charge on the electronic input is up to 11 pC. The main focus of the work performed on the design of the readout electronics of the SFT was to solve these problems. A description of the work and the results which followed are presented in this section.

A first test was designed to allow a short signal to be supplied to the GASSIPLEX chip which has a long integration time constant. The short PMT-like pulse was produced by a pulse generator which provided a rectangular pulse with a leading edge of 700 ps. This pulse was then differentiated by a 1 pF serial capacitor and a parallel $50\ \Omega$ resistor. The pulse shape obtained is very similar to the shape of the PMTs' output signals. The RC-circuit was connected to the GASSIPLEX input and the response to different pulse voltages and lengths was tested. The tests showed a reasonable linearity between pulse height and ADC output value as shown in Fig. 5.9. Recorded data values begin at 100 mV is due to

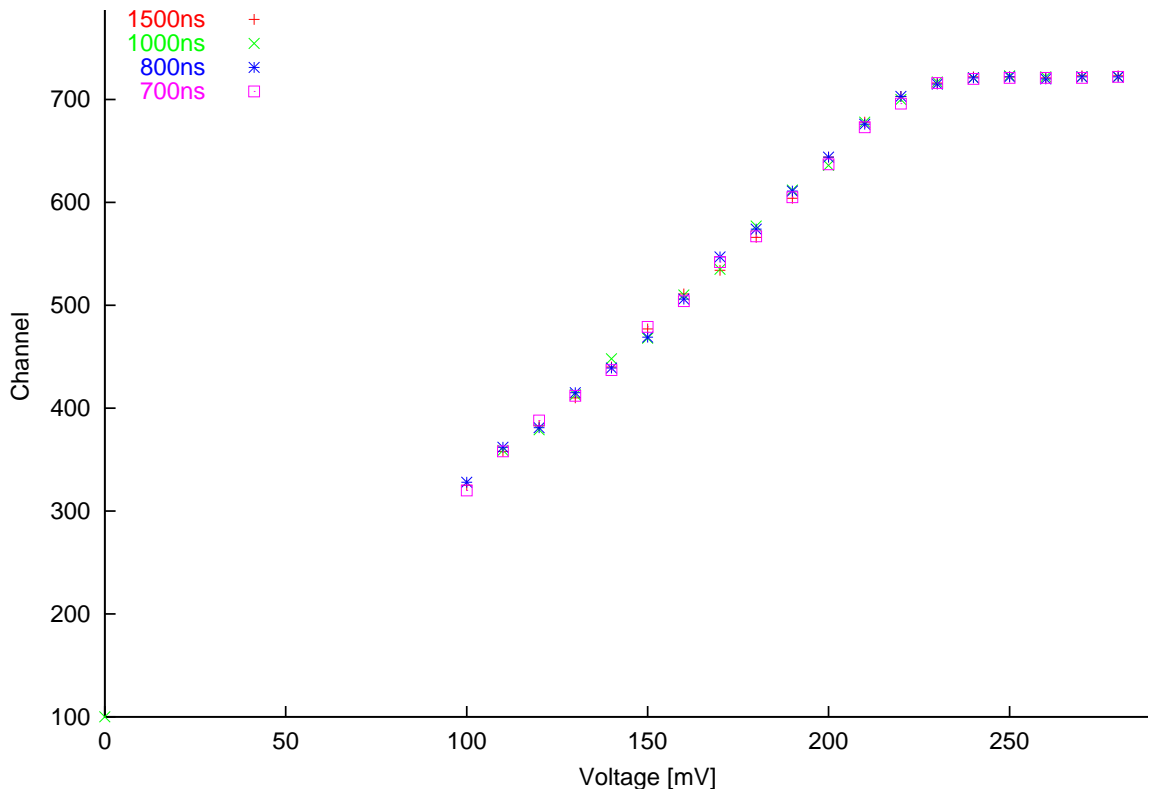


Figure 5.9: The result of the test of the PFMs response on the voltage of the input pulse.

the minimum amplitude provided by the pulser. The plateau at 220 mV corresponds to the saturation of the GASSIPLEX chip and the analog multiplexer.

The GASSIPLEX chip could accept both negative or positive input signals. The analog multiplexer between the GASSIPLEX chip and the ADC can operate with both polarities as well. The ADC input signals are in the range 1.25 V - 3.25 V. The signals out of the dynamic range of the ADC are converted as 0 or 1023 respectively. There are two options which were considered to shift the output signal of the multiplexer into the range of the ADC. The first option was to install a signal-inverting amplifier between the multiplexer and the ADC. Unfortunately, this required redesigning the PFMs printed circuit board (PCB). The second option was to use feedback resistors of the multiplexer to increase the base-line offset, so that without input signals to the GASSIPLEX chip the output voltage of the multiplexer would be about 3.25 V. The resistors R27 and R28 (see Fig. 5.10) are responsible for the offset. The gain of the multiplexer is given by resistors

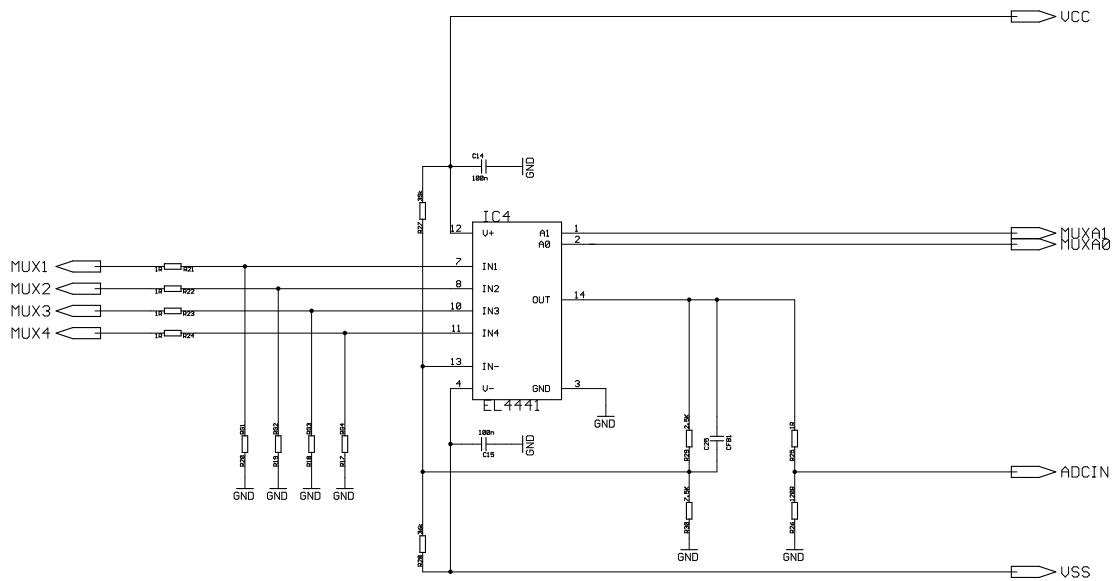


Figure 5.10: Analog Multiplexer Scheme

R29 and R30. The original values are $R27 = 39 \text{ k}\Omega$, $R28 = 2.2 \text{ k}\Omega$, $R29 = 120 \Omega$ and $R30 = 120 \Omega$. Care had to be taken with all the resistors which are responsible for the gain because of the big shift in the offset. The optimal resistor combination was found to be $R27 = 33 \text{ k}\Omega$, $R28 = 5.6 \text{ k}\Omega$, $R29 = 3.3 \text{ k}\Omega$ and $R30 = 8.2 \text{ k}\Omega$. A consequence of the change to the base-line offset and usage of the negative input signals was an inversion of the ADC values, i.e. events with a higher ADC number correspond to a lower signal and vice versa.

The drawback of this solution is that a part of the ADC range is lost. The ADS820 analog-to-digital converter is designed for an input signal in the range of $+1.25 \text{ V} - +3.25 \text{ V}$. This means that the base-line offset of the analog multiplexer has to be shifted to 3.25 V . The maximum output values of the analog multiplexer are given by power supply voltages. These can be within a $\pm 15 \text{ V}$ range, according to the data sheet [107]. The multiplexer on the PFMs is supplied by a $\pm 5 \text{ V}$ power line. Laboratory tests showed that by increasing the supply voltages, the base-line approaches 3.25 V . On the other hand, the $+5 \text{ V}$ power line is used to supply all digital elements on the PFMs which are working with TTL logic. Since the TTL elements require an exact $+5 \text{ V}$ power supply, a base line voltage of 3.25 V is unreachable without redesigning the PCB. Thus the necessary shift of the ADC base-line

could only be achieved by changing the feedback resistors which caused a loss of the ADC dynamic range of about 300 channels from 1024.

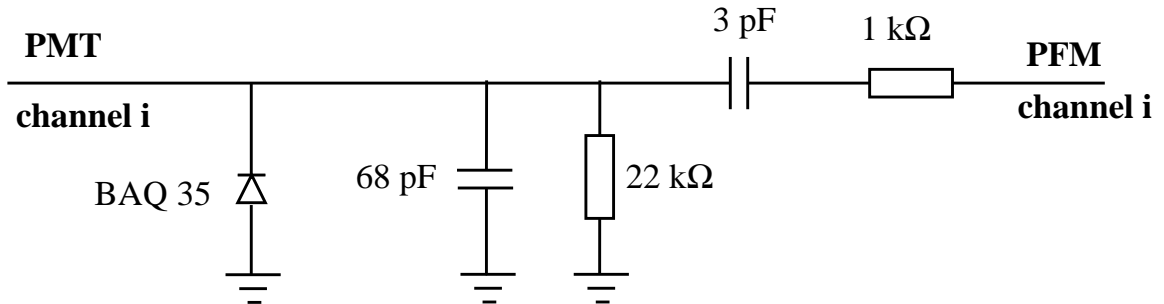


Figure 5.11: Capacitive Coupling Between PMTs and GASSIPLEX Input

As was mentioned at the beginning of the section, the expected charge for low momenta protons dramatically exceeds the dynamic range of the GASSIPLEX chip amplifier. For this reason, capacitive coupling with attenuative behavior was designed and implemented. The aim of the test was to merge the attenuation factor in such a way that signals corresponding to 70 P.E. will still be within the dynamic range of the PFM. The attenuation of the input signal can be achieved in part by lowering the PMT high voltage supply value. The second part of achieving the necessary attenuation factor was capacitive coupling between the PMTs and the PFM. For this purpose, a PCB support board was designed for the PMTs. The PMT is soldered to this board in the position that the capacitive circuit is assembled for each channel. A diagram of the capacitive coupling is shown in Fig. 5.11. The shown values of capacitors and resistors were chosen for the first test. In order to merge the integration constant of the GASSIPLEX chip amplifier, the combination of parallel resistors and capacitor has to have a time constant of $1-2 \mu\text{s}$. The serial capacitor has to be small and comparable to the internal capacitance of the GASSIPLEX chip due to noise consideration. The internal capacitance of the GASSIPLEX chip is in the order of a few pF. The ratio between serial and parallel capacitors determines the attenuation factor of the RC-coupling circuit.

The capacitive coupling connection to the PMT and PFM was then tested in the following way. A blue LED was installed in front of the light guide in the black-box. The LED was connected to the pulser, which provided short pulses with a length of 10 ns. The light guide was coupled to one pixel of the multi-anode PMT and the second pulser

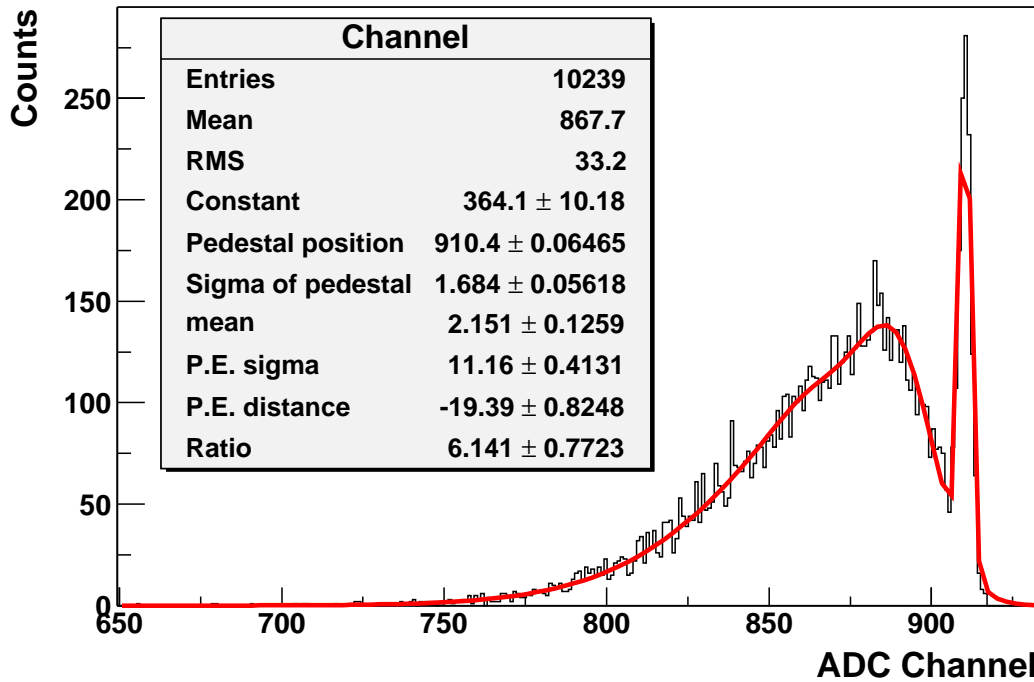


Figure 5.12: Example of the calibration spectrum of one PFM channel. The spectrum is fitted by Poisson distribution.

output was used as the trigger. The electronics were read out as described previously. The amplitude was chosen so that the yield of the PMT was just above its noise value. An example of the resulting spectrum is shown in Fig. 5.12. The spectrum has been taken with the following combination of the coupling circuit elements: The serial capacitor was 8.2 pF, the parallel capacitor was 680 pF, the PMT high voltage was 970 V and the trigger delay was 600 ns. The multiplexer was powered by -7.5 V and $+6.3$ V.

The spectrum was fitted by a function derived from the Poisson distribution. If the number of photoelectrons is small, the distribution has to follow the Poisson distribution

$$P(n) = \frac{\mu^n e^{-\mu}}{n!}, \quad (5.7)$$

where $P(n)$ is the probability of finding n photoelectrons and μ is the mean number of photoelectrons. The n -photoelectron peak can't appear as a line - due to PMT resolution it is smeared by the Gaussian and the width grows with the square root of the number of photoelectrons. The number of P.E. was small and the expansion of the Poisson distribution

has been taken up to the 8th term. The final function has the form

$$P(x) = C_1 \frac{1}{\sigma_{ped}} \exp\left(\frac{x-x_{ped}}{\sigma_{ped}^2}\right) \exp(-\mu) + C_2 \sum_{n=1}^8 \frac{1}{\sqrt{n}\sigma_{P.E.}} \exp\left(\frac{x-x_{ped}-n\mu x_{P.E.}}{n\sigma_{P.E.}^2}\right) \frac{\mu^n e^{-\mu}}{n!}, \quad (5.8)$$

where x corresponds to the ADC channel, x_{ped} is the position of pedestal, σ_{ped} is the pedestal width, μ is the mean number of P.E., $x_{P.E.}$ is the distance of one P.E. peak from the pedestal mean and $\sigma_{P.E.}$ is the width of one P.E. peak. The width of the P.E. peak can be interpreted as the resolution of the PMT. The constants C_1 and C_2 are normalization factors which merge the fit function to the measured data.

5.4 GSI Test Beam

The result with the pulser and LED light source showed, that modification of the PFMs to accept PMT signals would be possible. In order to follow this line of reasoning, the electronics were tested with real signals from scintillating fibres. The Recoil Detector was designed to measure pion and proton momentum and to provide their identification according to the energy deposited in the detector. Three runs were organized with the mixed beam of protons and pions at the GSI facility in Darmstadt. The focus was on momenta up to 900 MeV - the range for which PID by the SFT is intended.

The GSI SIS 18 Tm synchrotron accelerator is a device which is able to provide a $p\pi^+$ mixed beam with the momentum range of interest [114]. The primary proton or heavy ion beam impacts on a B_4C production target. Magnetic field manipulation selects secondary fragments according to their momenta with a resolution of 10 %. Momenta of 300, 450, 600 and 900 MeV were chosen for the test. The secondary beam is composed mainly of pions and protons to which the contribution of heavier products is negligible. The test beam area is equipped with MWPCs, which provide information about the positions of particle tracks and can be used for rejecting multi-track events. Data taken in Nov. 2003 provides the main focus for study of the detector response. In parallel to the tests of the SFT, the other detector components of the Recoil project - the silicon detector (SD) and the photon detector (PD) were also tested.

5.4.1 Experimental Setup

The tests were designed to obtain information about the performance of the SFT modules - their gain and efficiency of detection of pions and protons. Fig. 5.13 shows the

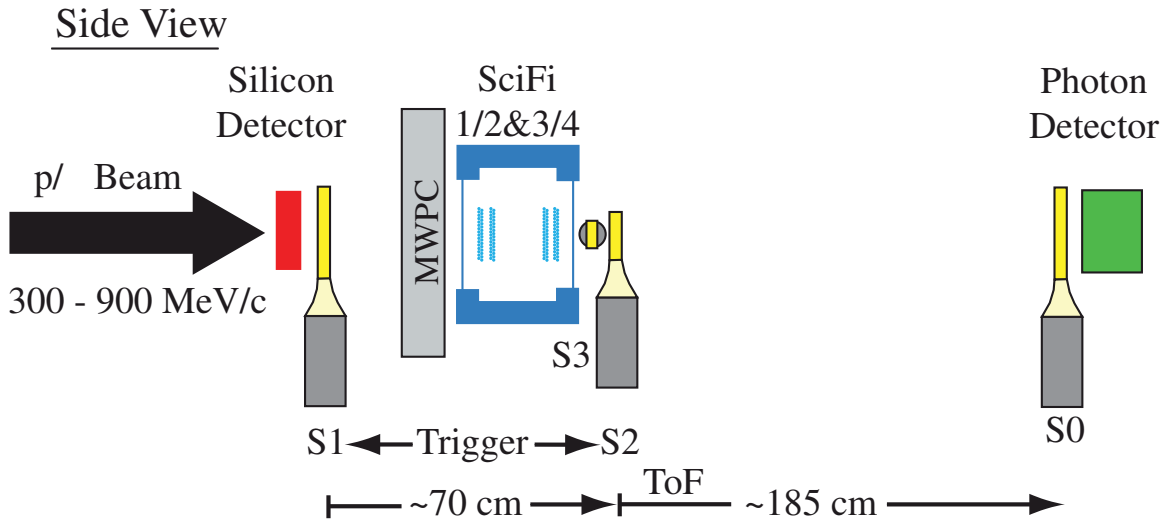


Figure 5.13: The side view of the experimental setup at the GSI in November 2003.

setup at GSI: four trigger scintillators (S0, S1, S2 and S3), MWPCs and modules of the SD, the SFT and the PD. The configuration scheme is derived from the design of the Recoil Detector. The Silicon Detector module was situated furthest upstream followed by the first trigger scintillator S1. The MWPCs behind the S1 scintillator were used to reject multi-track events and to provide position information on the track. All module types of the SFT were used. Modules 1 and 2 are inner-cylinder and 3 and 4 are outer-cylinder types. Modules with a parallel orientation of fibres alternate with modules with 10° tilted (stereo) orientations. Behind the SFT modules, a small scintillator S3 was placed, for efficiency measurements. Behind them was the scintillator S2 which provides, in coincidence with the scintillator S1, the trigger signal. Scintillator S0 is situated 185 cm downstream of S2 and was used for particle identification by the Time of Flight (TOF) method. The last detector of the setup is the PD.

Each SFT module was connected via clear light guides to a multi-anode PMT. More detailed descriptions about the mechanical parts will be published in [115]. The

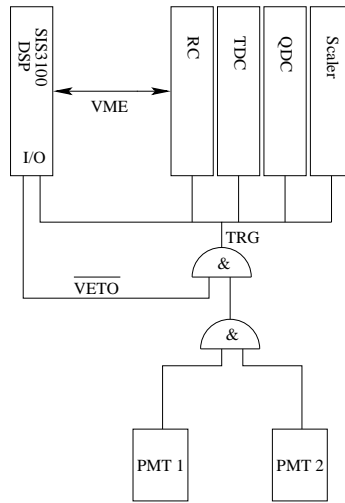


Figure 5.14: Diagram of the test beam trigger. Two PMTs produce the trigger in coincidence. The VETO signal has to be released during event processing.

PMTs were soldered onto the multilayer boards which provided the HV supply to the PMTs and also the coupling circuits between PMTs and PFMs.

5.4.2 Digitization and DAQ

The hardware part of the readout of the multi-anode photomultipliers remains mostly the same as is described in section 5.3. The only differences were values of four capacitors in the analog coupling circuit. The change was made in order to find the optimal values for the coupling circuit capacitor and high voltage for use in the final installation of the SFT. The capacitors used in the parallel branch of the coupling circuit had values of 100, 220, 330 and 470 pF, whereas in the serial branch all capacitors were 3 pF.

It was necessary to collect time and amplitude information from trigger scintillators in order to synchronize the data streams from the different VME modules. The time and energy information from the trigger scintillators provided an independent PID, which was used to test the PID capability of the SFT. In order to synchronize the data stream, trigger handling has been integrated with the readout program, which was running on a DSP processor. A diagram of the trigger distribution is shown in Fig. 5.14.

The signal from trigger scintillators S1, S2 and S0 was split by means of a Fan-in Fan-out module. The signal of S1 and S2 in coincidence was used as a common trigger for all

DAQ modules after passing through a discriminator. The modules receiving a trigger signal were the RC, the Charge to Digital Convertor (QDC V792), the start signal for a Time to Digital Convertor (TDC V775N), a scaler (Struck SIS3803) and the VME controller. The VME controller received the trigger signal through its first I/O port and used it as an interrupt of the running DSP program. The interrupted DSP program released the VETO signal on the second I/O port and started to poll the status register of the RC. During VETO release, generation of the next trigger signal was blocked.

For the QDC, the trigger signal was distributed as a 100 ns gate. The TDC was used in common-start mode, where the trigger signal was used as the start. For the FE, the trigger signal was delayed by about 600 ns due to the integration time of the GASSIPLEX chip amplifier. Finally, the scaler counted both the accepted and the unaccepted triggers on two of its sixteen input channels. Other channels were used for counting rates from single trigger scintillators and single wires of the MWPCs.

There were three modules of the QDC in the readout chain. Two modules were used for readout of one 64-channel PMT of the photon detector. The third one was used for digitization of amplitudes from single trigger scintillators.

Digitization of all the channels and storage the data above threshold in the FIFO memory on the PFM board take $10 \mu\text{s}$. In order to obtain information about the pedestal values of channels which were not hit, the threshold was set to zero. This prolonged the time needed for the collection of one event and extended the need for disk space. However, it provided useful information about the stability of the electronics during data taking. Since the signals are stored in the PFM's FIFO memory, the status register of the RC is switched to ready. The status register was polled by the VME controller, which started the transfer of data to SDRAM. After the RCs, the QDC and the TDC were read out. The scaler was read out only after every thousand events. These particular events were labeled in the header as "scaler events".

When all the VME modules were read out and the data was collected in 64 MB SDRAM on the VME controller board, the VETO signal was set to zero and the electronics were ready for the next event. Running in parallel to the program in the DSP on the VME-controller board a program on the PC organized data transfer from the VME-controllers SDRAM to the PC over a 1Gbit/s optolink. The dual ported memory (DPM) on the VME-controller was used for hand shaking bits necessary to control the access of both programs to the SDRAM. Uncontrolled parallel access of both programs to the SDRAM could have

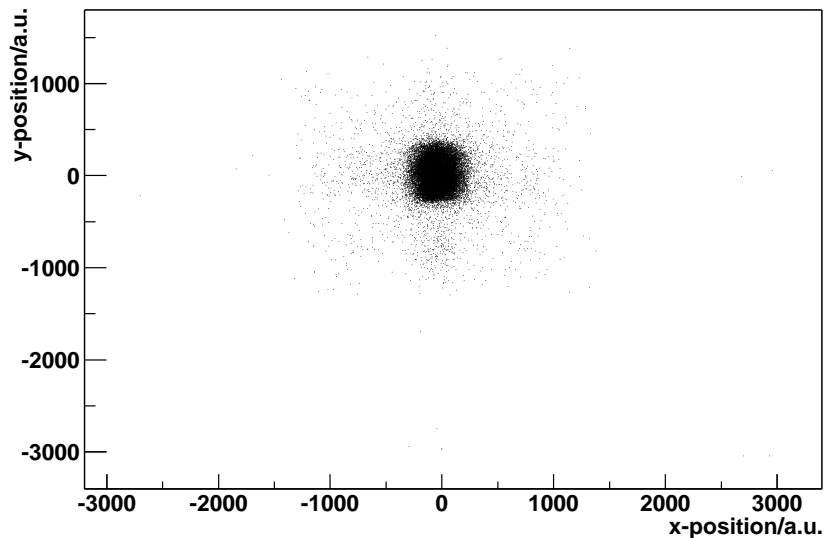


Figure 5.15: The scatter plot of the hit position obtained by the MWPC. The plot contains only single hit events.

led to a critical error and a full restart of DAQ would then have been necessary.

5.4.3 Results of the Testbeam

In this section a short review of the test beam result will be given. A detailed description of the test experiments is reported in [116] & [117]. Data containing single tracks was selected for the analysis. This was accomplished using timing information obtained by the MWPCs. The plot of the hit distribution over the $x - y$ plane after applying cuts is shown in Fig. 5.15

In order to obtain independent PID information, the time-of-flight between trigger scintillators was measured. Together with the energy deposited in the trigger scintillators, it allows very good separation of pions from protons. In Fig. 5.16, the two-dimensional distribution of both quantities is shown. Because the TOF strongly depends on the particle momenta as well as energy lost in the detector, the plots for the lowest momentum (300 MeV/c) and the highest (900 MeV/c) are compared. The dashed lines represent the cuts used for proton/pion separation.

The GSI experiment was designed to test the more complex performance of the

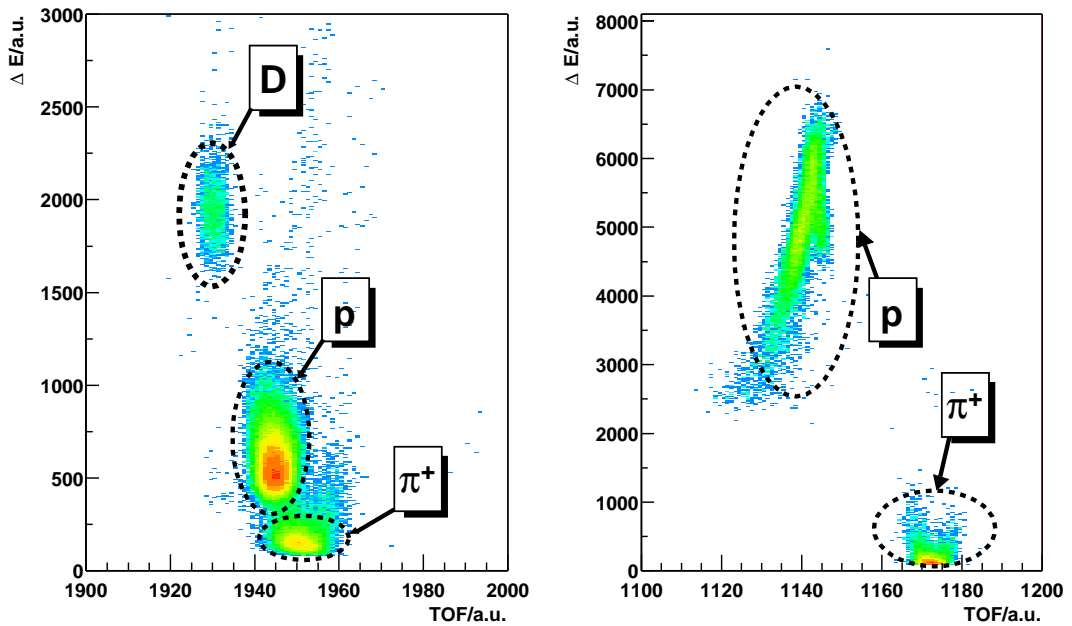


Figure 5.16: The energy deposition versus TOF. The right panel shows the distribution for particles with momentum 300 MeV/c. Good separation of pions (region in right bottom corner) and protons is obtained. The left plot shows the distribution for momentum 900 MeV/c. The proton and pion peak are closer but still good separable. The region in left upper corner represents hits caused by heavier particles like D or He_3 .

SFT under real beam conditions. A response-comparison between the commercially available electronics and customized electronics based on the GASSIPLEX chip was performed. Two similar modules situated behind each other in the mixed beam were connected to the 64 channel multi-anode photomultiplier. These were read-out, each by different electronics. The first module was read-out by two 32 channel CAEN QDC V792 VME boards while the second was connected via a customized PFM board with the GASSIPLEX chip. The results of both readout methods are compared in Fig 5.17. Events above a certain threshold are summed over all channels of the modules and separation between protons and pions has been done by means of TOF information. The spectra are, qualitatively, almost the same. Only in the QDC spectrum is a single photoelectron peak visible due to the finer resolution of the ADC (4096 channel) compared to the PFM ADC (1024 channel).

Each single fibre was calibrated in the same way as described in section 5.3.1. The

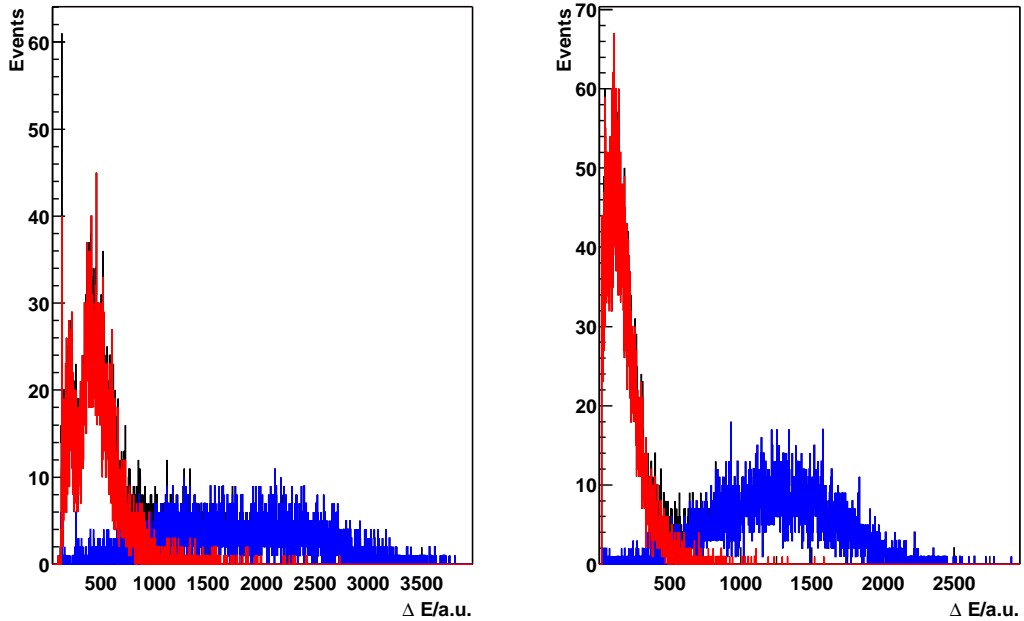


Figure 5.17: Comparison of the QDC and customized readout by measurement of energy deposition in each module caused by protons (blue) and pions (red) of 300 MeV/c. The left panel shows the response of CAEN QDC while the right shows the response of the customized PFM.

position of the single photoelectron peak was checked with the peak position of the signal from GSI data. The signal spectrum before and after applying calibration is shown in Fig. 5.18. Appropriate action has been taken to compensate for anode cross talk and losses of efficiency at the boundary of the lightguide and the anode. A dedicated algorithm [116] has been developed to reconstruct the hit channel. By means of this “cluster-algorithm”, the light output corresponding to a hit in a single fibre is summed. Combining information from PID detectors, the energy deposition in a single fibre from a hit caused by a proton or a pion can be reconstructed. In Fig. 5.19 the energy deposition in a single fibre is expressed in terms of the number of photoelectrons. From the displayed plots it is clearly seen that different energy deposition is caused by pions and protons. As expected, the difference is more significant for lower momenta particles. In the plot, the deposition in a single fibre is shown. In the final PID algorithm, the combination of information from all four layers is foreseen and data from the photon detector is included. A test of PID capability using the

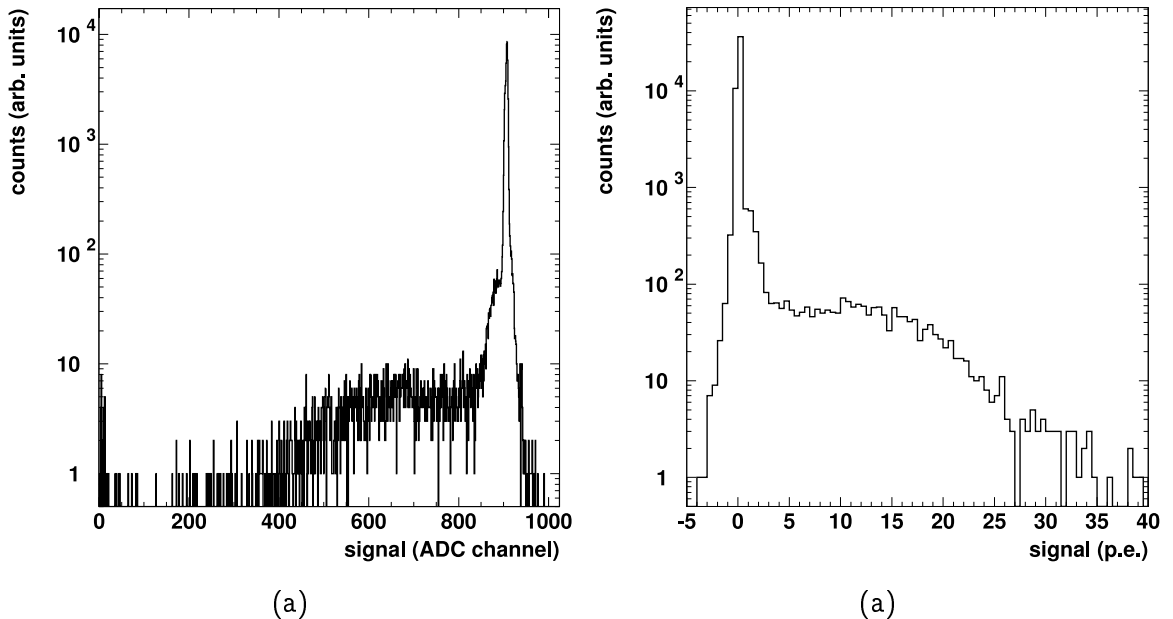


Figure 5.18: (a) Uncalibrated spectrum of a single SFT channel. On the lower ADC boundary the effect of erroneous overflow handling can be seen. (b) Spectrum of same SFT channel employing SPE calibration and including overflow suppression.

data of the first two runs has been performed in the diploma thesis of W. Sommer [113]. The result of this preliminary study shows proton identification efficiency from single modules to be about 85 %, with 10 % contamination by pions. This result fulfills the requirements for the SFT proposed in the Technical Design Report [104].

By means of a more sophisticated cluster algorithm in [116] and data from S3 trigger scintillator, it has been found that the detection efficiency of a single particle in one module is higher than reported in [113]. Depending on the readout channel threshold and the particle momentum, detection efficiency for the pions varies between 93 % and 99 %. For the protons, it is higher than 98 % over all thresholds or momenta. This results predict good performance from the Recoil Detector in terms of detection and identification of the recoiling proton from the DVCS process. The final algorithm which combines information from all of the subdetectors is under development by other members of recoil project.

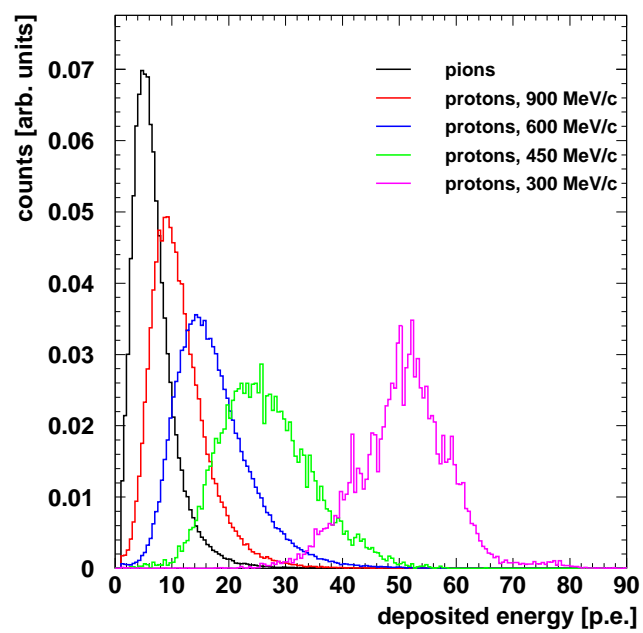


Figure 5.19: Energy deposition for protons or pions in a single fibre at different momenta.

Chapter 6

Conclusion

The observation of a narrow strange resonance with a mass of about 1540 MeV in the last few years has been one of the most exciting items of progress in the field of hadronic physics. The observed resonance properties agree with predictions published by Diakonov, Petrov and Polyakov which were based on chiral soliton model, where three members of the antidecuplet should exhibit exotic quantum numbers. Several experiments found this resonance either in the pK_S or in the nK^+ decay channel. These successful observers include the HERMES collaboration which reported a narrow resonance in the pK_S decay channel with a mass of about 1528 MeV and a width of 19 MeV. However, several experiments also reported non-observance of such a resonance, bringing into question the existence of such a resonance, thought originally to be the Θ^+ pentaquark.

The work described in this thesis was an analysis of the pK_S channel, as measured with the HERMES spectrometer. The kinematics of the detected pK_S system were investigated in detail. The most significant deduction made was that the Karliner-Lipkin scheme could be a possible tool for the reduction of background and investigate the production mechanism. There is a slight indication of forward peaking in the angular momentum distribution but the statistics used to investigate the method were too low to draw concrete conclusions.

In addition, to the analyses of the pK_S channel, an investigation of possible, artificial sources of the resonance was performed. A Monte Carlo simulation of N resonances decaying into a $K_S\Lambda$ has been used in order to determine if this is a possible source of a kinematic reflection, resulting in a narrow peak in the pK_S mass spectrum. All the N resonances between 1600 and 2000 MeV have been ruled out as a possible cause. Their broad

widths do not allow a narrow peak to form. The $\Xi^*(1690)$ can also be discounted since, although it can form a narrow peak, it exhibits too low a mass value to be a contender. Further evidence comes from studying the detector acceptance and the cross-section branching ratios which point to a number of events which is beyond the number seen in the observed peak.

Despite these tests to discount artificial sources for the observed peak, the HERMES result has a very low statistical significance, and so it is impossible to make a firm statement about the possible existence of the resonance, other than to note that there is no obvious source for the peak, should it be anything other than a statistical fluctuation.

The Recoil Project, designed to extend the HERMES capability to measure DVCS reactions, will also help to clarify the situation regarding the observed peak at 1528 MeV. Placed in the target region of the spectrometer, it will greatly enhance the acceptance of the spectrometer and provide enhanced particle identification, the latter being very important for the suppression of background.

Part of the work completed towards the attainment of a PhD was to design a readout system for the SFT part of the Recoil detector. The frontend electronics of the HADES detector were used as a basis for the readout of the multi-anode photomultipliers, necessitating some changes to the analog part of the existing system. The resultant design was tested both in the laboratory using an LED pulser and later in the GSI test facility. The test beam at GSI was also used to check the efficiency of the SFT in detecting minimally ionizing particles and that the SFT complies with the design requirements stated in the TDR concerning particles of higher momenta. The electronics were shown to be capable of separating one photoelectron peak and provide sufficient resolution to separate pions and protons with momenta between 450 MeV and 900 MeV.

These results for the SFT represent an internal goal in the Recoil Project, which should, in addition to investigating the DVCS reaction, help to establish the observance (or non-observance) of the Θ^+ at HERMES kinematics to a degree of satisfactory statistical significance.

List of Figures

2.1	The multiplets of the hadrons in the plane given by strangeness and z -components of the isospin. The left diagram shows the SU(3) octet of the mesons with and a Φ which belongs to the SU(3) singlet. The plot in middle shows the SU(3) baryon octet and the rightmost the baryon decuplet. . . .	8
2.2	Anti-decuplet of baryons. The corners of this diagram are manifestly exotic.	12
2.3	The first observation of the Θ^+ by the LEPs experiment [31]. Left panel a) shows the missing mass $MM_{\gamma K^+}^c$ spectrum for K^+K^- production for the signal sample (solid histogram) and for events which are accompanied with a proton hit. Right panel b) shows $MM_{\gamma K^-}^c$ for the signal sample (solid histogram) and for events accompanied with a proton hit (dotted histogram).	13
2.4	Compilation of the world data observed Θ^+ . Left panel shows the mass values and the right plot shows the FWHM.	15
3.1	Location of HERMES at the HERA storage ring. The other experiments H1, HERA-B and ZEUS, the Spin rotators and polarimeters are superimposed. The setup of run 2001-2007 is shown. Prior to 2001 there were no rotators at H1 and ZEUS.	21
3.2	Side view of the current setup of the HERMES spectrometer	23
3.3	Čerenkov angles versus momentum for aerogel and C_4F_{10} gas. The upper curve shows angles of the Čerenkov light cone coming from the aerogel radiator. The lower curve corresponds to the C_4F_{10} gas.	28
4.1	$\pi^+\pi^-$ invariant mass spectrum (left) and $\pi^+\pi^-p$ invariant mass spectrum (right). No cuts are applied on selected protons and pions. The $\pi^+\pi^-$ spectrum shows clear K_S peak while no structure is seen in the $\pi^+\pi^-p$ spectrum.	34
4.2	Topology of reconstructed three-track events	35
4.3	The $\pi^+\pi^-$ invariant mass spectrum left and the $\pi^+\pi^-p$ invariant mass spectrum right. The DCA and the decay length cuts are applied on selected pions in order to improve the K_S signal.	36

4.4	The $\pi^+\pi^-$ invariant mass spectrum left and the $\pi^+\pi^-p$ invariant mass spectrum right. The applied are extended by causality cut for position between $\pi^+\pi^-$ production and decay vertex. The $\pi^+\pi^-p$ spectrum is computed from events witch belong to the filled area of histogram in the left panel plot.	37
4.5	$\pi^+\pi^-$ invariant mass spectrum after applying the cuts is shown in the left panel. The spectrum is fitted with the sum of a polynomial of second order and a Gaussian. In the right panel, the π^-p invariant mass spectrum is shown.	38
4.6	The final invariant mass spectrum of the pK_S obtained by the HERMES experiment. The right plot shows the spectrum fitted by third order polynomial plus Gaussian. In the left picture are six Σ^* resonances fitted additionally to the background. The gray shaded histogram represents a normalized PΥTHIA6 simulation and the solid line histogram is the normalized result of a mixed event analysis.	39
4.7	The invariant mass distribution of the $\bar{p}K_S$ system. The statistics are too small for any statement about existence of Θ^- state,	42
4.8	The distribution of particle type of the fourth track.	43
4.9	Invariant mass spectrum of the system $K_S\pi$. The spectrum is generated from events where three tracks of standard Θ^+ cuts are accompanied by fourth track which is identified as pion.	44
4.10	The invariant mass spectrum of K_Sp system. Two opposite charged pions and protons are accompanied with the fourth track identified as pion. The events, where pion have together with K_S invariant mass of K^* or with p mass of the Λ , are excluded.	44
4.11	The invariant mass distribution of simulated Θ	47
4.12	The comparison of the simulated and measured angular distribution of the Θ^+ . In the simulation, the parent particle decays isotropically in the center-of-mass system. Angular distribution of simulated Θ^+ accepted by the HERMES spectrometer is displayed by the dashed line. The angular distribution corresponding to the events whose mass agree within 2σ to the mean of the observed peak are depicted by solid line.	48
4.13	The measured angular distributions of the pK_S system. The solid line is given by the events whose mass corresponds to the mass of the observed peak. The dashed line corresponds to background events out of the two σ -range around a peak.	48
4.14	The invariant mass spectrum of the pK^- system.	51
4.15	The invariant mass spectrum of the $\bar{p}K^+$ system.	52
4.16	The squared momentum difference $ P_K ^2 - P_N ^2$ plot. Solid line shows distribution of the signal events, whereas dotted line shows distribution of the background.	53

4.17	The scan of square momenta cut values for K.-L. scheme. The events below certain square momenta difference are selected and the final spectrum is fitted. In upper panels the dependence of naïve and realistic significance is showed. The dependence of peak position and width on the cut value is shown in lower panels.	54
4.18	The pK_S system mass spectrum after applying cut $ P_K ^2 - P_N ^2 < 5 \text{ GeV}^2/c^2$. 54	
4.19	The invariant mass spectrum of the events where system pK_S exhibits mass of $1528 \pm 30 \text{ MeV}$ and systems $p\pi^-$ have mass of the Λ $1116 \pm 18 \text{ MeV}$. The π^- is observed as the fourth track in the events.	56
4.20	The generated mass of the $N(1710)$ resonances.	58
4.21	The simulated momenta of the $N(1710)$ resonances. The upper left histogram shows the total momentum of the parent particle. The upper right shows the momentum distribution in the direction of the z -axis, lower left in the x -axis and lower right in the y -axis	58
4.22	The reconstructed mass spectrum of pK_S system. The generated events are coming from decay of $N(1710)$ decaying into $K_S\Lambda$. The π^- from the Λ decay is not reconstructed.	59
4.23	The fit of the reconstructed mass spectrum of the pK_S system. The fit function is composed as a sum of Breit-Wigner, Gauss and third order polynomial function	59
4.24	The fit of the pK_S mass spectrum. The fit function is the sum of a third degree polynomial, six Breit-Wigner function describing Σ^* resonances and a function obtained from $N(1710)$ kinematic reflection studies.	60
4.25	The pK_S system invariant mass spectrum obtained by higher statistic simulation of $N(1710)$	61
4.26	The pK_S system invariant mass spectrum obtained by simulation of $\Xi^{*0}(1690)$ decaying into $K_S^0\Lambda$. The peak has been fitted by means of Gaussian distribution.	62
5.1	The Feynman diagram of the DVCS and competitive Bethe-Heitler process	68
5.2	The missing mass spectrum of the DVCS process. The black points correspond to the measured data. The magenta area are MC DVCS events, the light blue area are events from fragmentation background	69
5.3	3D View of the Recoil Detector	70
5.4	The schematic view of fibre layout in the Scintillating Fibre Tracker. The fibres of the inner sub-layers are orientated parallel to the beam axis. Fibres wrapped around the barrel in a helix-shaped in the outer sub-layers form a stereo angel of 10° with respect to the beam direction. Two sub-layers are built into each of the parallel and stereo layers of either barrel.	72
5.5	Scheme of internal structure of GASSIPLEX	74
5.6	Block scheme of the PFM board	75
5.7	Timing of a complete sample cycle	76
5.8	Daisy chained connection of five PFMs	77
5.9	The result of the test of the PFMs response on the voltage of the input pulse.	79

5.10	Analog Multiplexer Scheme	80
5.11	Capacitive Coupling Between PMTs and GASSIPLEX Input	81
5.12	Example of the calibration spectrum of one PFM channel. The spectrum is fitted by Poisson distribution.	82
5.13	The side view of the experimental setup at the GSI in November 2003.	84
5.14	Diagram of the test beam trigger. Two PMTs produce the trigger in coincidence. The VETO signal has to be released during event processing.	85
5.15	The scatter plot of the hit position obtained by the MWPC. The plot contains only single hit events.	87
5.16	The energy deposition versus TOF. The right panel shows the distribution for particles with momentum 300 MeV/c. Good separation of pions (region in right bottom corner) and protons is obtained. The left plot shows the distribution for momentum 900 MeV/c. The proton and pion peak are closer but still good separable. The region in left upper corner represents hits caused by heavier particles like D or He_3	88
5.17	Comparison of the QDC and customized readout by measurement of energy deposition in each module caused by protons (blue) and pions (red) of 300 MeV/c. The left panel shows the response of CAEN QDC while the right shows the response of the customized PFM.	89
5.18	(a) Uncalibrated spectrum of a single SFT channel (b) Calibrated spectrum of same SFT channel	90
5.19	Energy deposition for protons or pions in a single fibre at different momenta.	91

List of Tables

2.1	Additive quantum numbers of the quarks.	8
2.2	Published experiments with evidence for Θ^+ resonance.	15
2.3	Published experiments with non observation of the Θ^+ resonance.	17
4.1	Mass and width values obtained by different fit procedures of the pK_s system and their systematic and statistical errors. Row Ia) is based on the fit using the simulated background model and Σ^* s. In the case of row Ib), background is fitted simply by a polynomial. Rows IIa) and IIb) are using same background models as Ia) and Ib) respectively, but different mass reconstruction expressions that are expected to result in better resolution. Number of signal and background events in 2σ area are in column marked as $N_s^{2\sigma}$ and $N_b^{2\sigma}$.	41

Bibliography

- [1] J. J. Thomson *Philosophical Magazine* 44, 293 (1897).
- [2] E. Rutherford, F.R.S.* *Philosophical Magazine Series 6*, vol. 21 May 1911, p. 669-688
- [3] M. Gell-Mann, *Phys. Rev.* **125** (1962) 1067.
- [4] M. Gell-Mann, *Phys. Lett.* **8** (1964) 214.
- [5] M. Gell-Mann and Y. Ne'eman 1964 *The Eightfold Way* (New York: Benjamin)
- [6] P. N. Kirk *et al.*, *Phys. Rev. D* **8** (1973) 63.
- [7] D. P. Barber *et al.*, *Phys. Rev. Lett.* **43** (1979) 830.
- [8] D. J. Gross and F. Wilczek, *Phys. Rev. Lett.* **30** (1973) 1343.
- [9] H. D. Politzer, *Phys. Rev. Lett.* **30** (1973) 1346.
- [10] K. Gottfried, *Phys. Rev. Lett.* **18** (1967) 1174.
- [11] M. Arneodo *et al.* [New Muon Collaboration], *Phys. Rev. D* **50** (1994) 1.
- [12] K. Ackerstaff *et al.* [HERMES Collaboration], *Phys. Rev. Lett.* **81** (1998) 5519 [arXiv:hep-ex/9807013].
- [13] F. M. Steffens and A. W. Thomas, *Phys. Rev. C* **55** (1997) 900 [arXiv:nucl-th/9612056].
- [14] G. Curci, W. Furmanski and R. Petronzio, *Nucl. Phys. B* **175** (1980) 27.
- [15] V. N. Gribov and L. N. Lipatov, *Sov. J. Nucl. Phys.* **15** (1972) 675 [*Yad. Fiz.* **15** (1972) 1218].
- [16] G. Altarelli and G. Parisi, *Nucl. Phys. B* **126** (1977) 298.

- [17] Y. L. Dokshitzer, Sov. Phys. JETP **46** (1977) 641 [Zh. Eksp. Teor. Fiz. **73** (1977) 1216].
- [18] A. Airapetian *et al.* [HERMES Collaboration], Phys. Lett. B **585** (2004) 213 [arXiv:hep-ex/0312044].
- [19] R. L. Jaffe, SLAC-PUB-1774 *Talk presented at the Topical Conf. on Baryon Resonances, Oxford, Eng., Jul 5-9, 1976*
- [20] R. L. Jaffe, Phys. Rev. D **15** (1977) 267.
- [21] R. L. Jaffe, Phys. Rev. D **15** (1977) 281.
- [22] V. Kopeliovich, Phys. Lett. B **259** (1991) 234.
- [23] M. Chemtob, Nucl. Phys. B **256** (1985) 600.
- [24] H. Walliser, Nucl. Phys. A **548** (1992) 649.
- [25] D. Diakonov, V. Petrov and M. V. Polyakov, Z. Phys. A **359** (1997) 305 [arXiv:hep-ph/9703373].
- [26] T. H. R. Skyrme, Nucl. Phys. **31** (1962) 556.
- [27] J. K. Perring and T. H. R. Skyrme, Nucl. Phys. **31**, 550 (1962).
- [28] K. Hicks, arXiv:hep-ex/0504027.
- [29] S. Kabana, arXiv:hep-ex/0503019.
- [30] S. Kabana, arXiv:hep-ex/0503020.
- [31] T. Nakano *et al.* [LEPS Collaboration], Phys. Rev. Lett. **91** (2003) 012002 [arXiv:hep-ex/0301020].
- [32] V. V. Barmin *et al.* [DIANA Collaboration], Phys. Atom. Nucl. **66** (2003) 1715 [Yad. Fiz. **66** (2003) 1763] [arXiv:hep-ex/0304040].
- [33] J. Barth *et al.* [SAPHIR Collaboration], Phys. Lett. B **572** (2003) 127.
- [34] A. E. Asratyan, A. G. Dolgolenko and M. A. Kubantsev, Phys. Atom. Nucl. **67** (2004) 682 [Yad. Fiz. **67** (2004) 704] [arXiv:hep-ex/0309042].

- [35] S. Chekanov *et al.* [ZEUS Collaboration], Phys. Lett. B **591** (2004) 7 [arXiv:hep-ex/0403051].
- [36] M. Abdel-Bary *et al.* [COSY-TOF Collaboration], Phys. Lett. B **595** (2004) 127 [arXiv:hep-ex/0403011].
- [37] A. Aleev *et al.* [SVD Collaboration], arXiv:hep-ex/0401024.
- [38] A. Aleev *et al.* [SVD Collaboration], arXiv:hep-ex/0509033.
- [39] B. Aubert *et al.* [BABAR Collaboration], arXiv:hep-ex/0408064.
- [40] K. Abe *et al.* [BELLE Collaboration], arXiv:hep-ex/0409010.
- [41] S. R. Armstrong, Nucl. Phys. Proc. Suppl. **142** (2005) 364 [arXiv:hep-ex/0410080].
- [42] J. Z. Bai *et al.* [BES Collaboration], Phys. Rev. D **70** (2004) 012004 [arXiv:hep-ex/0402012].
- [43] I. Abt *et al.* [HERA-B Collaboration], Phys. Rev. Lett. **93** (2004) 212003 [arXiv:hep-ex/0408048].
- [44] M. J. Longo *et al.* [HyperCP Collaboration], Phys. Rev. D **70** (2004) 111101 [arXiv:hep-ex/0410027].
- [45] D. O. Litvintsev [CDF Collaboration], Nucl. Phys. Proc. Suppl. **142** (2005) 374 [arXiv:hep-ex/0410024].
- [46] Y. M. Antipov *et al.* [SPHINX Collaboration], Eur. Phys. J. A **21** (2004) 455 [arXiv:hep-ex/0407026].
- [47] K. Abe *et al.* [Belle Collaboration], arXiv:hep-ex/0411005.
- [48] K. Goetzen [BaBar Collaboration], arXiv:hep-ex/0510041.
- [49] C. Pinkenburg [PHENIX Collaboration], J. Phys. G **30** (2004) S1201 [arXiv:nucl-ex/0404001].
- [50] M. Battaglieri, R. De Vita, V. Kubarovsky, L. Guo, G. S. Mutchler, P. Stoler and D. P. Weygand [the CLAS Collaboration], arXiv:hep-ex/0510061.

- [51] V. D. Burkert, arXiv:hep-ph/0510309.
- [52] M. I. Adamovich *et al.* [WA89 Collaboration], arXiv:hep-ex/0510013.
- [53] S. Stepanyan *et al.* [CLAS Collaboration], Phys. Rev. Lett. **91** (2003) 252001 [arXiv:hep-ex/0307018].
- [54] V. Kubarovsky *et al.* [CLAS Collaboration], Phys. Rev. Lett. **92** (2004) 032001 [Erratum-ibid. **92** (2004) 049902] [arXiv:hep-ex/0311046].
- [55] H. Z. Huang, arXiv:nucl-ex/0509037.
- [56] C. Alt *et al.* [NA49 Collaboration], Phys. Rev. Lett. **92** (2004) 042003 [arXiv:hep-ex/0310014].
- [57] B. Aubert *et al.* [BABAR Collaboration], Phys. Rev. Lett. **95** (2005) 042002 [arXiv:hep-ex/0502004].
- [58] K. Stenson [FOCUS Collaboration], Int. J. Mod. Phys. A **20** (2005) 3745 [arXiv:hep-ex/0412021].
- [59] J. Spengler [HERA-B Collaboration], Acta Phys. Polon. B **36** (2005) 2223 [arXiv:hep-ex/0504038].
- [60] A. Airapetian *et al.* [HERMES Collaboration], Phys. Rev. D **71** (2005) 032004 [arXiv:hep-ex/0412027].
- [61] M. I. Adamovich *et al.* [WA89 Collaboration], Phys. Rev. C **70** (2004) 022201 [arXiv:hep-ex/0405042].
- [62] S. Chekanov *et al.* [ZEUS Collaboration], Phys. Lett. B **610** (2005) 212 [arXiv:hep-ex/0501069].
- [63] C. Alt *et al.* [NA49 Collaboration], Phys. Rev. Lett. **92** (2004) 042003 [arXiv:hep-ex/0310014].
- [64] A. Aktas *et al.* [H1 Collaboration], Phys. Lett. B **588** (2004) 17 [arXiv:hep-ex/0403017].
- [65] R. L. Jaffe and F. Wilczek, Phys. Rev. Lett. **91** (2003) 232003 [arXiv:hep-ph/0307341].
- [66] A. Gal and E. Friedman, Phys. Rev. Lett. **94** (2005) 072301 [arXiv:nucl-th/0511033].

- [67] C. Alexandrou and A. Tsapalis, arXiv:hep-lat/0503013.
- [68] A. I. Titov, A. Hosaka, S. Date and Y. Ohashi, Phys. Rev. C **70** (2004) 042202 [arXiv:nucl-th/0408001].
- [69] K. Ackerstaff *et al.* [HERMES Collaboration], Nucl. Instrum. Meth. A **417** (1998) 230 [arXiv:hep-ex/9806008].
- [70] A. Nass *et al.*, Nucl. Instrum. Meth. A **505** (2003) 633.
- [71] J. T. Brack *et al.*, Nucl. Instrum. Meth. A **469** (2001) 47.
- [72] S. Bernreuther *et al.*, Nucl. Instrum. Meth. A **416** (1998) 45 [arXiv:hep-ex/9803005].
- [73] A. Andreev *et al.*, Nucl. Instrum. Meth. A **465** (2001) 482.
- [74] H. Avakian *et al.*, Nucl. Instrum. Meth. A **417** (1998) 69 [arXiv:hep-ex/9810004].
- [75] N. Akopov *et al.*, Nucl. Instrum. Meth. A **479** (2002) 511 [arXiv:physics/0104033].
- [76] T. Benisch *et al.*, Nucl. Instrum. Meth. A **471** (2001) 314.
- [77] K. Wittenburg, 11th ICFA Mini-Workshop on Diagnostics for High-Intensity Hadron Machines, ORNL Spallation Neutron Source project in Oak Ridge, Tennessee, U.S., October 21-23, 2002
- [78] U. Elschenbroich HERMES 02-013, June 2002
- [79] S. Eidelman *et al.* [Particle Data Group Collaboration], Phys. Lett. B **592** (2004) 1.
- [80] W. Verkerke and D. Kirkby, eConf **C0303241** (2003) MOLT007 [arXiv:physics/0306116].
- [81] T. Sjostrand, P. Eden, C. Friberg, L. Lonnblad, G. Miu, S. Mrenna and E. Norrbin, Comput. Phys. Commun. **135** (2001) 238 [arXiv:hep-ph/0010017].
- [82] E.-C. Aschenauer, P. Liebing, and T.Sjostrand, in preparation.
- [83] W. Yu, Y. Mao, X. Lu, H. Ye, B. Ma. HERMES 04-018, June 2004
- [84] A. Airapetian *et al.* HERMES Release report, September 16, 2003

- [85] GEANT Detector Description and Simulation Tool, CERN Program Library, Long Writeup, W5013, 1994.
- [86] A. Airapetian, W. Deconinck, F. Giordano HERMES 04-030, September 2003
- [87] C. F. von Weizsacker, *Z. Phys.* **88** (1934) 612.
- [88] E. J. Williams, *Phys. Rev.* **45** (1934) 729.
- [89] M. A. Moinester, D. Ashery, L. G. Landsberg and H. J. Lipkin, *Z. Phys. A* **356** (1996) 207 [arXiv:hep-ph/9510356].
- [90] M. Karliner and H. J. Lipkin, *Phys. Lett. B* **616** (2005) 191 [arXiv:hep-ph/0501189].
- [91] A. R. Dzierba, D. Krop, M. Swat, S. Teige and A. P. Szczepaniak, *Phys. Rev. D* **69** (2004) 051901 [arXiv:hep-ph/0311125].
- [92] A. R. Dzierba, D. Krop, M. Swat, S. Teige and A. P. Szczepaniak, *Phys. Rev. D* **71** (2005) 098502.
- [93] K. Hicks, V. Burkert, A. E. Kudryavtsev, I. I. Strakovsky and S. Stepanyan, *Phys. Rev. D* **71** (2005) 098501.
- [94] M. I. Adamovich *et al.* [WA89 Collaboration], *Eur. Phys. J. C* **5** (1998) 621 [arXiv:hep-ex/9710024].
- [95] S. F. Biagi *et al.*, *Z. Phys. C* **34** (1987) 15.
- [96] C. Dionisi *et al.* [Amsterdam-CERN-Nijmegen-Oxford Collaboration], *Phys. Lett. B* **80** (1978) 145.
- [97] S. F. Biagi *et al.*, *Z. Phys. C* **9** (1981) 305.
- [98] F. Giordano, DESY-HERMES-04-55
- [99] X. D. Ji, *J. Phys. G* **24** (1998) 1181 [arXiv:hep-ph/9807358].
- [100] A. V. Radyushkin, arXiv:hep-ph/0101225.
- [101] K. Goetze, M. V. Polyakov and M. Vanderhaeghen, *Prog. Part. Nucl. Phys.* **47** (2001) 401 [arXiv:hep-ph/0106012].

- [102] M. Diehl, Phys. Rept. **388** (2003) 41 [arXiv:hep-ph/0307382].
- [103] The HERMES Collaboration DESY PRC 01-01, HERMES 01-017, April 2001
- [104] The HERMES Collaboration DESY PRC 02-01, HERMES 02-003, April 2002
- [105] J. C. Santiard *et al.*, CERN-ECP-94-17 *Presented at the 6th Pisa Meeting on Advanced Detectors, La Biodola, Isola d'Elba, Italy, 22 - 28 May 1994*
- [106] J. C. Santiard and K. Marent [ALICE Collaboration], CERN-ALICE-PUB-2001-49
- [107] EL4421C/22C/41C/42C/43C/44C-data sheet Rev.C. Elantec Inc. January 1996
- [108] ADS820 data sheet, Burr-Brown Corp. October 1996
- [109] MG-7010 data sheet, Seiko-Epson Inc.
- [110] CY7C420/421 data sheet, Cypress Semiconductor, August 1993
- [111] Anton Kastnüller, Michael Böhmer, Jürgen Friese, et l. Fast detector readout for the HADES RICH. Nucl. Instr. Meth. A **433**(1999)438
- [112] M. Böhmer, Diploma Thesis, TU München 2000.
- [113] W. Sommer, Diploma Thesis, JLU Giessen 2003
- [114] J. Diaz *et al.*, Nucl. Instrum. Meth. A **478** (2002) 511.
- [115] M. Hoek, Thesis, JLU Giessen in preparation
- [116] M. Hoek *et al.* HERMES 05-013, April 2005
- [117] M. Hoek, *et al.* Nucl. Instrum. Meth. A in preparation

Acknowledgments

I would like to express my gratitude to my advisor Prof. Dr. Michael Düren who made it possible for me to work at HERMES and supervised me during the writing of my PhD.

I wish to thank also Bjoern Seitz for his time and help with the development of the SFT electronics and the analysis of the data pertaining to the Recoil project. I highly appreciate the help and assistance of Matthias Hartig during his stay in Giessen. I am especially grateful for his coordination of the test beam at GSI Darmstadt and the expertise that he provided at that facility.

Many thanks to my friend and office mate Matthias Hoek for his support and fruitful discussions on all subjects during the completion of this work. My thanks go to all my colleagues in our group at Giessen as well.

I would like to express my thanks to the developers of the HADES electronics for their continuous aid and assistance: Jörg Lehnert, Michal Böhmer and Roman Gernhäuser.

My thanks also go to members of HERMES collaboration. I would like to thank the management of the Recoil Project for the opportunity to participate in such an interesting program of detector development. I would also like to thank all the members of the “Exotics Analysis Group” for many productive discussions and continued motivation during the analysis period of my work.

I wish to express my gratitude to representatives of the Copenhagen-Gießen-Helsinki-Jyväskylä-Torino European Graduate School on “Complex Systems of Hadrons and Nuclei” for their financial support and the opportunities they provided for me to participate in exciting Lecture Weeks and colloquia.

In addition, I would like to thank to Morgan Murray for his help in correcting the grammar and spelling of this publication.

Last but not least, I would like to express my heartfelt thanks to my parents for providing me their continued support throughout my education.